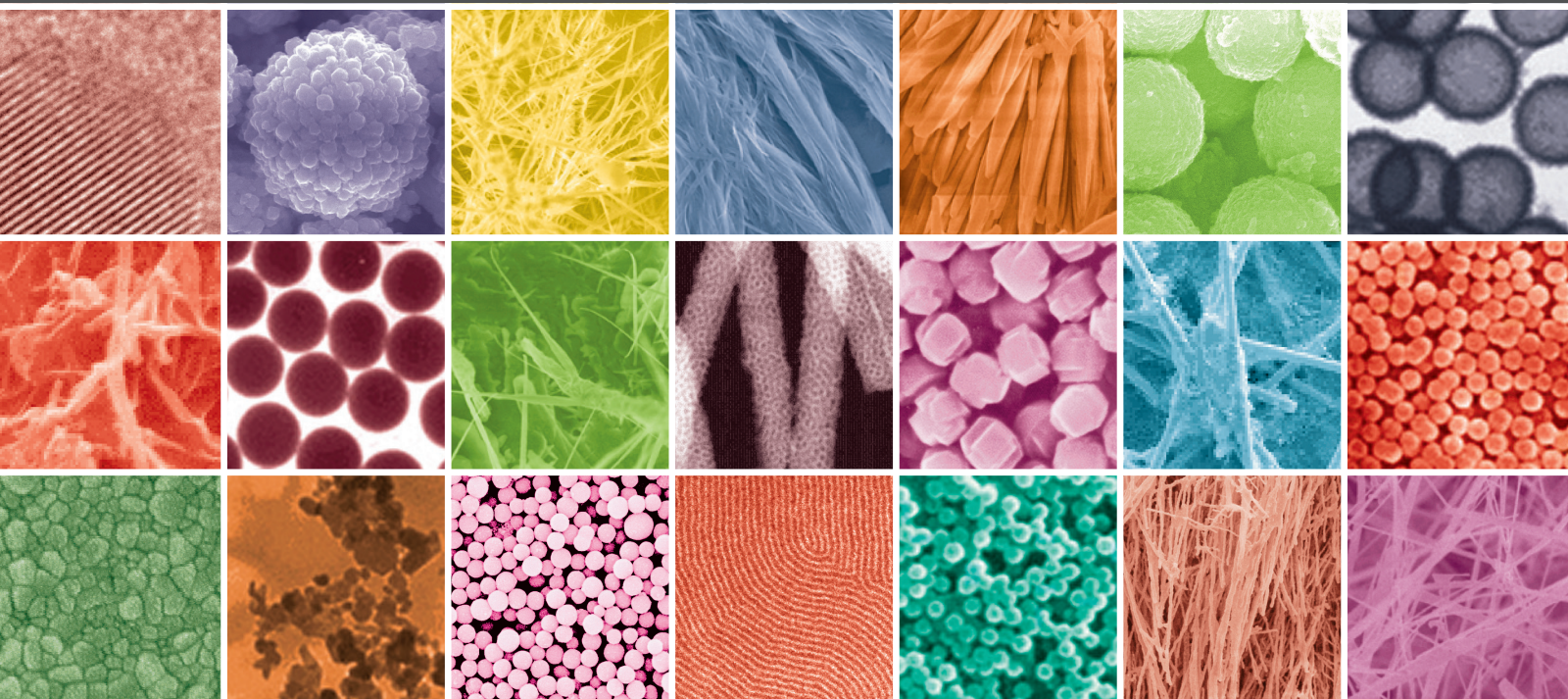


# Testing, Measurement, and Characterization of Nanomaterials

OPEN ACCESS

Guest Editors: Bei Peng, Changhong Ke, Yaling Liu, and Yong Zhu





---

# **Testing, Measurement, and Characterization of Nanomaterials**

Journal of Nanomaterials

---

## **Testing, Measurement, and Characterization of Nanomaterials**

Guest Editors: Bei Peng, Changhong Ke, Yaling Liu,  
and Yong Zhu



---

Copyright © 2015 Hindawi Publishing Corporation. All rights reserved.

This is a special issue published in "Journal of Nanomaterials." All articles are open access articles distributed under the Creative Commons Attribution License, which permits unrestricted use, distribution, and reproduction in any medium, provided the original work is properly cited.

## Editorial Board

Domenico Acierno, Italy  
Katerina Aifantis, USA  
Sheikh Akbar, USA  
Nageh K. Allam, USA  
Margarida Amaral, Portugal  
Raul Arenal, Spain  
Ilaria Armentano, Italy  
Vincenzo Baglio, Italy  
Lavinia Balan, France  
Thierry Baron, France  
Andrew R. Barron, USA  
Reza Bayati, USA  
Hongbin Bei, USA  
Daniel Bellet, France  
Stefano Bellucci, Italy  
Enrico Bergamaschi, Italy  
Samuel Bernard, France  
Debes Bhattacharyya, New Zealand  
Sergio Bietti, Italy  
Giovanni Bongiovanni, Italy  
Theodorian Borca-Tasciuc, USA  
Mohamed Bououdina, Bahrain  
Torsten Brezesinski, Germany  
C. Jeffrey Brinker, USA  
Christian Brosseau, France  
Philippe Caroff, Australia  
Victor M. Castaño, Mexico  
Albano Cavaleiro, Portugal  
Bhanu P. S. Chauhan, USA  
Shafiu Chowdhury, USA  
Jin-Ho Choy, Korea  
Kwang-Leong Choy, UK  
Yu-Lun Chueh, Taiwan  
Elisabetta Comini, Italy  
Giuseppe Compagnini, Italy  
David Cornu, France  
M. A. Correa-Duarte, Spain  
P. Davide Cozzoli, Italy  
Shadi A. Dayeh, USA  
Luca Deseri, USA  
Yong Ding, USA  
Philippe Dubois, Belgium  
Alain Dufresne, France  
Zehra Durmus, Turkey  
Joydeep Dutta, Oman

Ali Eftekhari, USA  
Jeffrey Elam, USA  
Samy El-Shall, USA  
Ovidiu Ersen, France  
C. Estournès, France  
Andrea Falqui, KSA  
Matteo Ferroni, Italy  
Elena Johan Foster, USA  
Ilaria Fratoddi, Italy  
Wolfgang Fritzsche, Germany  
Alan Fuchs, USA  
Miguel A. Garcia, Spain  
Siddhartha Ghosh, Singapore  
P. K. Giri, India  
Russell E. Gorga, USA  
Jihua Gou, USA  
Jean M. Greneche, France  
John Zhanhu Guo, USA  
Smrati Gupta, Germany  
Kimberly Hamad-Schifferli, USA  
Simo-Pekka Hannula, Finland  
Michael Harris, USA  
Yasuhiko Hayashi, Japan  
F. Hernandez-Ramirez, Spain  
Michael Z. Hu, USA  
Nay Ming Huang, Malaysia  
Shaoming Huang, China  
David Hui, USA  
Zafar Iqbal, USA  
B. Jeyadevan, Japan  
Xin Jiang, Germany  
Rakesh Joshi, Australia  
Jeong-won Kang, Korea  
Hassan Karimi-Maleh, Iran  
Antonios Kelarakis, UK  
Alireza Khataee, Iran  
Ali Khorsand Zak, Iran  
Philippe Knauth, France  
Ralph Krupke, Germany  
Christian Kübel, Germany  
Prashant Kumar, UK  
Michele Laus, Italy  
Eric Le Bourhis, France  
Burtrand Lee, USA  
Jun Li, Singapore

Meiyong Liao, Japan  
Shijun Liao, China  
Silvia Licoccia, Italy  
Wei Lin, USA  
Jun Liu, USA  
Zainovia Lockman, Malaysia  
Nico Lovergine, Italy  
Jim Low, Australia  
Jue Lu, USA  
Songwei Lu, USA  
Ed Ma, USA  
Laura M. Maestro, Spain  
Gaurav Mago, USA  
Muhamamd A. Malik, UK  
Devanesan Mangalaraj, India  
Sanjay R. Mathur, Germany  
Tony McNally, UK  
Yogendra Mishra, Germany  
Paulo Cesar Morais, Brazil  
Paul Munroe, Australia  
Jae-Min Myoung, Korea  
Rajesh R. Naik, USA  
Albert Nasibulin, Russia  
Toshiaki Natsuki, Japan  
Koichi Niihara, Japan  
Natalia Noginova, USA  
Sherine Obare, USA  
Won-Chun Oh, Republic of Korea  
Atsuto Okamoto, Japan  
Abdelwahab Omri, Canada  
Ungyu Paik, Republic of Korea  
Piersandro Pallavicini, Italy  
Edward A. Payzant, USA  
Alessandro Pegoretti, Italy  
Ton Peijs, UK  
Oscar Perales-Pérez, Puerto Rico  
Jorge Pérez-Juste, Spain  
Alexey P. Popov, Finland  
Philip D. Rack, USA  
Peter Reiss, France  
Orlando Rojas, USA  
Marco Rossi, Italy  
Ilker S. Bayer, Italy  
Cengiz S. Ozkan, USA  
Sudipta Seal, USA



---

Shu Seki, Japan  
Vladimir Šepelák, Germany  
Huaiyu Shao, Japan  
Prashant Sharma, USA  
Donglu Shi, USA  
Bhanu P. Singh, India  
Surinder Singh, USA  
Vladimir Sivakov, Germany  
Ashok Sood, USA  
Adolfo Speghini, Italy  
Marinella Striccoli, Italy  
Xuping Sun, KSA  
Ashok K. Sundramoorthy, USA

Angelo Taglietti, Italy  
Bo Tan, Canada  
Valeri P. Tolstoy, Russia  
Muhammet S. Toprak, Sweden  
Ramon Torrecillas, Spain  
Takuya Tsuzuki, Australia  
Tamer Uyar, Turkey  
Bala Vaidhyanathan, UK  
Luca Valentini, Italy  
Rajender S. Varma, USA  
Ester Vazquez, Spain  
Antonio Villaverde, Spain  
Ajayan Vinu, Australia

Ruibing Wang, Macau  
Shiren Wang, USA  
Yong Wang, USA  
Magnus Willander, Sweden  
Ping Xiao, UK  
Zhi Li Xiao, USA  
Yangchuan Xing, USA  
Doron Yadlovker, Israel  
Yoke K. Yap, USA  
Kui Yu, Canada  
William W. Yu, USA  
Michele Zappalorto, Italy  
Renyun Zhang, Sweden

# Contents

**Testing, Measurement, and Characterization of Nanomaterials**, Bei Peng, Changhong Ke, Yaling Liu, and Yong Zhu  
Volume 2015, Article ID 751698, 1 page

**Preparation of Homogeneous Nanostructures in 5 Minutes for Cancer Cells Capture**, Lixue Wang, Chuandong Zhu, Qin Zheng, and Xia He  
Volume 2015, Article ID 391850, 6 pages

**Mg Doping Effect on the Microstructural and Optical Properties of ZnO Nanocrystalline Films**, San-Lin Young, Ming-Cheng Kao, Hone-Zern Chen, Neng-Fu Shih, Chung-Yuan Kung, and Chun-Han Chen  
Volume 2015, Article ID 627650, 5 pages

**Obtaining Highly Crystalline Barium Sulphate Nanoparticles via Chemical Precipitation and Quenching in Absence of Polymer Stabilizers**, Ángela B. Sifontes, Edgar Cañizales, Jhoan Toro-Mendoza, Edward Ávila, Petra Hernández, Blas A. Delgado, G. Brenda Gutiérrez, Yraida Díaz, and Eliandreina Cruz-Barrios  
Volume 2015, Article ID 510376, 8 pages

**A Slope-Adapted Sample-Tilting Method for Profile Measurement of Microstructures with Steep Surfaces**, Hui Fang, Bin Xu, Wei Chen, Hairong Tang, and Shiping Zhao  
Volume 2015, Article ID 253062, 8 pages

**Frontal Cryosectioning: An Improved Protocol for Sectioning Large Areas of Fibrous Scaffolds**, Casey P. Grey and David G. Simpson  
Volume 2015, Article ID 359696, 7 pages

**Low-Temperature Sintering Bonding Using Silver Nanoparticle Paste for Electronics Packaging**, Wei Guo, Zhi Zeng, Xiaoying Zhang, Peng Peng, and Shanping Tang  
Volume 2015, Article ID 897142, 7 pages

**Butterfly-Inspired 2D Periodic Tapered-Staggered Subwavelength Gratings Designed Based on Finite Difference Time Domain Method**, Houxiao Wang, Wei Zhou, Er Ping Li, and Rakesh Ganpat Mote  
Volume 2015, Article ID 740984, 7 pages

**Changes in Nanoscaled Mechanical and Rheological Properties of Asphalt Binders Caused by Aging**, Ben Liu, Junan Shen, and Xuyan Song  
Volume 2015, Article ID 961924, 6 pages

**Size-Dependent Optical Properties of Nanoscale and Bulk Long Persistent Phosphor  $\text{SrAl}_2\text{O}_4:\text{Eu}^{2+}$ ,  $\text{Dy}^{3+}$** , Xiaoxia Duan, Lixin Yi, Xiqing Zhang, and Shihua Huang  
Volume 2015, Article ID 298692, 7 pages

**Impact of  $\text{NiO}_x$  Buffer Layers on the Dielectric Properties of  $\text{BaTiO}_3$  Thin Films on Nickel Substrates Fabricated by Polymer Assisted Deposition**, Hui Du, Yang Li, Wei Zheng Liang, Yu Xuan Wang, Min Gao, Wen Huang, Yin Zhang, and Yuan Lin  
Volume 2015, Article ID 167569, 7 pages

**Magnetization Reversal and Specific Loss Power of Magnetic Nanoparticles in Cellular Environment Evaluated by AC Hysteresis Measurement**, Satoshi Ota, Tsutomu Yamada, and Yasushi Takemura  
Volume 2015, Article ID 836761, 8 pages

## *Editorial*

# **Testing, Measurement, and Characterization of Nanomaterials**

**Bei Peng,<sup>1</sup> Changhong Ke,<sup>2</sup> Yaling Liu,<sup>3</sup> and Yong Zhu<sup>4</sup>**

<sup>1</sup>*School of Mechatronics Engineering, University of Electronic Science and Technology of China, Chengdu, Sichuan 611731, China*

<sup>2</sup>*Department of Mechanical Engineering, Binghamton University, State University of New York (SUNY), Binghamton, NY 13902-6000, USA*

<sup>3</sup>*Department of Mechanical Engineering and Mechanics, Lehigh University, PA 18015, USA*

<sup>4</sup>*Department of Mechanical and Aerospace Engineering, North Carolina State University, Raleigh, NC 27695-7910, USA*

Correspondence should be addressed to Bei Peng; [beipeng@uestc.edu.cn](mailto:beipeng@uestc.edu.cn)

Received 6 July 2015; Accepted 6 July 2015

Copyright © 2015 Bei Peng et al. This is an open access article distributed under the Creative Commons Attribution License, which permits unrestricted use, distribution, and reproduction in any medium, provided the original work is properly cited.

Materials and structures at the nanoscale often have unique mechanical, electronic, or optical properties. With emergence of various novel nanoscale materials and structures over the past decades, traditional testing and characterization techniques may not be suitable any more especially when structures are formed with sizes comparable to any of many possible length scales. In this special issue, original research articles were selected which cover the mechanical, electrical, thermal, optical, and biological properties of a broad range of nanomaterials. We hope the special issue will stimulate finding of new phenomena and properties and developing novel techniques for testing and characterization of nanomaterials.

*Bei Peng  
Changhong Ke  
Yaling Liu  
Yong Zhu*

## Research Article

# Preparation of Homogeneous Nanostructures in 5 Minutes for Cancer Cells Capture

Lixue Wang,<sup>1,2</sup> Chuandong Zhu,<sup>1</sup> Qin Zheng,<sup>1</sup> and Xia He<sup>3</sup>

<sup>1</sup>Department of Oncology, The Second Affiliated Hospital of Southeast University, Nanjing, Jiangsu 210003, China

<sup>2</sup>The Fourth Clinical Medical College of Nanjing Medical University, Nanjing, Jiangsu 210009, China

<sup>3</sup>Department of Radiation Oncology, The Affiliated Jiangsu Cancer Hospital of Nanjing Medical University, Nanjing, Jiangsu 210009, China

Correspondence should be addressed to Qin Zheng; txzzzq@sina.com and Xia He; zghexia@sina.com

Received 30 December 2014; Revised 28 March 2015; Accepted 31 March 2015

Academic Editor: Yaling Liu

Copyright © 2015 Lixue Wang et al. This is an open access article distributed under the Creative Commons Attribution License, which permits unrestricted use, distribution, and reproduction in any medium, provided the original work is properly cited.

Grafting aptamers on nanostructured substrates has shown ultrasensitivity in isolation of circulating tumor cells (CTCs). Here, we report that over 80 cm<sup>2</sup> of homogenous nanostructured surface on glass substrates can be prepared in 5 min after one-step dry etching. The surface area was doubled; the average diameter of nanostructures is approximately 374 nm, which is more close to the nanostructures of natural extracellular matrix. Antiepitheial cell adhesion molecule aptamers grafted nanostructured glass substrates captured over 76% of PC3 cells compared to 30% of planar substrates. Bispecific aptamers cofunctionalized nanostructured substrates, however, fail to capture cancer cells probably due to the formation of heterodimers. This limitation reveals that multispecific aptamers, when applied to cell isolation, must be analyzed to exclude any potential formation of heterodimers due to complementary sequence matching.

## 1. Introduction

Circulating tumor cells (CTCs) as emerging tumor biomarkers can provide valuable information for clinical diagnosis, prognosis, and treatment [1–5]. Over the last decade, numerous methods for detection and isolation of CTCs have been developed [6]. Recently, nanostructured substrates have emerged as very promising tools. They provide more surface area for ligands immobilization and lower the rolling velocity of cells in microchannels [7, 8]. Cancer cells also can dynamically arrange focal adhesion points [9]. However, there are two major challenges. First, due to the limitations of existing nanofabrication techniques, large-scale fabrication of homogeneous nanostructured substrates is nontrivial [10, 11]. These nanostructured substrates in small pieces (few cm<sup>2</sup>) only process a limited amount of blood at a time ( $\leq 1$  mL) [1]. Clinically relevant CTCs detection approaches should be able to process at least 7.5 mL of blood [12]. Thus, preparation of homogeneous nanostructures in large area is compulsory. Heterogeneity of CTCs poses the other challenge. Currently

biological isolation approaches heavily rely on antiepitheial cell adhesion molecule (EpCAM). However, CTCs may have little or no expression of EpCAM on the cell membrane [13], causing biased isolation of CTCs [14].

To prepare homogeneous nanostructures in larger area, we develop a new recipe using C<sub>3</sub>F<sub>8</sub> and C<sub>4</sub>F<sub>8</sub> as etchant gas and successfully obtain approximately 80 cm<sup>2</sup> projected area of homogeneous nanostructures after one-step dry etching in 5 min. Such area theoretically can process 8 mL whole blood samples for detection of CTCs [15]. On the other hand, to alleviate the challenge raised by heterogeneity of CTCs, we immobilize bispecific aptamers on nanostructured glass surface for cancer cells isolation. Aptamers are single-stranded oligomers that can specifically recognize and bind to target protein [16]. They are chemically stable at a wide range of pH, temperature, and ionic conditions [17]. Moreover, aptamers can be prepared in large quantity without batch-to-batch variation [18]. Bispecific aptamers have been used for targeted drug delivery [19]. However, it is unknown whether bispecific aptamers are able to increase isolation efficiency of

TABLE I: Sequences of respective aptamers and control DNA.

| Name        | Sequence (5' → 3')  |
|-------------|---|
| AEA [18]    | AAA AAA AAA AAA CAC TAC AGA GGT TGC GTC TGT CCC ACG TTG TCA TGG GGG GTT GGC CTG |
| APA [16]    | AAA AAA AAA AAA GCG TTT TCG CTT TTG CGT TTT GGG TCA TCT GCT TAC GAT AGC AAT GCT |
| Control DNA | AAA AAA AAA AAA CTG TCT TCG CGC CTA GCG CGA CCA TGT TAC AGA GCA GTG ATT TAG AGG |

cancer cells yet. To test the isolation efficiency, anti-EpCAM aptamers (AEA) or antiprostata specific membrane antigen (PSMA) aptamers (APA) are used.

Our results show that nanostructures with diameters ranging from 127 to 413 nm are successfully prepared, and nanostructured substrates can significantly increase cell capture efficacy. However, bispecific aptamers of AEA/APA mixture fail to capture PC3 cells due to the potential formation of heterodimers.

## 2. Materials and Methods

All chemicals were obtained from Sigma-Aldrich unless otherwise noted.

**2.1. Glass Slides Etching and Characterization.** The glass slides (Borofloat 33, Schott) were cleaned in piranha solution for 10 min at 90°C., followed by rinsing with DI water and drying in nitrogen flow. To create nanostructured surfaces, plain glass surface was subjected to RIE (ULVAC, NLD570 oxide etcher) for 3 to 15 min. The RIE condition was selected as C<sub>3</sub>F<sub>8</sub> (30 sccm), C<sub>4</sub>F<sub>8</sub> (10 sccm), Ar (50 sccm), O<sub>2</sub> (10 sccm), antenna power (2000 W), bias power (50–200 W), and chamber pressure (5 mTorr). After the RIE process, the glass surface was cleaned using piranha solution and DI water. Surface topography was evaluated quantitatively using a JPK atomic force microscope (AFM). Images of 10 × 10 μm area were captured in tapping model.

**2.2. Cell Culture.** PC3 cells (EpCAM<sup>+</sup>/PSMA<sup>-</sup>) were cultured in DMEM supplemented with 10% FBS, penicillin:streptomycin 100 U/mL and plated in T-25 tissue culture flasks (Corning, US). Flasks were placed into an incubator maintaining 5% CO<sub>2</sub> at 37°C and 10% humidity.

**2.3. Aptamers Binding to Cancer Cells.** The respective sequences of AEA and APA (Sangon, Shanghai) were shown in Table I. To confirm the binding of aptamer to cancer cells, Cy3 fluorescent groups labelled AEA, APA, and control DNA were incubated with PC3 cells. The aptamers were denatured by heating samples to 70°C for 5 minutes and then slowly cooling to RT. Cells in duplicate were seeded into 6-well cell culture plate and cultured for 48 hours. The aptamers and control DNA were incubated with cells at 37°C for 30 minutes under 5% CO<sub>2</sub>. After incubation, the cells were washed with 1x PBS three times, fixed with 4% paraformaldehyde for 30 min, and then stored in 1x PBS for optical and fluorescence imaging. The fluorescence images were taken followed by analysis of fluorescence intensity with *ImageJ*.

**2.4. Immobilize Aptamers onto Nanostructured Glass Surface.** All glass samples were immersed in 5% 3-aminopropyltriethoxysilane (APTES) in ethanol for 2 h at RT. The silanized substrates were then sequentially rinsed with DI water and cured at 120°C for 1 h. The substrates were then immersed in a dimethylformamide (DMF) solution containing 10% pyridine and 1 mM phenyldiisothiocyanate (PDITC) for 2 hours. Each substrate was then washed sequentially with DMF and 1,2-dichloroethane and dried under a stream of nitrogen. The amine group modified aptamers were prepared at 30 μM in DI water (ratio of AEA/APA: 1:3, 1:1, and 3:1). A volume of 25 μL of aptamer solution was placed on each substrate and allowed to incubate in a humidity chamber at 37°C overnight. Each substrate was then sequentially washed with methanol and DI water. The functionalized surface was then deactivated by capping unreacted PDITC moieties by immersion in 50 mM 6-amino-1-hexanol in DMF for 5 hours. Each substrate was then sequentially rinsed with DMF, methanol, and DI water.

**2.5. Cell Capture Assay and Image Analysis.** Four devices functionalized with AEA, APA, AEA/APA, and control DNA, respectively, were prepared for each type of cell. 1 × 10<sup>5</sup> cells/mL 500 μL of cell suspension was seeded onto 1 × 1 cm device surface and incubated at 37°C for 30 min, and then 1x PBS was used to wash off the nonspecifically bound cells. Captured cells were fixed with 4% paraformaldehyde for 1 h at RT and then treated with permeabilizing block buffer (1x PBS with 0.5% sodium azide supplemented with 0.05% Triton X-100 and 10% BSA). Cells were then washed with perm wash 1x PBS supplemented with 0.5% sodium azide followed by 0.1 μg/mL DAPI staining. The whole glass slide was analyzed using Cytell (GE, US) high-content imaging system using 10x objectives. The number of captured cells was counted through DAPI stained nuclei of cells. Cell capture efficiency was then defined as the ratio of the number of captured cells to the total number of cells.

**2.6. Electrophoresis Analysis of Heterodimers.** 8 μL of AEA and 8 μL of APA at 50 pM in 1x PBS were well mixed and denatured at 95°C for 5 min and then slowly cooled to RT. 8 μL of AEA or APA at 50 pM in 1x PBS was treated by the same procedure. Samples were analyzed by 4% agarose gel electrophoresis at 80 V at 4°C.

## 3. Results and Discussion

**3.1. Characterization of Nanostructures.** AFM images of samples and quantified results are shown in Figure 1 and Table 2.

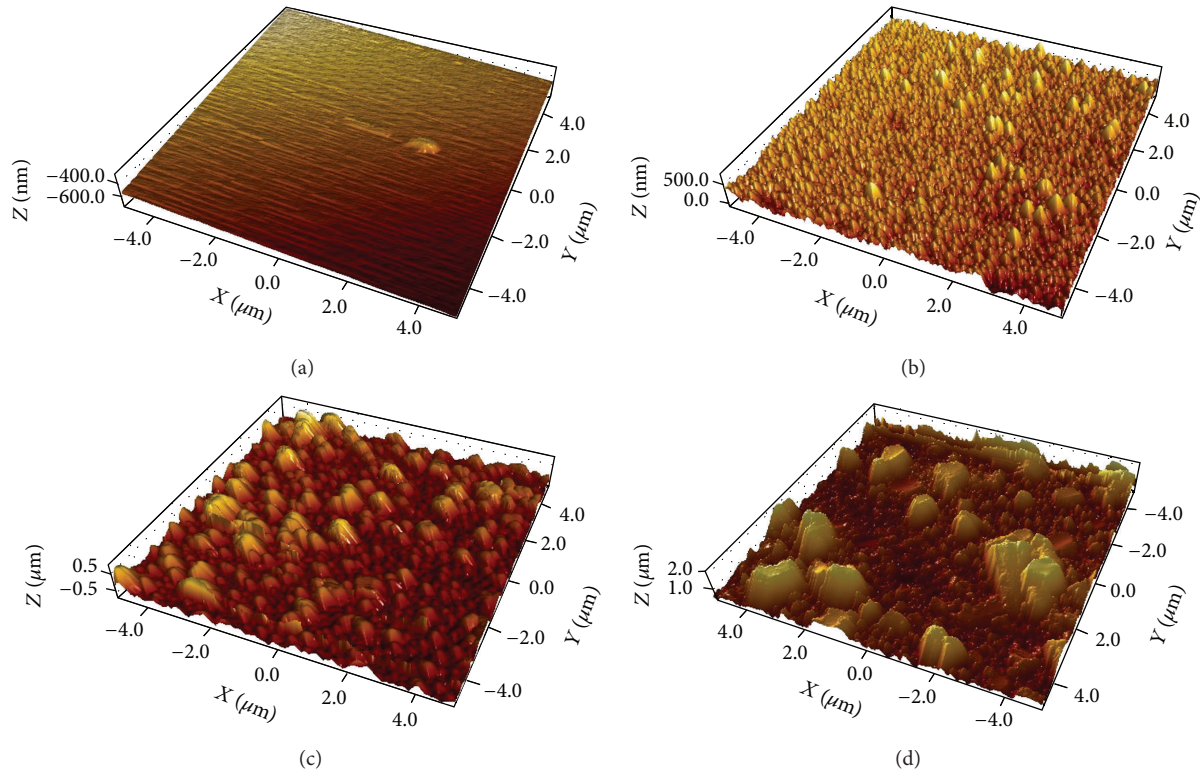


FIGURE 1: AFM images ( $10 \times 10 \mu\text{m}^2$ ) of the surface roughness of etched glass. (a) shows glass surface before etching; (b) shows glass etched at 50 W for 5 min; (c) shows glass etched at 100 W for 5 min; (d) shows glass etched at 200 W for 5 min.

TABLE 2: Characterization of glass substrates under different etching conditions.

| Etching condition | Surface area ( $\mu\text{m}^2$ ) | Mean diameter (nm) | $R_q$ (nm) |
|-------------------|----------------------------------|--------------------|------------|
| Unetched          | 102                              | 2                  | 6.5        |
| 50 W 5 min        | 191                              | 126.8              | 77.9       |
| 100 W 5 min       | 212                              | 374.3              | 203        |
| 200 W 5 min       | 363.5                            | 412.9              | 382.4      |

The increase of bias power can significantly increase the surface roughness. High bias power (200 W) is not ideal for preparation of homogeneous nanostructures and thus is excluded. Insular and abrupt microstructures are found probably due to fast etching rate (Figure 1(d)). We choose 100 W bias power and treatment for 5 min in following experiments. Previous research validated that cancer cell capture yield increased with nanoroughness [9]. Roughness of 203 nm obtained at 100 W is better. Moreover, the mean diameter of nanostructures obtained at 100 W for 5 min is 374.3 nm (Figure 1(c)). The size is more close to the nanostructures of natural extracellular matrix which fall in the range of 260 to 410 nm [1].

**3.2. Aptamers Binding to Cancer Cells.** To confirm AEA and APA can specifically recognize and bind to PC3 cells, Cy3

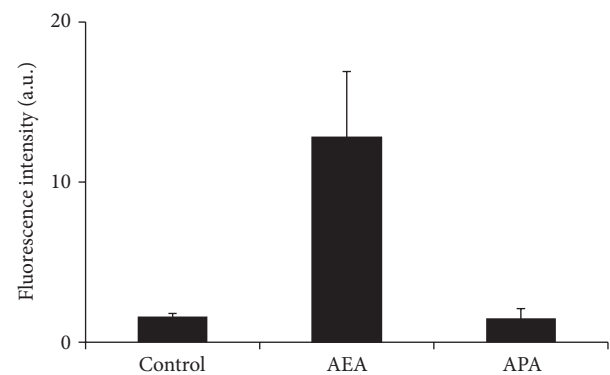


FIGURE 2: Average fluorescence intensity of AEA or APA binding to the LNCaP cells. Aptamers were allowed to interact and bind to cells at  $37^\circ\text{C}$  for 30 min in 5%  $\text{CO}_2$ . After binding, the cells were washed with 1x PBS three times.

labelled AEA, APA, and control DNA were directly incubated with cells. The fluorescence intensity of respective aptamers is shown in Figure 2. The fluorescence signals reveal that AEA can bind to PC3 cells that weakly express EpCAM. Previous study has confirmed that APA can specifically recognize and internalize into  $\text{PSMA}^+$  cells with minimal uptake into  $\text{PSMA}^-$  PC3 cells [20]. We did not detect fluorescent signals from dye labelled APA because of null expression of PSMA on PC3 cell membrane. Nonspecific adsorption or binding of control DNA probes did not occur.

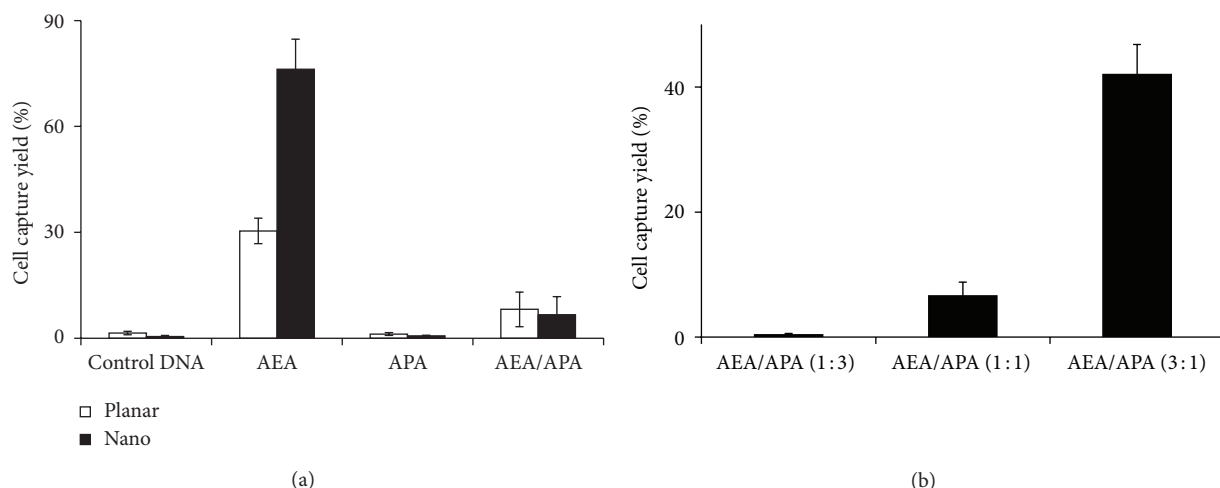


FIGURE 3: (a) shows average capture efficiency of PC3 cells on the AEA, APA, or AEA/APA functionalized planar and nanostructured surfaces; (b) shows differentiated capture efficiency of PC3 cells on the mixture of AEA and APA in ratio, respectively.  $1 \times 10^5$  cells were seeded onto surfaces and incubated at  $37^\circ\text{C}$  for 30 min in 5%  $\text{CO}_2$ . After binding, the cells were washed with 1x PBS three times.

**3.3. Cancer Cells Capture.** We firstly compared the difference of capture yield of PC3 cells between planar and nanostructured substrates (Figure 3(a)). 30.4% (SD: 3.6%) and 76.2% (SD: 8.5%) of PC3 cells were captured on planar and nanostructured glass substrates with AEA, respectively. The low capture efficiency of AEA functionalized planar surface might be raised by the inherent low-affinity interactions of aptamers [21]. The dissociation constant ( $K_d$ ) value of anti-EpCAM aptamer is approximately 20 nM, and it is fluctuant depending on the types of target cells [22]. Moreover, low amount of EpCAM (51,667 EpCAM molecules per cell) may be unable to gain sufficient binding forces during washing procedure [23]. In contrast, AEA grafted nanostructured substrates increase capture yield through higher odds of binding and higher total binding forces between AEA and EpCAM. In control groups, 1.4% (SD: 0.3%) and 0.5% (SD: 0.2%) of cells were captured on control DNA grafted planar and nanostructured substrates, respectively. Because PC3 cells do not express PSMA on cell membrane, approximately 1.2% (SD: 0.4%) and 0.7% (SD: 0.2%) of cells were nonspecifically captured onto APA functionalized planar and nanostructured substrates, respectively. Together, AEA grafted nanostructured substrates show better cell capture yield compared to that of planar substrates.

Once we incubated PC3 cells on AEA/APA cofunctionalized planar and nanostructured substrates, cell capture yield decreased significantly. Only 8.2% (SD: 4.9%) and 6.7% (SD: 5.1%) PC3 cells were captured on planar and nanostructured substrates, respectively. It might be caused by heterodimer between AEA and APA. Further, we used mixed AEA/APA in different ratios (1:3, 1:1, and 3:1) to reveal the potential formation of heterodimers. PC3 cells capture yields were 0.5%, 6.7%, and 42.1%, respectively. If AEA and APA did not form any heterodimers, AEA/APA (3:1) theoretically could capture approximately 60% of PC3 cells. However, in practical experiments, only 42% of cells were captured by AEA/APA in 3:1 ratio. The results indicated that a number of AEA were

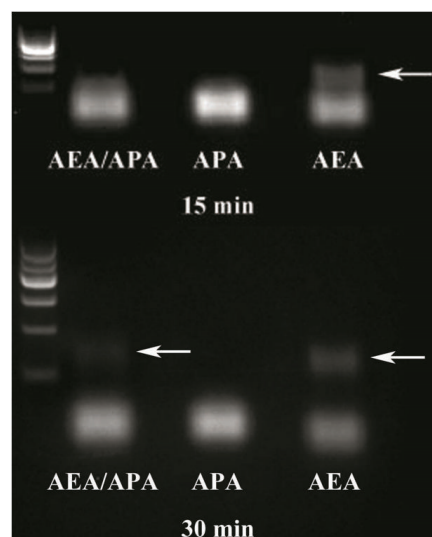


FIGURE 4: The potential heterodimer structure between AEA and APA. Electrophoresis of AEA, APA, and annealed AEA/APA at 15 and 30 min timepoints, respectively; samples were analyzed by 4% agarose gel electrophoresis at 80 V at  $4^\circ\text{C}$ .

unable to form suitable tertiary structures and to participate into antigens reorganization and capture. Alternatively, AEA does form right hairpin structures, but the recognition parts may be blocked by APA. However, in our design, both AEA and APA have 12 nt polyA spacer that can effectively prevent steric effect. Thus, the later speculation is invalid. The heterodimer analysis of AEA/APA and hairpin analysis of AEA or APA (IDT OligoAnalyzer 3.1) show the lowest Delta G value is  $-8.09$ ,  $-4.08$ , and  $-4.87$  kcal/mole, respectively. The values indicate all reactions are exergonic and spontaneous, and the heterodimer reaction between AEA and APA is more favourable. Figure 4 shows electrophoresis results of  $16 \mu\text{L}$  of AEA/APA,  $8 \mu\text{L}$  of APA, and  $8 \mu\text{L}$  of AEA, respectively, at 15

and 30 min timepoint, respectively. If heterodimers do not exist, the mixture should show the exact same bands with that of AEA. Although an approximately 120-nt band appeared in both AEA and the mixture of AEA and APA, it is much weaker in the mixture. We speculate that, in the mixture, AEA and APA may form heterodimers after annealing. The continuous electrophoretic forces in 30 min gradually destroy these heterodimers [20, 21], and once AEA and APA are compulsorily separated the mixture begins to show the similar distribution of bands. We admit that we do not have direct evidences to confirm the heterodimers; nevertheless the electrophoresis results demonstrate that AEA and APA have mutual interactions that can impede their dissociation.

#### 4. Conclusion

Homogeneous nanostructures in approximately 370 nm diameter can reliably and quickly be prepared on borosilicate glass slides using our recipe, and the aptamer functionalized nanostructured substrates can significantly improve cancer cell capture yield. However, bispecific aptamers cografted surface failed to capture cancer cells probably due to the formation of heterodimers. The potential shortcoming may impair the application of multispecific aptamers for detection and isolation of molecules unless the heterodimers between selected aptamers can be strictly excluded.

#### Conflict of Interests

The authors declare no competing financial interests.

#### Authors' Contribution

Lixue Wang and Chuandong Zhu contributed equally to this paper.

#### Acknowledgments

This project was supported by the Research Foundation of Jiangsu Provincial Commission of Health and Family Planning, China (Grant no. H201440); Medical Science and Technology Development Foundation, Nanjing Department of Health (Grant no. YKK14152); Jiangsu Provincial Natural Science Fund (no. BK20141018); "333" Project of Jiangsu Province (no. BRA2013292), Six Major Talent Peak Project of Jiangsu Province (class B, no. WS-047); and the Natural Science Foundation of China (nos. 30670619, 81072017).

#### References

- [1] L. Wang, W. Asghar, U. Demirci, and Y. Wan, "Nanostructured substrates for isolation of circulating tumor cells," *Nano Today*, vol. 8, no. 4, pp. 374–387, 2013.
- [2] H. J. Yoon, M. Kozminsky, and S. Nagrath, "Emerging role of nanomaterials in circulating tumor cell isolation and analysis," *ACS Nano*, vol. 8, no. 3, pp. 1995–2017, 2014.
- [3] X. Liu and S. Wang, "Three-dimensional nano-biointerface as a new platform for guiding cell fate," *Chemical Society Reviews*, vol. 43, no. 8, pp. 2385–2401, 2014.
- [4] M. Lin, J.-F. Chen, Y.-T. Lu et al., "Nanostructure embedded microchips for detection, isolation, and characterization of circulating tumor cells," *Accounts of Chemical Research*, vol. 47, no. 10, pp. 2941–2950, 2014.
- [5] H. Ma, J. Liu, M. M. Ali et al., "Nucleic acid aptamers in cancer research, diagnosis and therapy," *Chemical Society Reviews*, vol. 44, no. 5, pp. 1240–1256, 2015.
- [6] M. Yu, S. Stott, M. Toner, S. Maheswaran, and D. A. Haber, "Circulating tumor cells: approaches to isolation and characterization," *The Journal of Cell Biology*, vol. 192, no. 3, pp. 373–382, 2011.
- [7] Y. Wan, M. A. I. Mahmood, N. Li et al., "Nanotextured substrates with immobilized aptamers for cancer cell isolation and cytology," *Cancer*, vol. 118, no. 4, pp. 1145–1154, 2012.
- [8] W. Han, B. A. Allio, D. G. Foster, and M. R. King, "Nanoparticle coatings for enhanced capture of flowing cells in microtubes," *ACS Nano*, vol. 4, no. 1, pp. 174–180, 2010.
- [9] W. Chen, S. Weng, F. Zhang et al., "Nanoroughened surfaces for efficient capture of circulating tumor cells without using capture antibodies," *ACS Nano*, vol. 7, no. 1, pp. 566–575, 2013.
- [10] S. Wang, Y. Wan, and Y. Liu, "Effects of nanopillar array diameter and spacing on cancer cell capture and cell behaviors," *Nanoscale*, vol. 6, no. 21, pp. 12482–12489, 2014.
- [11] M. A. I. Mahmood, Y. Wan, M. Islam et al., "Micro+nano-texturing of substrates to enhance ligand-assisted cancer cell isolation," *Nanotechnology*, vol. 25, no. 47, Article ID 475102, 2014.
- [12] J. C. Fischer, D. Niederacher, S. A. Topp et al., "Diagnostic leukapheresis enables reliable detection of circulating tumor cells of nonmetastatic cancer patients," *Proceedings of the National Academy of Sciences of the United States of America*, vol. 110, no. 41, pp. 16580–16585, 2013.
- [13] A. M. Sieuwerts, J. Kraan, J. Bolt et al., "Anti-epithelial cell adhesion molecule antibodies and the detection of circulating normal-like breast tumor cells," *Journal of the National Cancer Institute*, vol. 101, no. 1, pp. 61–66, 2009.
- [14] S.-M. Tu, "Heterogeneity of cancer," in *Origin of Cancers*, pp. 129–136, Springer, Berlin, Germany, 2010.
- [15] Y. Wan, M. Winter, B. Delalat et al., "Nanostructured polystyrene well plates allow unbiased high-throughput characterization of circulating tumor cells," *ACS Applied Materials & Interfaces*, vol. 6, no. 23, pp. 20828–20836, 2014.
- [16] S. M. Nimjee, C. P. Rusconi, and B. A. Sullenger, "Aptamers: an emerging class of therapeutics," *Annual Review of Medicine*, vol. 56, pp. 555–583, 2005.
- [17] Y. Wan, J. Tan, W. Asghar, Y.-T. Kim, Y. Liu, and S. M. Iqbal, "Velocity effect on aptamer-based circulating tumor cell isolation in microfluidic devices," *The Journal of Physical Chemistry B*, vol. 115, no. 47, pp. 13891–13896, 2011.
- [18] Y. Wan, D. Tamuly, P. B. Allen et al., "Proliferation and migration of tumor cells in tapered channels," *Biomedical Microdevices*, vol. 15, no. 4, pp. 635–643, 2013.
- [19] G. Zhu, L. Meng, M. Ye et al., "Self-assembled aptamer-based drug carriers for bispecific cytotoxicity to cancer cells," *Chemistry*, vol. 7, no. 7, pp. 1630–1636, 2012.
- [20] O. Boyacioglu, C. H. Stuart, G. Kulik, and W. H. Gmeiner, "Dimeric DNA aptamer complexes for high-capacity-targeted drug delivery using pH-sensitive covalent linkages," *Molecular Therapy—Nucleic Acids*, vol. 2, article e107, 2013.
- [21] Y. Wan, Y.-T. Kim, N. Li et al., "Surface-immobilized aptamers for cancer cell isolation and microscopic cytology," *Cancer Research*, vol. 70, no. 22, pp. 9371–9380, 2010.

- [22] Y. Song, Z. Zhu, Y. An et al., "Selection of DNA aptamers against epithelial cell adhesion molecule for cancer cell imaging and circulating tumor cell capture," *Analytical Chemistry*, vol. 85, no. 8, pp. 4141–4149, 2013.
- [23] S. L. Stott, C.-H. Hsu, D. I. Tsukrov et al., "Isolation of circulating tumor cells using a microvortex-generating herringbone-chip," *Proceedings of the National Academy of Sciences of the United States of America*, vol. 107, no. 43, pp. 18392–18397, 2010.

## Research Article

# Mg Doping Effect on the Microstructural and Optical Properties of ZnO Nanocrystalline Films

San-Lin Young,<sup>1</sup> Ming-Cheng Kao,<sup>1</sup> Hone-Zern Chen,<sup>1</sup> Neng-Fu Shih,<sup>1</sup>  
Chung-Yuan Kung,<sup>2</sup> and Chun-Han Chen<sup>2</sup>

<sup>1</sup>Department of Electronic Engineering, Hsiuping University of Science and Technology, Taichung 41280, Taiwan

<sup>2</sup>Department of Electrical Engineering, National Chung Hsing University, Taichung 40227, Taiwan

Correspondence should be addressed to San-Lin Young; [slyoung@hust.edu.tw](mailto:slyoung@hust.edu.tw) and Chung-Yuan Kung; [cylkung@nchu.edu.tw](mailto:cylkung@nchu.edu.tw)

Received 16 October 2014; Accepted 17 November 2014

Academic Editor: Changhong Ke

Copyright © 2015 San-Lin Young et al. This is an open access article distributed under the Creative Commons Attribution License, which permits unrestricted use, distribution, and reproduction in any medium, provided the original work is properly cited.

Transparent  $\text{Zn}_{1-x}\text{Mg}_x\text{O}$  ( $x = 0.01, 0.03, \text{ and } 0.05$ ) nanocrystalline films were prepared by sol-gel method followed by thermal annealing treatment of  $700^\circ\text{C}$ . Mg doping effect on the microstructural and optical properties of the  $\text{Zn}_{1-x}\text{Mg}_x\text{O}$  films is investigated. From SEM images of all films, mean sizes of uniform spherical grains increase progressively. Pure wurtzite structure is obtained from the results of XRD. Grain sizes increase from  $34.7\text{ nm}$  for  $x = 0.01$  and  $37.9\text{ nm}$  for  $x = 0.03$  to  $42.1\text{ nm}$  for  $x = 0.05$  deduced from the XRD patterns. The photoluminescence spectra of the films show a strong ultraviolet emission and a weak visible light emission peak. The enhancement of ultraviolet emission and reduction of visible emission are observed due to the increase of Mg doping concentration and the corresponding decrease of oxygen vacancy defects. Besides, the characteristics of the dark/photo currents with  $n\text{-Zn}_{1-x}\text{Mg}_x\text{O}/n\text{-Si}$  heterojunction are studied for photodetector application.

## 1. Introduction

The ZnO-based semiconductors have recently drawn much interest for the possible application in optoelectronics devices [1–3] due to the large direct band gap. These properties are important for application to commercial electronic products, such as photoconductors for electrophotography [4], varistors for electrical circuits [5], sensors for gas detection [6], and active layer for thin film transistors [7]. Highly conductive and optical transparent ZnO films in the visible range suitable for transparent electrodes in solar cell and liquid crystal display applications have been also reported [8, 9].

The ZnO-based thin films have been fabricated through various methods [10–12]. However, sol-gel spin coating method offers more merits due to ease-control of chemical composition and simpler method for large area coating at a low cost, compared with other high vacuum fabrication processes. For the application of ZnO-based semiconductors on electronic devices, one of the most promising methods is doping with elements from groups I and III and transitional

metals [13–15]. While the shift in PL and XRD versus Mg composition has been studied previously [16, 17], it becomes interesting to further explore the doping effect on the microstructural and optical properties of the ZnO-based films. In the present work, we survey the Mg-doping effect on the microstructural and optical properties of ZnO nanocrystalline films. In addition, the  $I$ - $V$  characteristics of photodetecting devices with  $n\text{-Zn}_{1-x}\text{Mg}_x\text{O}/n\text{-Si}$  heterojunction are studied.

## 2. Materials and Methods

$\text{Zn}_{1-x}\text{Mg}_x\text{O}$  ( $x = 0.01, 0.03, \text{ and } 0.05$ ) films were fabricated by sol-gel method. The source solutions were prepared by  $\text{Zn}(\text{C}_2\text{H}_3\text{O}_2)_2 \cdot 2\text{H}_2\text{O}$  (zinc acetate dehydrate),  $\text{Mg}(\text{CH}_3\text{COO})_2 \cdot 4\text{H}_2\text{O}$  (magnesium acetate),  $\text{C}_3\text{H}_8\text{O}_2$  (2-methoxyethanol), and  $\text{C}_2\text{H}_7\text{NO}$  (ethanolamine). Zinc acetate dehydrate and magnesium acetate were firstly dissolved in 2-methoxyethanol in stoichiometric proportions. The concentration of metal ions was kept at  $0.5\text{ M}$ . Then, ethanolamine

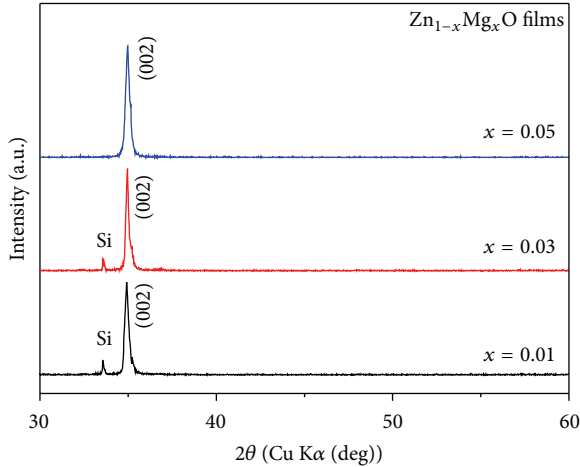


FIGURE 1: X-ray diffraction patterns of  $Zn_{1-x}Mg_xO$  films with  $x = 0.01$ ,  $x = 0.03$ , and  $x = 0.05$ .

was added into the solutions to form stable precursor solutions. After stirring at  $150^\circ\text{C}$  for 1 h on a hotplate, transparent solutions were obtained. The  $Zn_{1-x}Mg_xO$  thin films were prepared by spin coating technique. Then, the samples were annealed by rapid thermal annealing treatment in air at the temperature of  $700^\circ\text{C}$  for 2 min with a heating rate of  $600^\circ\text{C}/\text{min}$ .

The crystal structure and grain orientation of ZnO films were determined by the X-ray diffraction (XRD) patterns using a Rigaku D/max 2200 X-ray diffractometer with Cu-K $\alpha$  radiation. The XRD data were recorded at room temperature under the  $2\theta$  range from  $20^\circ$  to  $60^\circ$  with a step width of  $0.01^\circ$  and a scan speed of  $0.5^\circ/\text{min}$ . Morphological characterization was observed using a field emission scanning electron microscopy (FE-SEM, JEOL JSM-6700F) at 3.0 kV. The transmittance spectra were obtained by JASCO V-670 spectrophotometer. Room temperature photoluminescence (PL) spectroscopy was applied for optical emission measurement from 330 to 645 nm and defect analysis using the He-Cd laser with wavelength 325 nm. Finally, the DC current-voltage ( $I$ - $V$ ) characteristics of ( $Zn_{1-x}Mg_xO$  film)/( $n$ -Si substrate) structures were separately measured by an HP 4145 semiconductor parameter analyzer with the applied voltage from  $-5$  V to 5 V under darkness and photo illumination using a solar simulator with power density  $1000\text{ W}/\text{cm}^2$  as the irradiation source.

### 3. Results and Discussion

Figure 1 illustrates the XRD patterns of  $Zn_{1-x}Mg_xO$  nanocrystalline films. Based on the XRD patterns, all Mg-doped samples are found to have the same single polycrystalline phase with the wurtzite hexagonal structure of P63/mc. All samples exhibit the (002) preferred orientation, indicating  $c$ -axis orientation. The progressive narrowing of the XRD peaks with the increase of Mg concentration is related to the increase of the grain size of the nanocrystalline films. The

average grain size of the samples, obtained by the classical Scherrer formula, increases gradually from 34.7 nm for  $x = 0.01$  and 37.9 nm for  $x = 0.03$  to 42.1 nm for  $x = 0.05$ .

Figure 2 shows the surface morphology of FE-SEM images which reveals porously granular structure for all  $Zn_{1-x}Mg_xO$  films. It is clear that the grain size increases progressively with the increase of the Mg concentration, which is consistent with the results indicated in Figure 1. Furthermore, the film thickness decreases from 132 nm for  $x = 0.01$  and 124 nm for  $x = 0.03$  to 105 nm for  $x = 0.05$ . It is for the reason that the film is gradually densified due to the increase of Mg doping concentration.

Figure 3 shows the PL spectra for all  $Zn_{1-x}Mg_xO$  films. Two distinct emissions including an obvious ultraviolet (UV) emission and a weak green-yellow visible emission are observed. The UV emission originates from the exciton recombination corresponding through an exciton-exciton collision process [18]. The green-yellow emission is induced from the recombination of a photogenerated hole with an electron that belongs to a singly ionized defect, such as oxygen vacancy [19]. Gradual blue shift of the UV luminescence from 369.8 nm for  $x = 0.01$  and 366.2 nm for  $x = 0.03$  to 362.6 nm for  $x = 0.05$  occurs with the increase of Mg doping concentration. Using the luminescence data, the band gaps, 3.35 eV for  $x = 0.01$ , 3.38 eV nm for  $x = 0.03$ , and 3.41 eV nm for  $x = 0.05$ , are calculated. As the Mg concentration increased, the results indicate a linear increase in the band gap due to the higher band gap of MgO (7.8 eV) than that of ZnO (3.3 eV). The intensity of the ultraviolet emission is strongly dependent on the crystalline quality of ZnO films [20]. Besides, the decrease of visible emission with increasing Mg concentration indicates the decrease of intrinsic defects [21]. The enhancement of ultraviolet emission intensity ( $I_{UV}$ ) and reduction of green-yellow visible emission ( $I_{VIS}$ ) are observed due to the increase of Mg doping concentration and the corresponding decrease of oxygen vacancy defects. The ratio of the emission intensities of visible to UV emission (denoted as  $I_{VIS}/I_{UV}$ ) shows a decrease from 0.0876 and 0.0595 to 0.0488 of  $Zn_{1-x}Mg_xO$  films for  $x = 0.01$ ,  $x = 0.03$ , and  $x = 0.05$ , respectively. The decrease of  $I_{VIS}/I_{UV}$  ratio with increasing Mg concentration of  $Zn_{1-x}Mg_xO$  films shows a decrease of defects and an enhancement of crystallinity of the ZnO films, which is consistent with the result observed from XRD patterns.

Figure 4 shows the  $I$ - $V$  characteristics of  $Zn_{1-x}Mg_xO$  films deposited on  $n$ -type Si substrates for photodetector application, which was measured separately under dark (dark current,  $I_{\text{dark}}$ ) and photo illumination (photo current,  $I_{\text{photo}}$ ). The previous report elsewhere [22] stated that zinc oxides usually exhibit  $n$ -type semiconductor nature due to in situ defects. The PL results reveal the decrease of defects with Mg doping increase. We may continuously deduce the results of the decrease of carrier concentration, the increase of resistivity, and the decrease of both  $I_{\text{dark}}$  and  $I_{\text{photo}}$  currents. The measured ( $I_{\text{dark}}$ ,  $I_{\text{photo}}$ ) at 5 V are (4.12  $\mu\text{A}$ , 5.52  $\mu\text{A}$ ), (4.02  $\mu\text{A}$ , 5.12  $\mu\text{A}$ ), and (3.80  $\mu\text{A}$ , 4.84  $\mu\text{A}$ ) for  $x = 0.01$ ,  $x = 0.03$ , and  $x = 0.05$ , respectively. The variation of UV photo-induced current defined as  $(I_{\text{photo}} - I_{\text{dark}})/I_{\text{dark}}$  decreases from

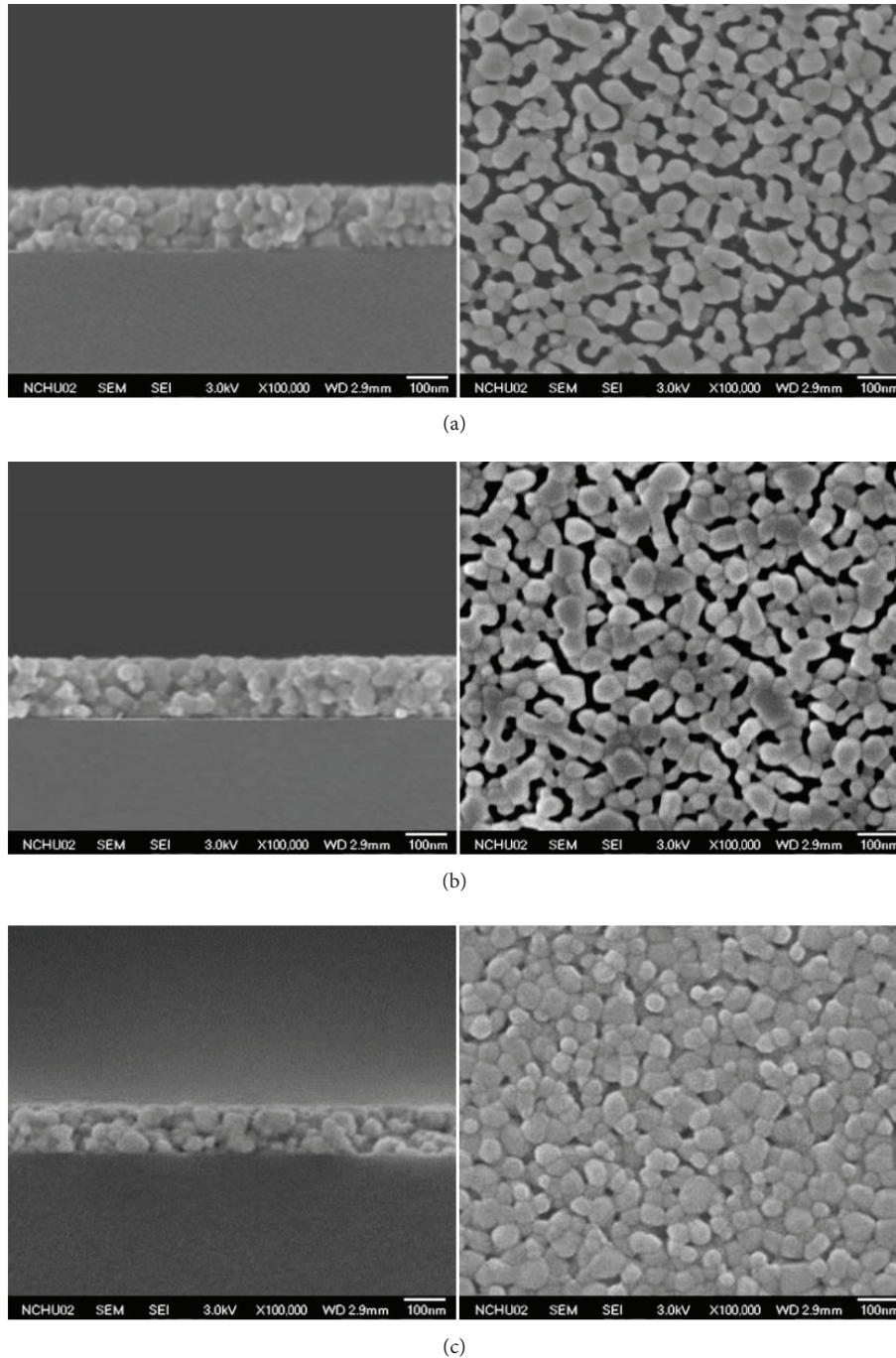


FIGURE 2: SEM images for  $Zn_{1-x}Mg_xO$  films of (a)  $x = 0.01$ , (b)  $x = 0.03$ , and (c)  $x = 0.05$ . Left and right columns show the cross-section and top view, respectively. The scale bars denote 100 nm.

34% and 28% to 27%. The results reveal the possibility of ZnO-based semiconductors for photodetector application.

#### 4. Conclusions

The Mg-doped ZnO nanocrystalline films were separately deposited by sol-gel spin coating method for comparison of microstructural and optical properties. XRD patterns

show that all compositions are found to exhibit the same wurtzite hexagonal structure with group space  $P63/mc$ . FE-SEM images show the grain size increases and the thickness decreases of  $Zn_{1-x}Mg_xO$  films with the increase of Mg doping concentration. The results of photoluminescence spectra show a linear increase of band gap and a decrease of defects.  $I$ - $V$  curves with the dark and photo illumination of the  $Zn_{1-x}Mg_xO$  film/ $n$ -Si structures reveal the possibility of ZnO-based semiconductors for photodetector application.

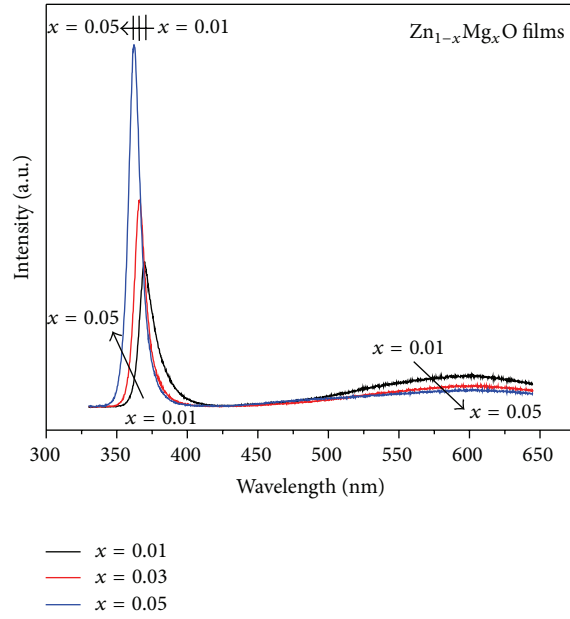


FIGURE 3: Photoluminescence spectra of  $\text{Zn}_{1-x}\text{Mg}_x\text{O}$  films with  $x = 0.01$ ,  $x = 0.03$ , and  $x = 0.05$ .

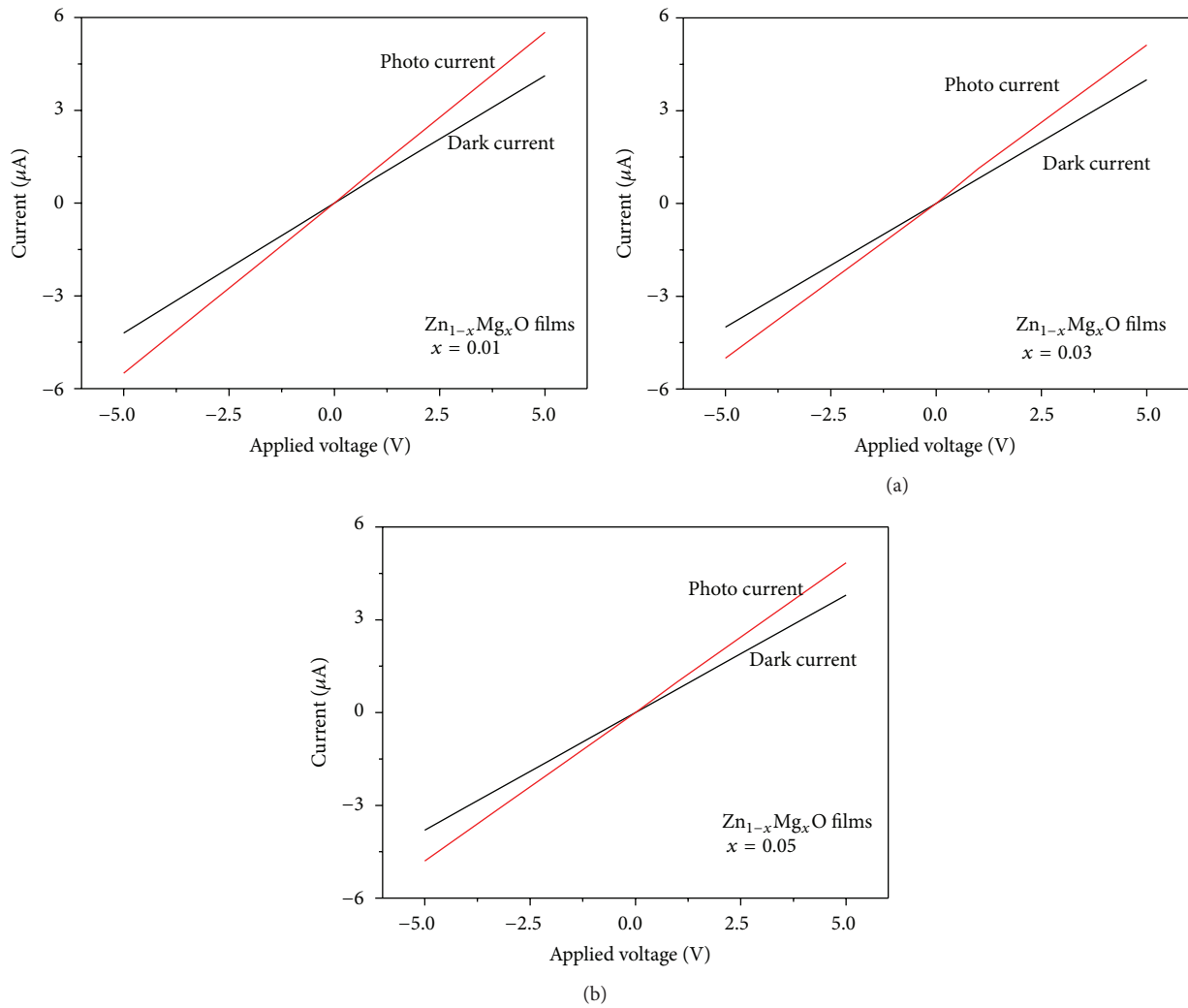


FIGURE 4: Dark/photo  $I$ - $V$  curves of  $\text{Zn}_{1-x}\text{Mg}_x\text{O}$  films with (a)  $x = 0.01$ , (b)  $x = 0.03$ , and (c)  $x = 0.05$ .

## Conflict of Interests

The authors declare that there is no conflict of interests regarding the publication of this paper.

## Acknowledgment

This work was sponsored by the Ministry of Science and Technology of the Republic of China under Grants nos. MOST 103-2221-E-164-003 and MOST 103-2221-E-005-033.

## References

- [1] P. I. Reyes, C.-J. Ku, Z. Duan, Y. Lu, A. Solanki, and K.-B. Lee, "ZnO thin film transistor immunosensor with high sensitivity and selectivity," *Applied Physics Letters*, vol. 98, no. 17, Article ID 173702, 2011.
- [2] K. Liu, M. Sakurai, and M. Aono, "ZnO-based ultraviolet photodetectors," *Sensors*, vol. 10, no. 9, pp. 8604–8634, 2010.
- [3] M. Ahmad and J. Zhu, "ZnO based advanced functional nanostructures: synthesis, properties and applications," *Journal of Materials Chemistry*, vol. 21, no. 3, pp. 599–614, 2011.
- [4] K.-K. Kim, S. Niki, J.-Y. Oh et al., "High electron concentration and mobility in Al-doped *n*-ZnO epilayer achieved via dopant activation using rapid-thermal annealing," *Journal of Applied Physics*, vol. 97, no. 6, Article ID 066103, 2005.
- [5] A. Sedky, T. A. El-Brollosy, and S. B. Mohamed, "Correlation between sintering temperature and properties of ZnO ceramic varistors," *Journal of Physics and Chemistry of Solids*, vol. 73, no. 3, pp. 505–510, 2012.
- [6] S. Öztürk, N. Kiliç, N. Taştaltın, and Z. Z. Öztürk, "A comparative study on the NO<sub>2</sub> gas sensing properties of ZnO thin films, nanowires and nanorods," *Thin Solid Films*, vol. 520, no. 3, pp. 932–938, 2011.
- [7] A. Alias, K. Hazawa, N. Kawashima, H. Fukuda, and K. Uesugi, "Fabrication of ZnO thin-film transistors by chemical vapor deposition method," *Japanese Journal of Applied Physics*, vol. 50, no. 1, Article ID 01BG05, 2011.
- [8] N. Hirahara, B. Onwona-Agyeman, and M. Nakao, "Preparation of Al-doped ZnO thin films as transparent conductive substrate in dye-sensitized solar cell," *Thin Solid Films*, vol. 520, no. 6, pp. 2123–2127, 2012.
- [9] N. Yamamoto, H. Makino, Y. Hirashima et al., "Heat resistance of Ga-doped ZnO thin films for application as transparent electrodes in liquid crystal displays," *Journal of the Electrochemical Society*, vol. 157, no. 2, pp. J13–J20, 2010.
- [10] S. Agrawal, R. Rane, and S. Mukherjee, "ZnO thin film deposition for TCO application in solar cell," *Conference Papers in Energy*, vol. 2013, Article ID 718692, 7 pages, 2013.
- [11] W. L. Dang, Y. Q. Fu, J. K. Luo, A. J. Flewitt, and W. I. Milne, "Deposition and characterization of sputtered ZnO films," *Superlattices and Microstructures*, vol. 42, no. 1-6, pp. 89–93, 2007.
- [12] C.-Y. Tsay, H.-C. Cheng, Y.-T. Tung, W.-H. Tuan, and C.-K. Lin, "Effect of Sn-doped on microstructural and optical properties of ZnO thin films deposited by sol-gel method," *Thin Solid Films*, vol. 517, no. 3, pp. 1032–1036, 2008.
- [13] S. H. Jeong, B. N. Park, S.-B. Lee, and J.-H. Boo, "Study on the doping effect of Li-doped ZnO film," *Thin Solid Films*, vol. 516, no. 16, pp. 5586–5589, 2008.
- [14] Y. Liu, Y. Li, and H. Zeng, "ZnO-based transparent conductive thin films: doping, performance, and processing," *Journal of Nanomaterials*, vol. 2013, Article ID 196521, 9 pages, 2013.
- [15] C. C. Lin, S. L. Young, C. Y. Kung et al., "Effect of Fe doping on the microstructure and electrical properties of transparent ZnO nanocrystalline films," *Thin Solid Films*, vol. 529, pp. 479–482, 2013.
- [16] J. Huso, J. L. Morrison, H. Hoeck et al., "Pressure response of the ultraviolet photoluminescence of ZnO and MgZnO nanocrystallites," *Applied Physics Letters*, vol. 89, no. 17, Article ID 171909, 2006.
- [17] K. K. Zhuravlev, W. M. Hlaing Oo, M. D. McCluskey, J. Huso, J. L. Morrison, and L. Bergman, "X-ray diffraction of Mg<sub>x</sub>Zn<sub>1-x</sub>O and ZnO nanocrystals under high pressure," *Journal of Applied Physics*, vol. 106, Article ID 013511, 2009.
- [18] D. Banerjee, J. Y. Lao, D. Z. Wang et al., "Synthesis and photoluminescence studies on ZnO nanowires," *Nanotechnology*, vol. 15, no. 3, pp. 404–409, 2004.
- [19] B. Lin, Z. Fu, and Y. Jia, "Green luminescent center in undoped zinc oxide films deposited on silicon substrates," *Applied Physics Letters*, vol. 79, no. 7, pp. 943–945, 2001.
- [20] G. Kenanakis, M. Androulidaki, D. Vernardou, N. Katsarakis, and E. Koudoumas, "Photoluminescence study of ZnO structures grown by aqueous chemical growth," *Thin Solid Films*, vol. 520, no. 4, pp. 1353–1357, 2011.
- [21] K. W. Liu, R. Chen, G. Z. Xing, T. Wu, and H. D. Sun, "Photoluminescence characteristics of high quality ZnO nanowires and its enhancement by polymer covering," *Applied Physics Letters*, vol. 96, no. 2, Article ID 023111, 2010.
- [22] M. D. McCluskey and S. J. Jokela, "Defects in ZnO," *Journal of Applied Physics*, vol. 106, no. 7, Article ID 071101, 2009.

## Research Article

# Obtaining Highly Crystalline Barium Sulphate Nanoparticles via Chemical Precipitation and Quenching in Absence of Polymer Stabilizers

Ángela B. Sifontes,<sup>1</sup> Edgar Cañizales,<sup>2</sup> Jhoan Toro-Mendoza,<sup>3</sup>  
Edward Ávila,<sup>1</sup> Petra Hernández,<sup>1</sup> Blas A. Delgado,<sup>2</sup> G. Brenda Gutiérrez,<sup>1</sup>  
Yraida Díaz,<sup>3</sup> and Eliandreina Cruz-Barríos<sup>3</sup>

<sup>1</sup>Centro de Química, Instituto Venezolano de Investigaciones Científicas (IVIC), Apartado 20632, Caracas 1020-A, Venezuela

<sup>2</sup>Área de Análisis Químico Inorgánico, PDVSA, INTEVEP, Los Teques 1070-A, Venezuela

<sup>3</sup>Centro de Estudios Interdisciplinarios de la Física, Instituto Venezolano de Investigaciones Científicas (IVIC), Apartado 20632, Caracas 1020-A, Venezuela

Correspondence should be addressed to Ángela B. Sifontes; [angelasifontes@gmail.com](mailto:angelasifontes@gmail.com)

Received 26 November 2014; Revised 9 February 2015; Accepted 10 February 2015

Academic Editor: Yong Zhu

Copyright © 2015 Ángela B. Sifontes et al. This is an open access article distributed under the Creative Commons Attribution License, which permits unrestricted use, distribution, and reproduction in any medium, provided the original work is properly cited.

Here we report the synthesis of barium sulphate ( $\text{BaSO}_4$ ) nanoparticles from  $\text{Ba}(\text{OH})_2/\text{BaCl}_2$  solutions by a combined method of precipitation and quenching in absence of polymer stabilizers. Transmission electron microscopy (HRTEM), Fourier transforms infrared spectroscopy (FTIR), and X-ray diffraction (XRD) were employed to characterize the particles. The Scherrer formula was applied to estimate the particle size using the width of the diffraction peaks. The obtained results indicate that the synthesized material is mainly composed of nanocrystalline barite, with nearly spherical morphology, and diameters ranging from 4 to 92 nm. The lattice images of nanoparticles were clearly observed by HRTEM, indicating a high degree of crystallinity and phase purity. In addition, agglomerates with diameters between 20 and 300 nm were observed in both lattice images and dynamic light scattering measurements. The latter allowed obtaining the particle size distribution, the evolution of the aggregate size in time of  $\text{BaSO}_4$  in aqueous solutions, and the sedimentation rate of these solutions from turbidimetry measurements. A short discussion on the possible medical applications is presented.

## 1. Introduction

The baryte group consists of baryte, celestine, anglesite, and anhydrite. Baryte is a sulfate of barium with chemical formula  $\text{BaSO}_4$ . It is generally white or colorless, chemically inert, insoluble in water, with high density, and the main source of barium. Although baryte contains a “heavy” metal (barium), it is not considered to be a toxic chemical reagent by most governments because of its extreme insolubility [1]. Commonly, baryte is used for the production of barium hydroxide for sugar refining and as a white pigment for textiles, paper, and paint [2]. It is also suitable for other purposes due to its high specific gravity (4.5), opaqueness to X-rays, inertness,

and whiteness [3]. Recently, more attention has been paid on the massive production of  $\text{BaSO}_4$  nanoparticles for its multiple applications in the oil industry, electronics, TV screen, glass, car filters, paint industry, and ceramics [4] as well as in medical applications. In particular, barium sulfate suspension in water is used as the universal contrast medium for the examination of the upper gastrointestinal tract [5]. Currently, the development of nanoparticle-based X-ray contrast agents is providing an increasing contribution to the field of diagnostic and molecular imaging. For example, the nanoparticles surface can be modified to enhance their specificity by attaching targeting moieties, increase their circulation half-life by adding appropriate coatings (e.g., polymers, silica), and

improve their functionality by adding other components, including fluorescent markers and therapeutic agents [6]. However, although significant progress has been made in preparing stable nanoparticles, their industrial production can present serious difficulties that limit their potential applications. For example, BaSO<sub>4</sub> nanoparticles tend to form aggregates due to the high ratio surface area-volume. Expensive costs and complex methodologies also attempt against massive industrial production [3].

Among the methods to obtain nanoscaled materials, chemical synthesis has numerous advantages such as simple technique, low costs, less instrumentation, doping, and high yield [4]. These methods could be classified as (a) direct precipitation [7], (b) microemulsion [8], (c) membrane separation [9], and (d) organic modification [10]. In general, particle sizes between 16 and 50 nm can be obtained. Nonetheless, precipitation seems to be the most suitable method due to its simple procedure and ease of mass production, and less apparatus is required [11]. In spite of this, the difficulties in controlling the size, polydispersity, and strong tendency to aggregate could hinder their potential applications [11]. In this sense, it is important to find more efficient methodologies of synthesis. Accordingly, in this paper we report the synthesis and characterization of barium nanoparticles by a chemical precipitation route, in the absence of polymer stabilizers.

## 2. Materials and Methods

**2.1. Chemicals and Instruments.** The starting reagents barium hydroxide, barium chloride, and sulfuric acid were used as received. Double distilled water was used in all experiments. The prepared barium sulfate was characterized by transmission electron microscopy using a JEOL JEM-2100 microscope with LaB<sub>6</sub> filament (accelerating voltage of 200 kV). The samples were prepared by suspending the powders in an ethanol-based liquid and pipetting the suspension onto a carbon/collodion coating. Fourier transform infrared (FT-IR) spectra were measured with a Perkin Elmer 100 spectrometer (in the range of 2000–500 cm<sup>-1</sup>) by incorporating the samples in KBr (1:99 mg) disks to confirm the characteristic vibrational bands. X-ray diffraction (XRD) patterns of BaSO<sub>4</sub> were recorded on a panalytical diffractometer, model X'Pert Pro, and CuK- $\alpha$  radiation in the  $2\theta$  range between 5 and 80°, operating at 40 kV and 20 mA. Phases were identified using the MATCH! 2 program (version 2.2.3, Build 361) Crystal Impact, coupled to the Release 2011 PDF-2 database [12]. PDF card number 024-1035 (or ICSD card number 33730) was used to carry out the Rietveld refinement to all the peaks [13], which were in accordance with the reported values in the literature. The structure of BaSO<sub>4</sub> was refined with the Rietveld (1969) program GSAS [14] using the graphical interface EXPGUI [15]. The peak shapes were modeled using the pseudo-Voigt peak shape function 3, which included the axial divergence correction at low angle [16]. Background was initially determined manually and then modeled using the Chebyshev polynomial function. The isotropic atomic displacement parameters were refined as one overall  $U_{\text{iso}}$  for the nonoxygen atoms starting from a value of 0.05 Å<sup>2</sup>.

TABLE 1: Selected peaks employed to calculate the particles size with Scherrer's equation. These are the nine first peaks that appearance powder pattern of BaSO<sub>4</sub> synthesized.

| $hkl$ | $2\theta/^\circ$ | $d/\text{Å}$ | Int./U.A. | Rel. Int./% | FWHM/ $2\theta^\circ$ |
|-------|------------------|--------------|-----------|-------------|-----------------------|
| 200   | 19.9969          | 4.43666      | 211.47    | 13.68       | 0.0895                |
| 011   | 20.4650          | 4.33622      | 513.75    | 33.24       | 0.0892                |
| 111   | 22.8076          | 3.89586      | 795.40    | 51.46       | 0.0882                |
| 210   | 23.5789          | 3.77013      | 155.81    | 10.08       | 0.0879                |
| 002   | 24.8785          | 3.57606      | 448.89    | 29.04       | 0.0875                |
| 210   | 25.8694          | 3.44128      | 1521.90   | 98.46       | 0.0872                |
| 120   | 26.8582          | 3.31679      | 1090.44   | 70.55       | 0.0870                |
| 211   | 28.7665          | 3.10096      | 1545.73   | 100.00      | 0.0868                |
| 112   | 31.6281          | 2.83364      | 535.66    | 34.65       | 0.0868                |

Nevertheless, one constraint was applied to  $U_{\text{iso}}$  for modeling the isotropic atomic displacement parameters of oxygen atom following riding-model. The mean grain size ( $D$ ) of the prepared BaSO<sub>4</sub> nanoparticles was estimated from X-ray line broadening of the listed reflections in Table 1, using the Scherrer equation [17] ( $D = K\lambda/(\beta \cos \theta)$  where  $\lambda$  is the wavelength of the X-ray radiation,  $K$  is a constant taken as 0.89,  $\theta$  is the diffraction angle, and  $\beta$  (rad) is the full width at half-maximum (FWHM)).

Both initial particle size distribution and particles size variation were characterized by dynamic light scattering measurements (DLS) on a Brookhaven BI 9000AT goniometer. Measurements were carried out at a fixed angle of 90° using a 633 nm laser. The sedimentation rate was obtained from Turbiscan LAB software in scanning mode. The light source is an electro luminescent diode in near infrared (880 nm). Two synchronous optical sensors receive the transmitted light through the sample (180°) and the backscattered light by the sample (45°). The sample was dispersed in a deionized water solution at a phase fraction of 0.1% w/v. The suspension was sonicated during 15 min before measurement.

**2.2. Preparation of the Samples.** The direct precipitation (DP) procedure followed consists in adding a Ba(OH)<sub>2</sub>·8H<sub>2</sub>O solution to BaCl<sub>2</sub>·2H<sub>2</sub>O in presence of water. The molar ratio of Ba(OH)<sub>2</sub> to BaCl<sub>2</sub> was 3:1. The resulting solution was stirred at room temperature while a sulfuric acid solution (50% (v/v)) was added (step 1, precipitation). The precipitated solid material was washed and filtered four times with hot distilled water (step 2). The sample was frozen at -26°C for 24 hours. Subsequently, the supernatant liquid was carefully decanted and then a volume of distilled water was added again. This procedure was repeated 5 times. The final step involved a freeze-dry cycle and was oven-dried at 105°C for 12 hours (step 3, purification) [18]. All the experiments were performed three times in order to observe reproducibility.

## 3. Results and Discussion

Figure 1 shows the XRD pattern and final Rietveld plot of the synthesized sample. It is shown that the solid is composed of baryte. The BaSO<sub>4</sub> crystalized in orthorhombic crystals, space

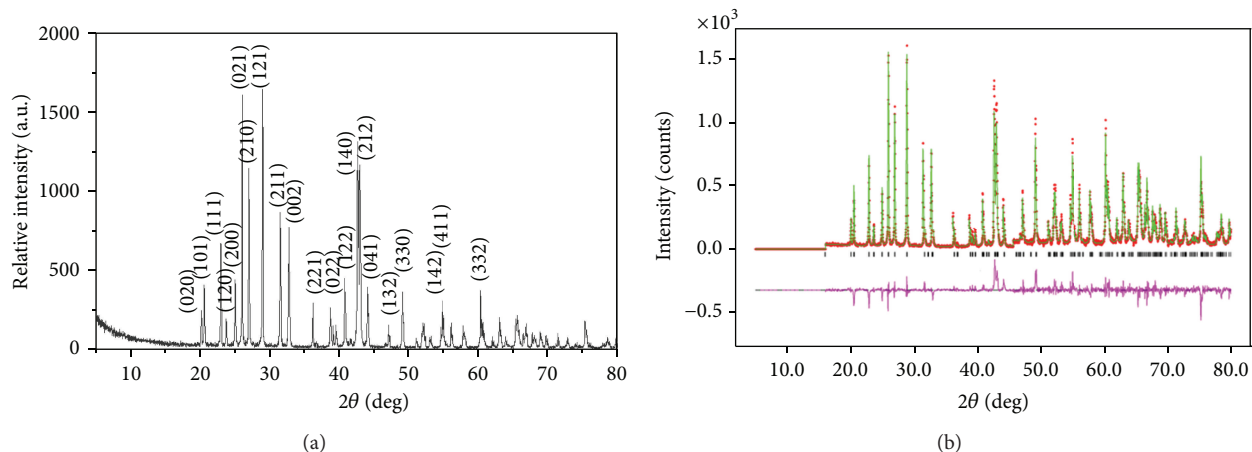


FIGURE 1: XRD pattern of synthesized sample (a) and final Rietveld plot for  $\text{BaSO}_4$  (b). The continuous green line represents the calculated pattern and the red discontinuous line is the observed pattern.

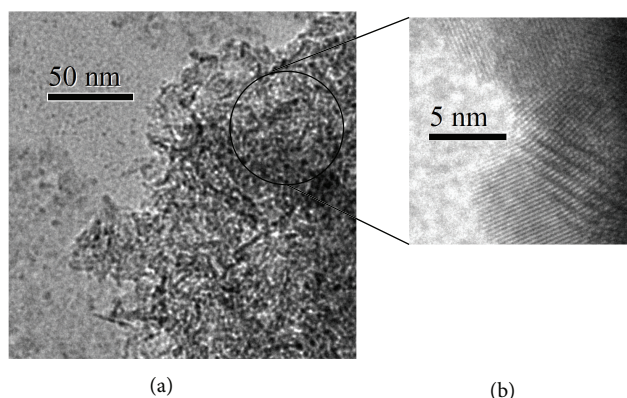


FIGURE 2: TEM image of  $\text{BaSO}_4$  nanoparticles (a); HRTEM image showing lattice fringes of  $\text{BaSO}_4$  nanoparticles (b).

group  $Pnma$ , with cell parameters  $a = 8.875 \text{ \AA}$ ,  $b = 5.453 \text{ \AA}$ , and  $c = 7.154 \text{ \AA}$ . The final Rietveld refinement with the reported model gave figures of merit:  $R_p = 0.1135$ ,  $R_{wp} = 0.1433$ ,  $R_{exp} = 0.014$ ,  $R_F^2 = 0.0945$  (249 reflections), and  $\chi^2 = 1.41$ . Finally, the Scherrer equation was used to estimate the particle size by averaging the value of FWHM for the first nine lines of the powder pattern of  $\text{BaSO}_4$  (see Table 1). Thus, the average particle size estimated for the  $\text{BaSO}_4$  synthesized in this work was 91.72 nm.

TEM and HRTEM images (Figures 2–6) show that the sample was composed of both isolated and aggregated particles. The morphology of  $\text{BaSO}_4$  particles is nearly spherical. The nanoparticles size determined from micrographies is between 2.6 and 20 nm, with an average size of 14.5 nm. Besides, large (>20 nm) fully crystallized structures are observed. Typical sizes of aggregates were found to be about 11–300 nm (Figure 3).

In Figure 4 HRTEM analysis shows that the lattice fringes with an interlayer distance of 0.327 nm is close to the 0.331 nm lattice spacing of the  $\{210\}$  crystal planes of barite

phase. This was confirmed by fast Fourier transformation (FFT) patterns, which is also in accordance with XRD results. For this study, noise reduction was performed on the square-labeled area of Figure 4(a). Masking was applied on the intense spots of the FFT power spectrum. The resulting image after performing inverse FFT on the masked power spectrum is showed in Figure 4(d).

In Figure 5(a) (nanoparticles 1, 2) HRTEM analysis shows that the lattice fringes with an interlayer distance of 0.338 nm correspond to lattice spacing of the (210) crystal planes of  $\text{BaSO}_4$ , which is in accordance with XRD results. Figures 6(b) and 6(c) show a FFT of Figure 5(a), and the diffraction points can be indexed to the (210) plane. Masking was also applied on Figures 5(b) and 5(c), specifically on the intense spots of the FFT power spectrum. The resulting image (Figures 5(d) and 5(e)) was obtained after performing inverse FFT on the masked power spectrum (Figures 5(f) and 5(g)).

In the HRTEM image (Figure 6), the planar spacing obtained is 0.355 nm, corresponding to spacing for (200) planes of orthorhombic structure  $\text{BaSO}_4$ . All the planar

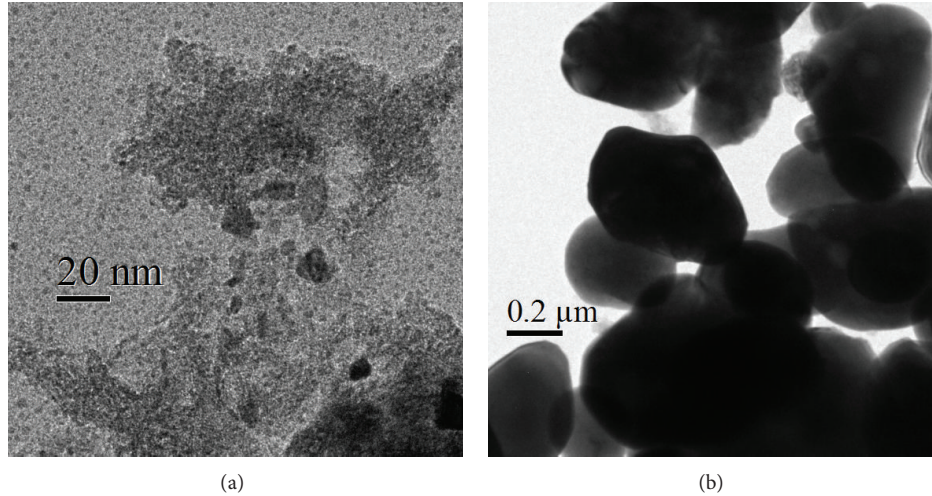


FIGURE 3: TEM image of BaSO<sub>4</sub> nanoparticles (a); typical aggregates (b).

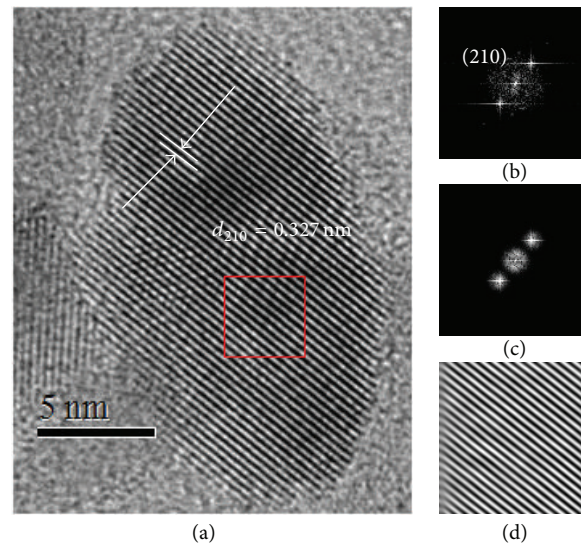


FIGURE 4: HRTEM image of BaSO<sub>4</sub> nanoparticle (a); FFT power spectrum (b); masked power spectrum FFT (c); image after performing inverse FFT on the masked power spectrum (d).

spacing determined from HRTEM images are in accordance with the database of Joint Committee on Powder Diffraction Standards (JCPDS) card 024-1035.

Figure 7 shows the FT-IR spectra of the synthesized BaSO<sub>4</sub> nanoparticles. It was previously mentioned that the sulfate group has four fundamental vibrational modes attributed to one nondegenerate mode ( $\nu_1$ ), one doubly degenerate mode ( $\nu_2$ ), and two triply degenerate modes ( $\nu_3$  and  $\nu_4$ ). In general, the IR spectrum of baryte exhibits several significant bands [19]. Two intense bands correspond to asymmetric stretching and bending ( $\nu_3$  and  $\nu_4$ ), and two weak ones correspond to symmetric stretching and bending ( $\nu_1$  and  $\nu_2$ ) [19]. In the FT-IR spectra the bands centered at 1073–1185 cm<sup>-1</sup> and the shoulder at 982 cm<sup>-1</sup> were assigned to symmetric stretching vibration of SO<sub>4</sub><sup>2-</sup> group. At 1636 cm<sup>-1</sup>

the stretching vibration  $\nu_3$  of SO<sub>4</sub><sup>2-</sup> group was identified. The peaks obtained at 609 and 637 cm<sup>-1</sup> were attributed to the out-of-plane bending vibration of the SO<sub>4</sub><sup>2-</sup> [10, 19]. The absorption peaks appeared at 3420 cm<sup>-1</sup> are due to antisymmetric stretching vibrations of H<sub>2</sub>O molecules localized on vacant sites of Ba. The peaks around 2000 cm<sup>-1</sup> are overtones and a combination of stretching and bending vibrations bands of the sulphur-oxygen [20].

**3.1. Particle Size Distribution, Aggregates Size Evolution, and Sedimentation Rate.** Figure 8 shows the particle size distribution from dynamic light scattering (DLS) measures of an aqueous suspension of BaSO<sub>4</sub> nanoparticles. As can be observed, the main peak appears around 800 nm with an average size of 2.23 ± 0.72 μm. Even though the micrographies

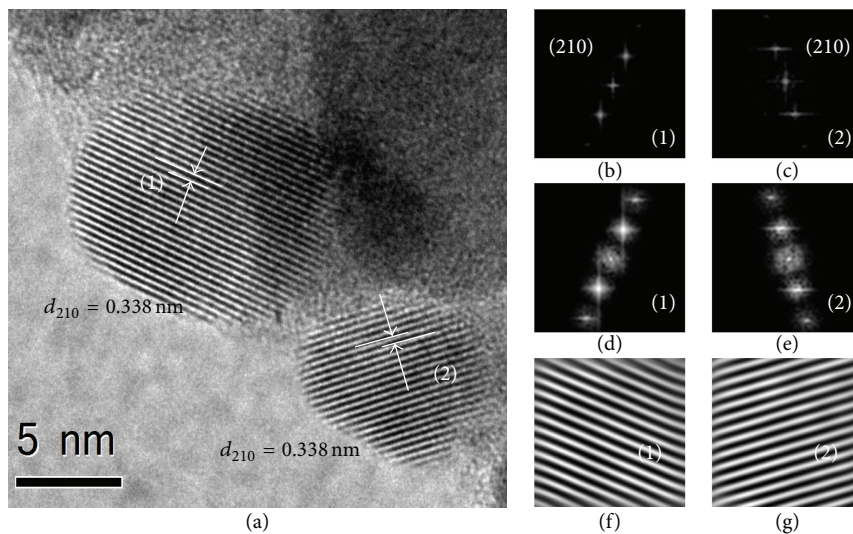


FIGURE 5: HRTEM image of BaSO<sub>4</sub> nanoparticles (a); FFT image (b) (particle 1), (c) (particle 2); masked power spectrum FFT (c) (particle 1), (d) (particle 2); image after performing inverse FFT on the masked power spectrum (c) and (d).

indicate a particle size less than 100 nm, the distribution shows particles sizes above 5 microns, an indicative that DLS yields an average radius of aggregates formed by several particles. The strong tendency to form aggregates was corroborated and the results are shown in Figure 9, where the time evolution of both radius and percentage of polydispersity is plotted. The average size evolves linearly with time from 1200  $\mu\text{m}$  to 4200  $\mu\text{m}$  in 1 h. However, the percentage of polydispersity fluctuates around 30%.

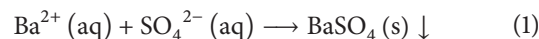
Due to the large size of aggregates, it is expected to observe sedimentation and the results from turbidimetry can be observed in Figure 10. The photon mean free path ( $l$ ) represents the mean distance travelled by photons before undergoing a diffusion phenomenon. Thus, the measurement is performed by the Turbiscan by sending a light beam through the cell and detecting the photons crossing the dispersion, without being diffused. Therefore as more photons cross the cell, more important is the  $l$  value and the sample is more translucent, an indicative that less particles are in the beam path. The initial slope of Figure 10, corresponding to the sedimentation rate, was 412  $\mu\text{m}/\text{min}$ , with a correlation coefficient of 0.99. The total average sedimentation rate in a 60 min measurement was 171  $\mu\text{m}/\text{min}$ .

The combined effect of forming aggregates and sedimentation could limit possible medical applications of BaSO<sub>4</sub> nanoparticles. Nevertheless, this study was processed without any additives (including stabilizers, antioxidants, and lubricants). In this sense, in general, barium sulfate suspension oral for gastric and colonic radiological work, containing a physiologically inert stabilizer, consists of a solution of a water-soluble cellulose ether and carboxymethylcellulose and also contains a suitable penetrant of cationic origin as lauryl sulfoacetate [21]. Besides, in order to improve the possibilities of application, further studies in particle-particle interactions and the main mechanisms responsible for coarsening are necessary to implement new methodologies to obtain more kinetically stable systems. In this sense, our procedure could

be optimized in order to low the polydispersity index around a particle size below 10 nm. It is also noticeable that the starting reagents have low impact toxicity, compared to others which, in some cases, make use of benzene [22]. This latter is an additional advantage of our procedure in order to use the synthesized nanoparticles in medical applications.

**3.2. Formation Mechanism of BaSO<sub>4</sub> Nanoparticles.** The synthesis of barium sulfate was carried out using a mix of Ba(OH)<sub>2</sub>/BaCl<sub>2</sub>, where the barium chloride solution was added to increase the concentration of Ba<sup>2+</sup> ions (in excess). Subsequently, with the addition of SO<sub>4</sub><sup>2-</sup> (H<sub>2</sub>SO<sub>4</sub>), BaSO<sub>4</sub> crystals were gradually formed.

The increase in pH could result in an increase in the negative charge of BaSO<sub>4</sub>. According to Zhang et al., this could be attributed to the adsorption of OH<sup>-</sup> ions on the positive charge centers of BaSO<sub>4</sub> particles [23]. The reaction of barium (Ba<sup>2+</sup>) and sulphate (SO<sub>4</sub><sup>2-</sup>) ions into barium sulphate (BaSO<sub>4</sub>) is [20, 24, 25]



In general, a precipitation process is described by processes that include the creation of a supersaturation level followed by the generation of nuclei (nucleation) and the subsequent growth [8]. A number of secondary processes like aging, ripening, agglomeration, and breakage might occur depending on the nature of the process itself and the chemical compound [8]. Moreover, in a highly supersaturated solution the instability of the system will result in a fast local concentration fluctuation [26]. Basically, there are three variables that govern the rate of nucleation: the temperature  $T$ , the degree of supersaturation  $S$ , and the surface energy  $\sigma$ . In this sense, if the supersaturation ratio is increased and the surface energy is decreased, the result is a higher nucleation rate, which finally leads to the formation of particles of smaller size [27, 28].

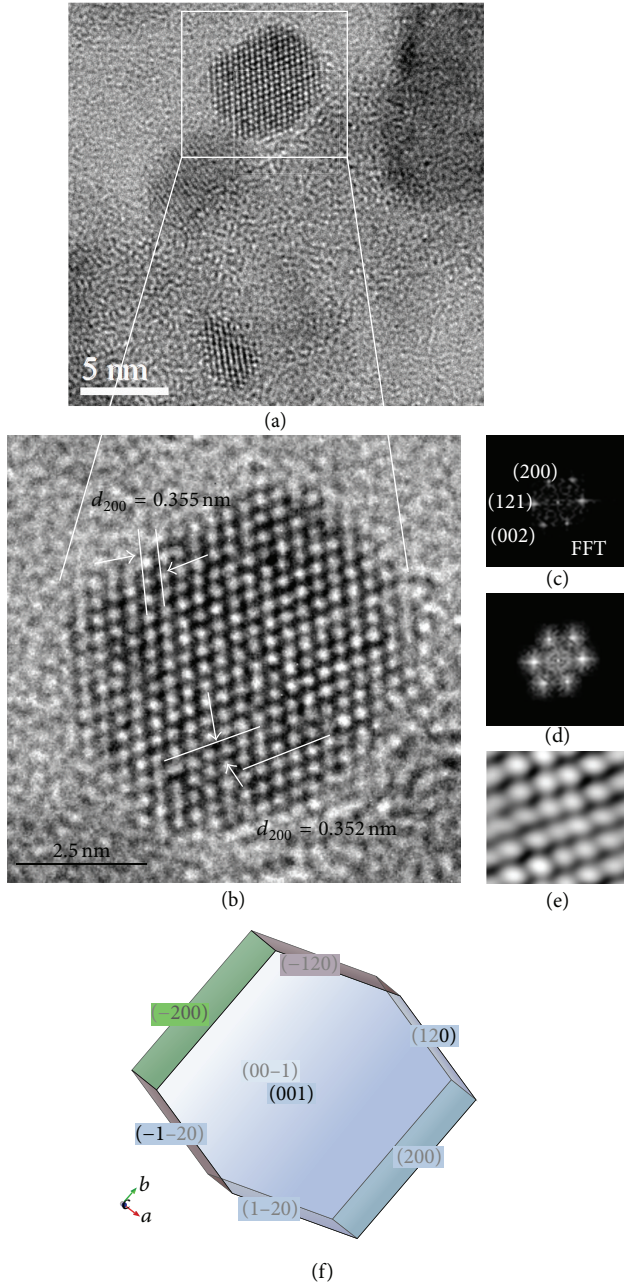


FIGURE 6: HRTEM image of BaSO<sub>4</sub> nanoparticle (a); HRTEM image of BaSO<sub>4</sub> nanoparticle (b); a magnification of the section marked with a white square in (a); FFT image (c); masked power spectrum FFT (d); image after performing inverse FFT on the masked power spectrum (e). A crystallographic representation of BaSO<sub>4</sub> crystal (f).

The synthesis process involves as second step a quenching. Quenching is simply cooling rapidly to a lower temperature,  $-26^{\circ}\text{C}$ . The final step in the precipitation process was an artificial aging at  $-26^{\circ}\text{C}$  (aging above room temperature). Temperature has a significant influence on solubility and *crystal growth* of barium sulphate [29]. It is then expected that the growth of particle size is stopped by quenching with cold water.

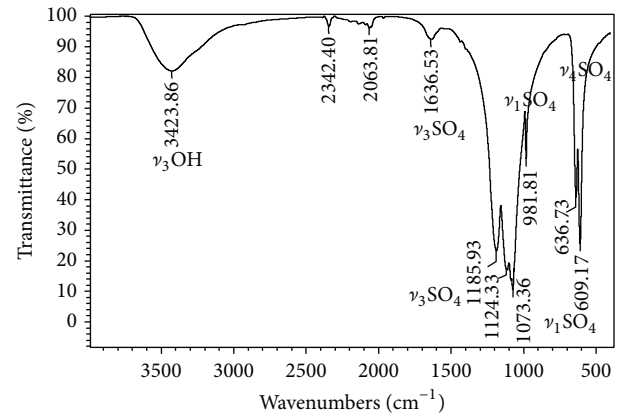


FIGURE 7: FT-IR spectra of BaSO<sub>4</sub> nanoparticles.

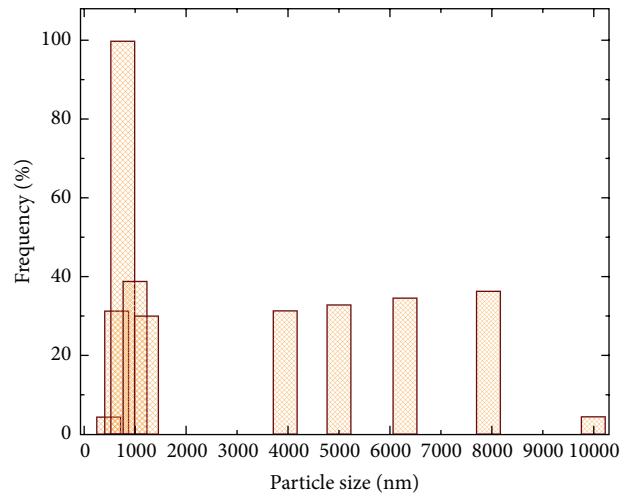


FIGURE 8: Particle size distribution of a BaSO<sub>4</sub>/W suspension (0.1% w/v) determined by dynamic light scattering.

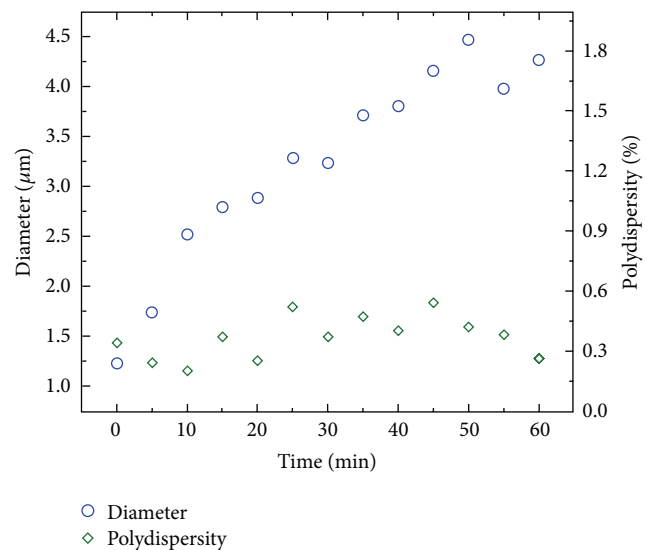


FIGURE 9: Particle size variation of a BaSO<sub>4</sub>/W suspension (0.1% w/v) determined by dynamic light scattering.

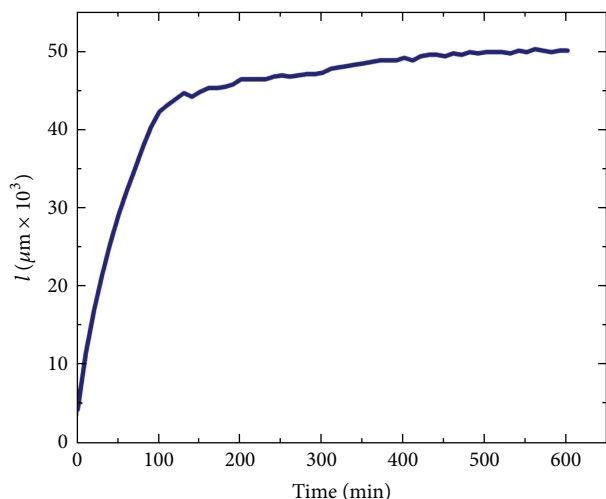


FIGURE 10: Sedimentation rate obtained from the initial slope of the photon mean free path ( $l$ ) as a function of time.

The results presented here prove that barium sulfate nanoparticles can be prepared in the absence of polymers stabilizers polymeric employing a simple methodology. Moreover, the nanomaterial synthesized has applications as a potential contrast agent for X-ray examination.

#### 4. Conclusions

Barium sulphate nanoparticles were synthesized using a precipitation method in absence of polymer stabilizers or solvents. The XRD study shows that the synthesized nanoparticles crystallize in orthorhombic system with space group *Pnma*. This method allowed obtaining high purity, spherical, and morphologically homogeneous nanoparticles. X-ray diffraction, transmission electron microscope (TEM), and high resolution transmission electron microscope (HRTEM) measurements confirmed an average particle size in the range from 4 to 92 nm and agglomerates with diameters between 20 and 300 nm. FTIR study shows the presence of the sulphate group in the synthesized nanoparticles. Dynamic light scattering and turbidimetry measurement indicates a strong tendency of nanoparticles to form aggregates and precipitate in aqueous solution. Finally, this methodology can be employed to synthesize BaSO<sub>4</sub> nanoparticles for possible applications as a potential contrast agent for X-ray examination.

#### Conflict of Interests

The authors declare that there is no conflict of interests regarding the publication of this paper.

#### Acknowledgment

The authors acknowledge financial support by IVIC through project 1077 and technical assistance of Lic. Liz Cubillán (FTIR).

#### References

- [1] J. S. Hanor, "Barite-celestine geochemistry and environments of formation," *Reviews in Mineralogy and Geochemistry*, vol. 40, pp. 193–275, 2000.
- [2] J. Dana and W. Ford, *Dana's Manual of Mineralogy For the Student of Elementary Mineralogy, the Mining Engineer, the Geologist, the Prospector, the Collector, etc*, John Wiley & Sons, New York, NY, USA, 14th edition, 1929.
- [3] Y. Shen, C. Li, X. Zhu, A. Xie, L. Qiu, and J. Zhu, "Study on the preparation and formation mechanism of barium sulphate nanoparticles modified by different organic acids," *Journal of Chemical Sciences*, vol. 119, no. 4, pp. 319–324, 2007.
- [4] V. Ramaswamy, R. M. Vimalathithan, and V. Ponnusamy, "Preparation of barium sulphate nanocrystals in ethanol—water mixed solvents," *Journal of Ceramic Processing Research*, vol. 12, no. 2, pp. 173–175, 2011.
- [5] D. Sutton, *A Textbook of Radiology and Imaging*, Churchill Livingstone, London, UK, 1980.
- [6] J. C. de la Vega and U. O. Häfeli, "Utilization of nanoparticles as X-ray contrast agents for diagnostic imaging applications," *Contrast Media & Molecular Imaging*, 2014.
- [7] M. Ismaiel and I. Mostafa, "Synthesis of BaSO<sub>4</sub> nanoparticles by precipitation method using polycarboxylate as a modifier," *American Journal of Nanotechnology*, vol. 2, pp. 106–111, 2011.
- [8] D. Adityawarman, A. Voigt, P. Veit, and K. Sundmacher, "Precipitation of BaSO<sub>4</sub> nanoparticles in a non-ionic microemulsion: identification of suitable control parameters," *Chemical Engineering Science*, vol. 60, no. 12, pp. 3373–3381, 2005.
- [9] G. Wu, H. Zhou, and S. Zhu, "Precipitation of barium sulfate nanoparticles via impinging streams," *Materials Letters*, vol. 61, no. 1, pp. 168–170, 2007.
- [10] A. Gupta, P. Singh, and C. Shivakumara, "Synthesis of BaSO<sub>4</sub> nanoparticles by precipitation method using sodium hexa metaphosphate as a stabilizer," *Solid State Communications*, vol. 150, no. 9–10, pp. 386–388, 2010.
- [11] M. I. Nieto, C. Tallón, and R. Moreno, "Synthesis of gamma-alumina nanoparticles by freeze drying," *Advances in Science and Technology*, vol. 45, pp. 223–230, 2006.
- [12] H. Putz, *MATCH 2-Phase Identification from Powder Diffraction, Version 2.2.3*, Crystal Impact, Bonn, Germany, 2014.
- [13] H. M. Rietveld, "A profile refinement method for nuclear and magnetic structures," *Journal of Applied Crystallography*, vol. 2, pp. 65–71, 1969.
- [14] A. C. Larson and R. B. von Dreele, *GSAS: General Structure Analysis System*, Software, The Los Alamos National Laboratory, Los Alamos, NM, USA, 2007.
- [15] B. H. Toby, "EXPGUI, a graphical user interface for GSAS," *Journal of Applied Crystallography*, vol. 34, no. 2, pp. 210–213, 2001.
- [16] L. W. Finger, D. E. Cox, and A. P. Jephcoat, "A correction for powder diffraction peak asymmetry due to axial divergence," *Journal of Applied Crystallography*, vol. 27, no. 6, pp. 892–900, 1994.
- [17] S. Phoka, P. Laokul, E. Swatsitang, V. Promarak, S. Seraphin, and S. Maensiri, "Synthesis, structural and optical properties of CeO<sub>2</sub> nanoparticles synthesized by a simple polyvinyl pyrrolidone (PVP) solution route," *Materials Chemistry and Physics*, vol. 115, no. 1, pp. 423–428, 2009.
- [18] W. Armarego and D. Perrin, *Laboratory Chemical*, Butterworth Heinemann, Oxford, UK, 4th edition, 1996.

- [19] B. Prameena, G. Anbalagan, V. Sangeetha, S. Gunasekaran, and G. R. Ramkumaar, "Behaviour of Indian natural baryte mineral," *International Journal of ChemTech Research*, vol. 5, no. 1, pp. 220–231, 2013.
- [20] J. Manam and S. Das, "Thermally stimulated luminescence studies of undoped, Cu and Mn doped BaSO<sub>4</sub> compounds," *Indian Journal of Pure and Applied Physics*, vol. 47, no. 6, pp. 435–438, 2009.
- [21] R. B. Garland, Patent US3236735 A, 1962.
- [22] V. Ramaswamy and R. M. Vimalathithan, "Ponnusamy synthesis of monodispersed barium sulphate nanoparticles using water-benzene mixed solvent," *Advanced Materials Letters*, vol. 3, pp. 29–33, 2012.
- [23] M. Zhang, B. Zhang, X. Li, Z. Yin, and X. Guo, "Synthesis and surface properties of submicron barium sulfate particles," *Applied Surface Science*, vol. 258, no. 1, pp. 24–29, 2011.
- [24] R. Kieffer, D. Mangin, F. Puel, and C. Charcosset, "Precipitation of barium sulphate in a hollow fiber membrane contactor: part II the influence of process parameters," *Chemical Engineering Science*, vol. 64, no. 8, pp. 1885–1891, 2009.
- [25] A. A. Öncül, K. Sundmacher, A. Seidel-Morgenstern, and D. Thévenin, "Numerical and analytical investigation of barium sulphate crystallization," *Chemical Engineering Science*, vol. 61, no. 2, pp. 652–664, 2006.
- [26] A. Myerson, *Handbook of Industrial Crystallization*, Butterworth-Heinemann, Boston, Mass, USA, 1993.
- [27] N. Tavare, *Industrial Crystallization: Process Simulation Analysis and Design*, Plenum Press, New York, NY, USA, 1995.
- [28] A. Randolph and M. Larson, *Theory of Particulate Processes*, Academic Press, San Diego, Calif, USA, 2nd edition, 1988.
- [29] A. B. B. Merdhah, "Laboratory study on precipitation of barium sulphate in Malaysia," *The Open Petroleum Engineering Journal*, vol. 2, pp. 1–11, 2009.

## Research Article

# A Slope-Adapted Sample-Tilting Method for Profile Measurement of Microstructures with Steep Surfaces

Hui Fang, Bin Xu, Wei Chen, Hairong Tang, and Shiping Zhao

*School of Manufacturing Science and Engineering, Sichuan University, 24 South No. 1 Ring Road, Chengdu 610065, China*

Correspondence should be addressed to Bin Xu; [bin\\_xu@outlook.com](mailto:bin_xu@outlook.com)

Received 29 January 2015; Revised 21 April 2015; Accepted 23 April 2015

Academic Editor: Yong Zhu

Copyright © 2015 Hui Fang et al. This is an open access article distributed under the Creative Commons Attribution License, which permits unrestricted use, distribution, and reproduction in any medium, provided the original work is properly cited.

This paper presents a slope-adapted sample-tilting method for the profile measurement of microstructures with steep surfaces. Distinct from the traditional scanning method that has the restriction of a maximum detectable angle, this method corrects the sample-stylus relative angle during the measurement of the steep surface to eliminate the profile deviation and the scanning blind region. The performance of the proposed method was verified by simulations that measured the surface profiles of a trapezoidal microstructure and a spherical microstructure, finding maximum errors of  $0.15\ \mu\text{m}$  and  $1.71\ \mu\text{m}$ , respectively, compared to  $3.63\ \mu\text{m}$  and  $7.85\ \mu\text{m}$  using the traditional scanning method. The proposed method enables accurate profile measurement and quality control of microstructures with steep surfaces.

## 1. Introduction

Precision microstructures with steep surfaces are widely used in precision industries and have recently become a trend in new generation manufacturing technology [1–4]. Such microstructures, as shown in Figure 1(a), including microlenses employed by Shack-Hartmann wavefront sensors, micropisms of a light guide plate in solar energy systems, and microgrooves in aerospace micropropulsion engines, typically have critical dimensions from several to several hundred microns and a maximum local slope of up to 90 degrees [5–9]. Accurate profile measurement is important because the geometric quality of the microstructure surfaces dominates the working performance of microstructure-based devices. The main difficulty in profiling microstructures with steep surfaces lies in the maximum detectable angle of the profiling system. In a stylus-based profiling system with a maximum detectable angle of 45 or 60 degrees [4, 10], the probing point tapers from the stylus tip to its flanks, resulting in the profile deviations shown in Figure 1(b). Using an optical profiling system, such as an autofocus profilometer or interferometer, with a maximum detectable angle of 15 or 30 degrees, it is difficult to achieve a useful reflection signal from the steep surface [4, 11].

Over the years, work has been conducted to resolve this issue. Ju et al. developed a novel scanning tunneling microscope to measure the surface profile of a microstructure with a 90-degree steep sidewall [12, 13]. Marinello et al. combined the methods of controlled tilting and image processing to increase the maximum detectable slope of an optical profiler [14]. Cho et al. built a three-dimensional atomic force microscope (AFM) to measure the surface roughness of undercut and sidewall structures [15]. Pan et al. proposed a stitching double-tilt image method to measure sub-50 nm line widths employing an AFM system [16]. The above approaches manually tilt the sample and measure the sample repeatedly under different tilt angles, and the entire surface profile is reconstructed by a data fusion algorithm. However, the measurement process is time consuming, and the measurement errors introduced by the manual sample-tilting and the data fusion algorithm are too strong to be eliminated by compensation. Henselmans et al. designed a noncontact measurement machine to scan the surface profile of freeform optics [17], and Weckenmann et al. proposed a sensor tilting method to enhance the measurement capability of microstructures [18, 19]. These two methods appropriately tilt the probing sensor when scanning a steep surface. However, as the lateral resolution of the employed probes is limited

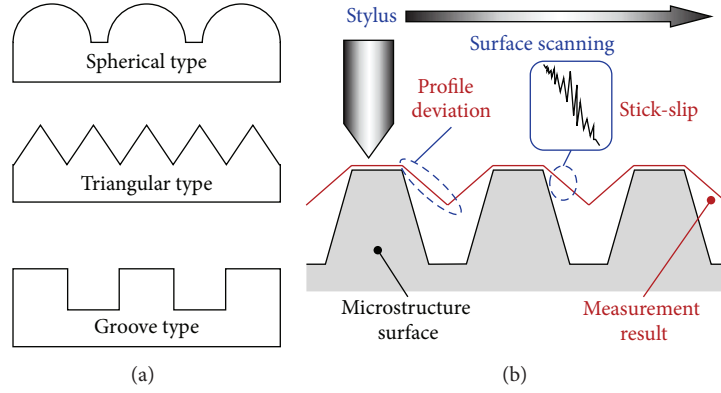


FIGURE 1: Stylus profiling microstructures. (a) Representative microstructures with steep surfaces. (b) Schematic of measurement deviation.

to the order of hundred microns, the application is unable to measure microstructures profiles with critical dimensions from several to several hundred microns. Although many measurement systems and methods have been established for the profile measurement of microstructures with steep surfaces [11, 20–24], a rapid, simple, and cost-effective measurement method is desired.

This paper presents a slope-adapted sample-tilting method for the profile measurement of microstructures with steep surfaces. First, a novel stylus-based profiling system that implements the proposed method is reported. Relevant theoretical work that underlies the realization of the system is described, including the principle of the proposed method and strategies to control the planar scanner and to tilt the sample. Simulations of the profiling of the steep surfaces of two microstructures were then carried out to verify the feasibility of the proposed method.

## 2. Measurement System and Slope-Adapted Sample-Tilting Method

Figure 2 shows the schematic of the stylus-based profiling system designed to implement the proposed method. The system consists of a displacement sensor with a microstylus as a Z-direction scanner, an X motorized driven stage for planar scanning, and a rotating spindle to adjust the sample-stylus relative angle. The system has a solid base plate and a bridge, both made of granite. The entire system is located on a vibration isolation table, so that the measurement would not be affected by external vibrations. The displacement sensor, which measures the axial motion of the microstylus in the Z-direction, is installed on the granite bridge by manual XYZ stages. The X motorized driven stage with a sample is mounted on the center of the spindle rotary table. The surfaces of the X motorized driven stage and the turntable are set parallel and perpendicular to the vibration-isolation table surface, respectively.

As shown in Figure 3, the slope-adapted sample-tilting method adjusts the sample-stylus relative angle during surface profile measurement. This method enables the contact

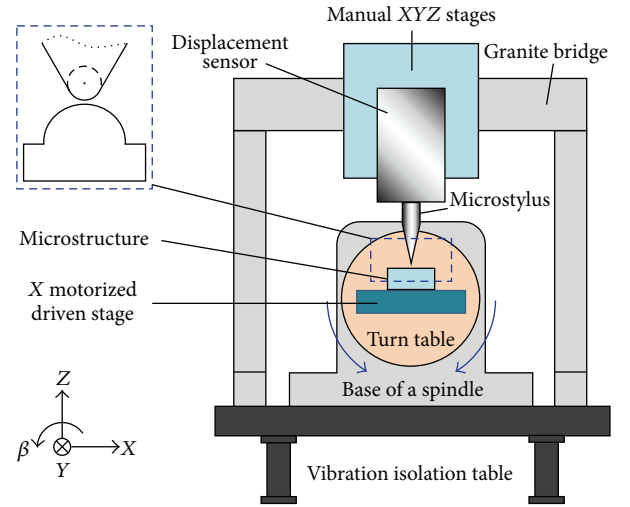


FIGURE 2: Schematic of the measurement system to implement the proposed method.

point to stay at the stylus tip and makes the profile measurement fulfill the requirement of the maximum detectable angle of the system, thereby eliminating the profile deviation.

Before measurement, the offset error of the sensor output should be calibrated by testing a master cylinder [23]. After the calibration, the sensor output is the distance from the radius center of the stylus tip to the rotation axis of the spindle. As shown in Figure 4(a), the profile represented by the scanning results,  $P'_i$ , is an envelope of the sample surface with a distance  $r$ , which is the tip radius of the stylus. The scanning results,  $P'_i$ , are expressed as

$$\begin{bmatrix} P'_1 \\ P'_2 \\ P'_3 \\ \vdots \\ P'_i \end{bmatrix} = \begin{bmatrix} P'_{1-X} & P'_{1-Z} \\ P'_{2-X} & P'_{2-Z} \\ P'_{3-X} & P'_{3-Z} \\ \vdots & \vdots \\ P'_{i-X} & P'_{i-Z} \end{bmatrix}, \quad (1)$$

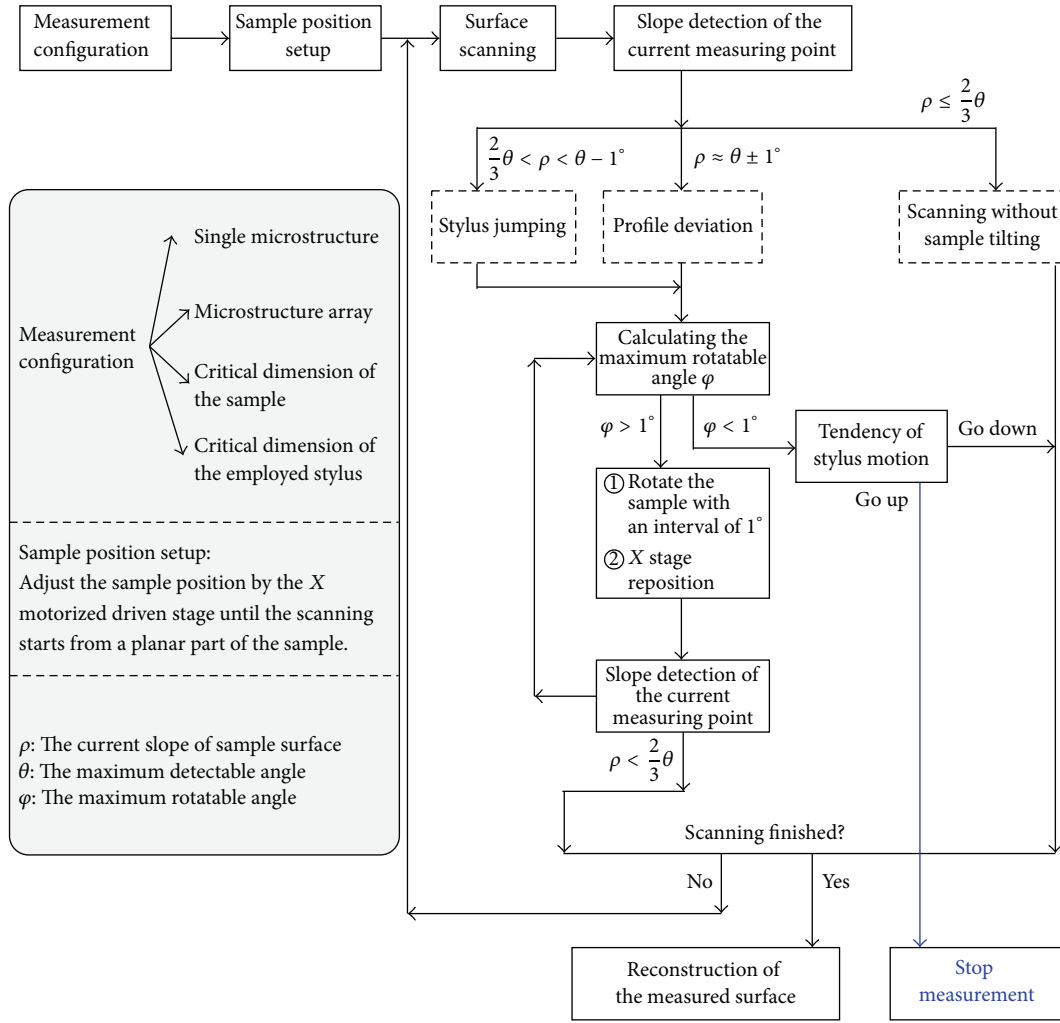


FIGURE 3: Flowchart of the slope-adapted sample-tilting method.

where  $P'_{i-X}$  is obtained from the X motorized driven stage and  $P'_{i-Z}$  is the output of the displacement sensor.

The profile measurement starts from a flat part of the sample surface, and the scanning interval along the X-direction is assumed to be  $\Delta x$ . After a few points were measured, the local slope,  $\rho_i$ , is detected for the current measuring point  $P_i$ . Then,  $\rho_i$  is compared with the maximum detectable angle denoted by  $\theta$ . Generally,  $\theta$  is determined by the included angle of the stylus flank. In some cases, it is desired that  $\theta$  be smaller than this value, such as two-thirds of  $\theta$ , to avoid the phenomenon of stylus jumping. If  $\rho_i$  is in the one degree tolerance range of  $\theta$ , it is reasonable to conclude that the contact point,  $C_i$ , moved to the stylus flank. In this case, point  $C'_i$ , which was calculated by a stylus radius correction algorithm, would deviate from the real sample surface, as shown in Figure 4(b). As  $C'_i$  is used in

the measurement to represent the sample surface, profile distortion would be generated.

In this case, the X motorized driven stage with the sample would be tilted by the spindle at a preset step angle  $\beta$ .  $\beta$  is set to be positive along the anticlockwise direction and negative along the clockwise direction. The previous scanning results, therefore, follow the rotation, and their updated coordinates can be recalculated by

$$\begin{bmatrix} P'_1 \\ P'_2 \\ P'_3 \\ \vdots \\ P'_i \end{bmatrix} = \begin{bmatrix} P'_{1-X} & P'_{1-Z} \\ P'_{2-X} & P'_{2-Z} \\ P'_{3-X} & P'_{3-Z} \\ \vdots & \vdots \\ P'_{i-X} & P'_{i-Z} \end{bmatrix} \times \begin{bmatrix} \cos \beta & \sin \beta \\ -\sin \beta & \cos \beta \end{bmatrix}. \quad (2)$$

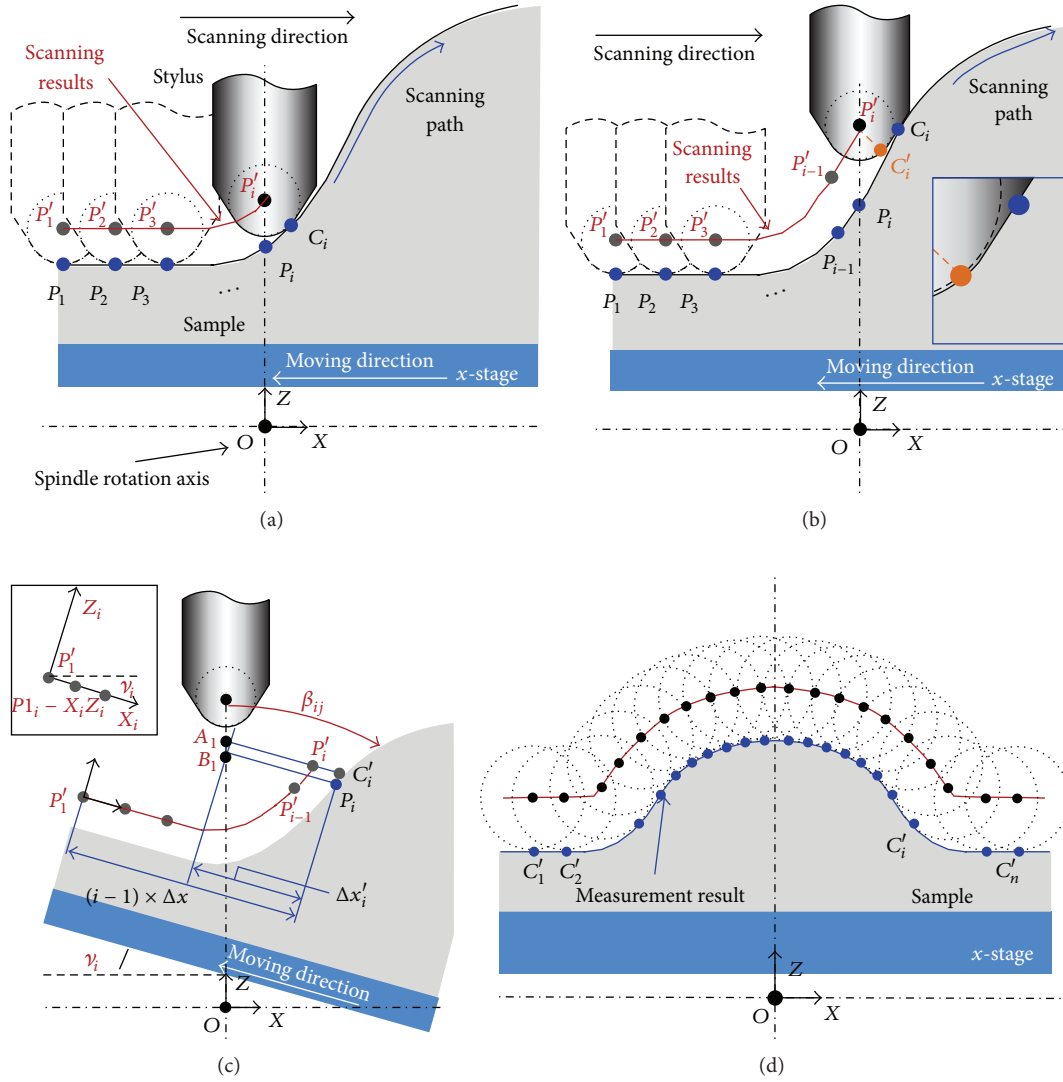


FIGURE 4: Control methods of the sample-tilting and the X motorized stage. (a) Schematic of stylus scanning. (b) Principle of profile deviation. (c) Schematic of sample-tilting. (d) Schematic of profile reconstruction.

After the rotation, the current measuring point,  $P_i$ , is not located at the ideal position where the  $x$ -coordinate is zero, which was shown in Figure 4(c). Because the exact spatial coordinates of  $P_i$  are unknown,  $P_i$  cannot be easily corrected to the ideal position by the  $X$  stage moving a given distance. The last three points  $[P'_{i-2} P'_{i-1} P'_i]$  of the scanning results after the coordinate transformation are used to estimate the current spatial coordinates of  $P_i$ . The slope of the curve, which is obtained by the first-order linear fitting of the points  $[P'_{i-2} P'_{i-1} P'_i]$ , is denoted by  $\rho'_i$ . The current coordinates  $[P_{i-X} P_{i-Z}]$  of  $P_i$  are expressed as

$$[P_{i-X} P_{i-Z}] = [P'_{i-X} + r \cdot \cos \rho'_i \quad P'_{i-Z} - r \cdot |\sin \rho'_i|]. \quad (3)$$

The total rotation angle of the spindle until this point is denoted by  $\nu_i$ , which is the cumulative sum of  $\beta$ . The

displacement of the  $X$  motorized driven stage is denoted by  $\Delta x'_i$  and derived from

$$\Delta x'_i = \frac{P_{i-X}}{\cos \nu_i}. \quad (4)$$

After the position of  $P_i$  along the  $X$ -direction is corrected,  $P_i$  can be measured and the local slope  $\rho_i$  is detected again. The sample-tilting process is repeated until the local slope  $\rho_i$  is smaller than  $\theta$ . If  $\rho_i$  meets the requirement relative to  $\theta$ , the surface scanning turns to  $P_{i+1}$ , and the moving distance of the  $X$  motorized stage is expressed as

$$\Delta x_{i+1} = \frac{\Delta x}{\cos \nu_i}. \quad (5)$$

It should be noted that the cumulative rotation angle of the sample-tilting is limited by the maximum rotation angle

of the spindle, denoted by  $\varphi$ , which is manually set according to the motion error of the spindle.

After the surface scanning is finished, the orientation of the scanning results can be transformed to its initial state by

$$\begin{bmatrix} P'_1 \\ P'_2 \\ P'_3 \\ \vdots \\ P'_N \end{bmatrix} = \begin{bmatrix} P'_{1-X} & P'_{1-Z} \\ P'_{2-X} & P'_{2-Z} \\ P'_{3-X} & P'_{3-Z} \\ \vdots & \vdots \\ P'_{N-X} & P'_{N-Z} \end{bmatrix} \times \begin{bmatrix} \cos(-\nu_N) & \sin(-\nu_N) \\ -\sin(-\nu_N) & \cos(-\nu_N) \end{bmatrix}, \quad (6)$$

where  $\nu_N$  is the total rotation angle after the last point  $P_N$  is measured and  $N$  is the number of sampling points.

As shown in Figure 4(d), the scanning result is an envelope of the sample surface. A stylus tip radius correction algorithm based on a first-order linear fitting method was used to eliminate the error introduced by the flank of the stylus tip. Assume that  $\rho''_i$ , which is obtained by the first-order linear fitting method, is the slope of each point  $P'_i$ . The contact point  $C'_i$ , the measurement results to represent the sample surface, can be obtained from

$$\begin{bmatrix} C'_1 \\ C'_2 \\ C'_3 \\ \vdots \\ C'_N \end{bmatrix} = \begin{bmatrix} C'_{1-X} & C'_{1-Z} \\ C'_{2-X} & C'_{2-Z} \\ C'_{3-X} & C'_{3-Z} \\ \vdots & \vdots \\ C'_{N-X} & C'_{N-Z} \end{bmatrix} = \begin{bmatrix} P'_{1-X} + r \cdot (k) \cdot \cos \rho''_1 & P'_{1-Z} - r \cdot |\sin \rho''_1| \\ P'_{2-X} + r \cdot (k) \cdot \cos \rho''_2 & P'_{2-Z} - r \cdot |\sin \rho''_2| \\ P'_{3-X} + r \cdot (k) \cdot \cos \rho''_3 & P'_{3-Z} - r \cdot |\sin \rho''_3| \\ \vdots & \vdots \\ P'_{N-X} + r \cdot (k) \cdot \cos \rho''_N & P'_{N-Z} - r \cdot |\sin \rho''_N| \end{bmatrix}. \quad (7)$$

In (7), the range of  $\rho''_i$  is from  $-\pi/2$  to  $+\pi/2$ , and if  $\rho''_i$  is equal to or greater than zero, the coefficient  $k$  is 1; otherwise, it is  $-1$ .

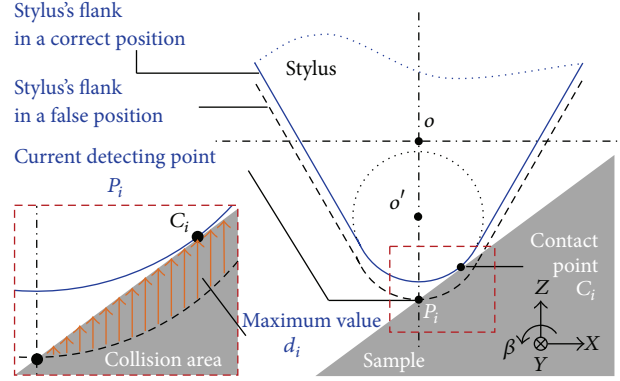


FIGURE 5: Schematic of detecting the contact point.

### 3. Simulation Method of the Surface Profile Measurement

To verify the feasibility of the proposed method, MATLAB was used to carry out the surface profile measurement of microstructures with steep surfaces. The surfaces of the employed stylus and the microstructure under test are dispersed to be point clouds with equal intervals in the  $X$ -direction. The motion of the stylus is simulated by modifying its  $z$ -coordinates. Therefore, the variation of the  $z$ -coordinates is the output of the displacement sensor. Similarly, the motion of the  $X$  motorized driven stage is carried out by changing the  $x$ -coordinates of the microstructure. The sample-tilting and data processing are carried by the method described in the previous section. In a traditional profiling method, the motions of the stylus and the  $X$  motorized driven stage are used to construct the surface profile of the sample. The proposed method employs a spindle to adjust the sample-stylus relative angle. Therefore, the remaining issue is how to simulate the physical contact between the stylus tip and the sample surface.

Figure 5 illuminates the method to detect the contact point between the stylus flank and the sample surface. When measuring a steep surface, the stylus moves depending on the variation of the surface profile of the sample under test. The contact position is not located at the current detecting point  $P_i$  but at a point nearby. In the simulation, the stylus tip is first moved a distance, which is denoted by  $w_i$ , to  $P_i$ . The collision area is then detected by comparing the  $z$ -coordinates of the stylus and the sample. The point where the difference in the  $z$ -coordinates has a maximum value is the correct contact point  $C_i$ , and the maximum difference is denoted by  $d_i$ . Next, the stylus draws back by a distance  $d_i$ , and the correct contact point  $C_i$  can be determined. The stylus position denoted by  $z_i$  is stored as the output of the displacement sensor and is expressed as

$$z_i = w_i - d_i. \quad (8)$$

### 4. Measurement Simulation and Analysis

Two types of microstructures with steep surfaces were employed to verify the feasibility of the slope-adapted

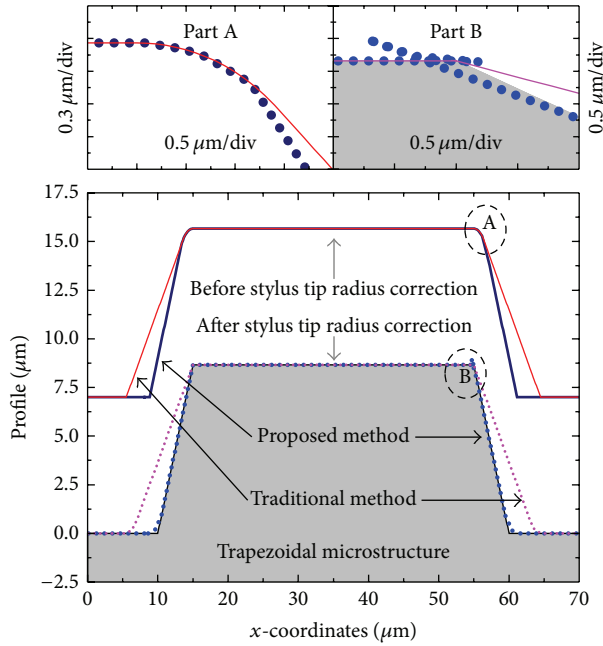


FIGURE 6: Results of profiling a trapezoidal microstructure.

sample-tilting method. The samples were measured twice, using the proposed method and the traditional scanning method, in which the relative direction of the sensing axis of the probing system to the measurement sample surface is unchangeable and the maximum detectable angle is limited by the included angle of the employed stylus [13], to demonstrate the improved measurement capability on steep surfaces.

A trapezoidal microstructure with a maximum local slope of up to 60 degrees was measured first. The height of the microstructure is  $8.66 \mu\text{m}$ , and its whole width is  $70 \mu\text{m}$ . A diamond-tipped stylus, which is employed in the hardware realization, was introduced into the simulation. The tip radius of the stylus is two micrometers with an included angle of 90 degrees, which means that the maximum detectable angle is 45 degrees. The interval of the surface discretization was set to  $0.01 \mu\text{m}$ , and the scanning interval was set to  $0.1 \mu\text{m}$ . The maximum sample-stylus relative angle was set to 30 degrees, which is  $2/3$  of the maximum detectable angle, 45 degrees. No maximum rotation angle of the spindle was set, to research the motion feature of the rotating spindle. In addition, the step-angle of the sample-tilting was set to be one degree.

Figure 6 shows the measurement results of the trapezoidal microstructure. Profiles before and after the stylus tip radius correction are plotted. As shown in the figure, the measurement result of the proposed method is much more accurate than that of the traditional method because it is much closer to the real surface of the sample. In contrast, the result of the traditional method shows obvious profile deviation and a blind region on the sample side flanks, where the local slope is up to 60 degrees. The measurement of the proposed method on part “B” exhibits data confusion, which, upon comparing the data on parts “A” and “B,” was

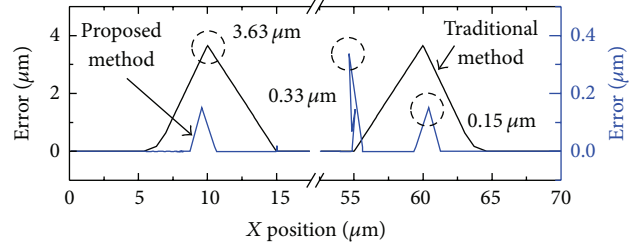


FIGURE 7: Errors in profiling a trapezoidal microstructure.

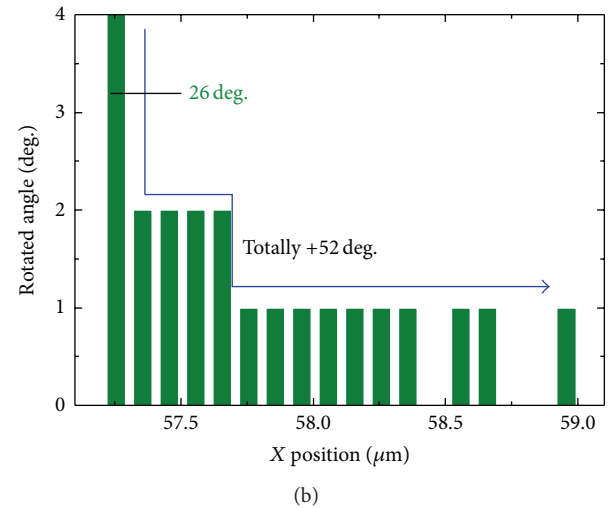
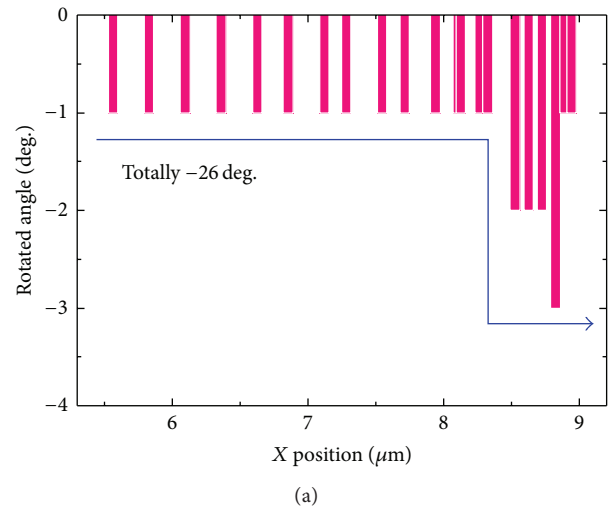


FIGURE 8: Sample-tilting process of profiling a trapezoidal microstructure.

determined to result from the stylus tip radius correction algorithm.

The measurement errors shown in Figure 7 were calculated by comparing the  $y$ -coordinates with the real profile of the sample. As shown in the figure, the measurement error of the traditional method was up to  $3.63 \mu\text{m}$ , while that of the proposed method was reduced to  $0.15 \mu\text{m}$ . It should be noted that the peak value of  $0.33 \mu\text{m}$  in the error curve of the proposed method resulted from the data treatment of the stylus radius correction. Figure 8 shows the sample-tilting

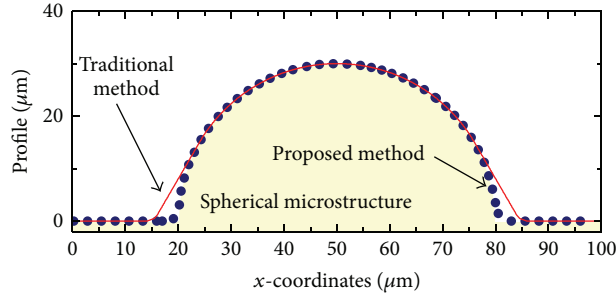


FIGURE 9: Results of profiling a spherical microstructure.

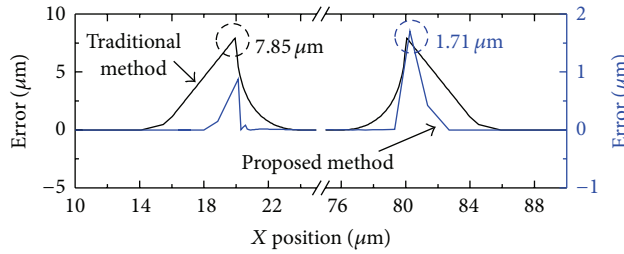


FIGURE 10: Errors in profiling a spherical microstructure.

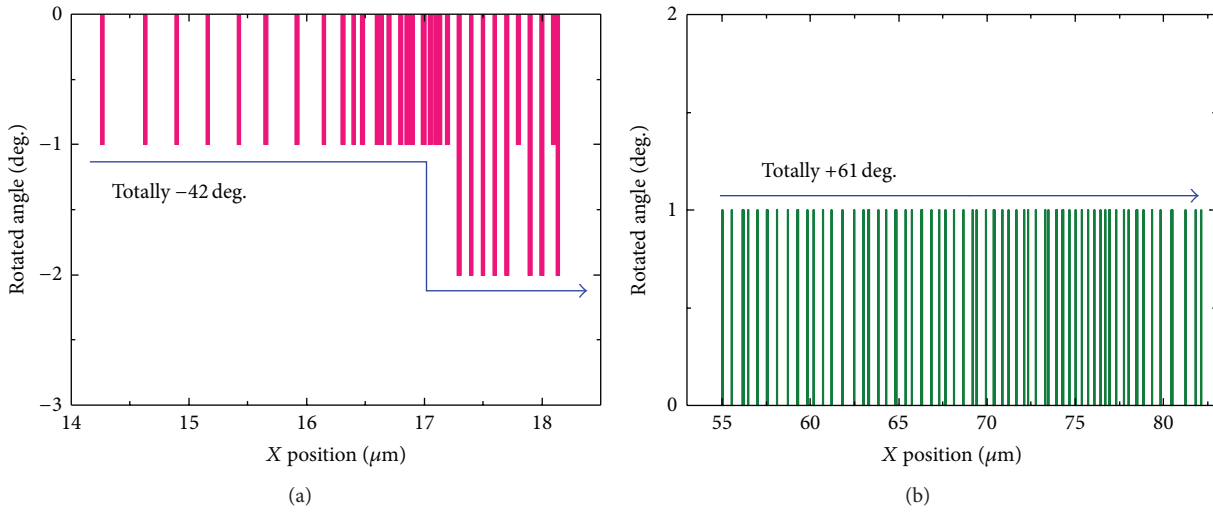


FIGURE 11: Sample-tilting process of profiling a spherical microstructure.

process. The sample was tilted by a total of 26 degrees in a clockwise direction when measuring the left part of the sample, over the  $x$ -coordinates range of  $5 \mu\text{m}$  to  $9 \mu\text{m}$ . When measuring the right part, the sample was tilted by a total of 52 degrees in an anticlockwise direction. It should be mentioned that when measuring a position at an  $x$ -coordinate of  $57.25 \mu\text{m}$ , the sample is rotated by 26 degrees at once.

A spherical microstructure with a radius of  $30 \mu\text{m}$  was employed as the secondary sample. In the measurement, the included angle of the stylus was set to 60 degrees, and the maximum sample-stylus relative angle was set to 45 degrees, which is  $3/4$  of the maximum detectable angle, 60 degrees. The step-angle of the sample-tilting was set to two degrees.

The other parameters were the same as those used in profiling the trapezoid microstructure.

Figure 9 displays the measurement results of the spherical microstructure. As shown in the figure, the profiles overlapped with each other over most parts of the sample surface, except for the regions around the two concave corners. This result indicates that the proposed method is able to measure a steep surface even with a local slope of up to 90 degrees. Figure 10 compares the measurement errors of the two methods, which were linked to the left and right  $y$ -axes, respectively. The maximum error of the traditional method is  $7.85 \mu\text{m}$  and that of the proposed method is reduced to  $1.71 \mu\text{m}$ . Figure 11 shows the sample-tilting process. The sample was tilted by a total of 42 degrees in the clockwise

direction when measuring the left part and by a total of 61 degrees in the anticlockwise direction for the right part.

## 5. Conclusion

A slope-adapted sample-tilting method has been proposed for the profile measurement of microstructures with steep surfaces. Theoretical work required to realize a system to implement the proposed method has been completed. Profile measurements of trapezoidal and spherical microstructures have been simulated to verify the performance of the developed method. The measurement results reveal that the steep surface of a microstructure can be precisely measured by the developed method.

The future work of this research will focus on analyzing the influence of the spindle motion error and realizing the stylus-based profiling system.

## Conflict of Interests

The authors declare that there is no conflict of interests regarding the publication of this paper.

## Acknowledgments

This work is supported by the National Natural Science Foundation of China (Grant no. 51405314) and by the Fundamental Research Funds for the Central Universities (Grant no. 2015SCU04A12).

## References

- [1] A. Weckenmann, G. Peggs, and J. Hoffmann, "Probing systems for dimensional micro- and nano-metrology," *Measurement Science and Technology*, vol. 17, no. 3, pp. 504–509, 2006.
- [2] P. M. Lonardo, D. A. Lucca, and L. De Chiffre, "Emerging trends in surface metrology," *CIRP Annals—Manufacturing Technology*, vol. 51, no. 2, pp. 701–723, 2002.
- [3] M. B. Bauza, S. C. Woody, B. A. Woody, and S. T. Smith, "Surface profilometry of high aspect ratio features," *Wear*, vol. 271, no. 3–4, pp. 519–522, 2011.
- [4] H. N. Hansen, K. Carneiro, H. Haitjema, and L. de Chiffre, "Dimensional micro and nano metrology," *CIRP Annals—Manufacturing Technology*, vol. 55, no. 2, pp. 721–743, 2006.
- [5] B. Xu, Y. Shimizu, S. Ito, and W. Gao, "A micro-ball tapping probe for form measurement of micro-structured surface," *Journal of the Chinese Society of Mechanical Engineers*, vol. 34, no. 1, pp. 73–80, 2013.
- [6] B. Xu, Z. Jia, X. Li et al., "Surface form metrology of micro-optics," in *International Conference on Optics in Precision Engineering and Nanotechnology (icOPEN2013)*, vol. 8769 of *Proceedings of SPIE*, April 2013.
- [7] B. Xu, Y. Shimizu, T. Takeishi, S. Ito, and W. Gao, "Surface form measurement and analysis of a cylindrical workpiece with microstructures," *Journal of Advanced Mechanical Design, Systems and Manufacturing*, vol. 6, no. 6, pp. 936–948, 2012.
- [8] F. Z. Fang, X. D. Zhang, A. Weckenmann, G. X. Zhang, and C. Evans, "Manufacturing and measurement of freeform optics," *CIRP Annals—Manufacturing Technology*, vol. 62, no. 2, pp. 823–846, 2013.
- [9] K.-W. Lee, Y.-J. Noh, W. Gao et al., "Experimental investigation of an air-bearing displacement sensor for on-machine surface form measurement of micro-structures," *International Journal of Precision Engineering and Manufacturing*, vol. 12, no. 4, pp. 671–678, 2011.
- [10] K. Takamasu, "Present problems in coordinate metrology for nano and micro scale measurements," *MAPAN*, vol. 26, no. 1, pp. 3–14, 2011.
- [11] Y. Takaya, M. Michihata, T. Hayashi, and T. Washitani, "Dimensional measurement of microform with high aspect ratio using an optically controlled particle with standing wave scale sensing," *CIRP Annals—Manufacturing Technology*, vol. 61, no. 1, pp. 479–482, 2012.
- [12] B.-F. Ju, Y.-L. Chen, W. Zhang, W. Zhu, C. Jin, and F. Z. Fang, "Note: long range and accurate measurement of deep trench microstructures by a specialized scanning tunneling microscope," *Review of Scientific Instruments*, vol. 83, no. 5, Article ID 056106, 2012.
- [13] B.-F. Ju, Y.-L. Chen, W. Zhang, and F. Z. Fang, "Rapid measurement of a high step microstructure with 90 degrees steep sidewall," *Review of Scientific Instruments*, vol. 83, no. 1, Article ID 013706, 2012.
- [14] F. Marinello, P. Bariani, A. Pasquini, L. De Chiffre, M. Bossard, and G. B. Picotto, "Increase of maximum detectable slope with optical profilers, through controlled tilting and image processing," *Measurement Science and Technology*, vol. 18, no. 2, pp. 384–389, 2007.
- [15] S.-J. Cho, B.-W. Ahn, J. Kim et al., "Three-dimensional imaging of undercut and sidewall structures by atomic force microscopy," *Review of Scientific Instruments*, vol. 82, no. 2, Article ID 023707, 2011.
- [16] S. P. Pan, H. C. Liou, C. C. A. Chen, J.-R. Chen, and T.-S. Liu, "Precision measurement of sub-50 nm linewidth by stitching double-tilt images," *Japanese Journal of Applied Physics*, vol. 49, no. 6, Article ID 06GK06, 2010.
- [17] R. Henselmans, L. A. Cacace, G. F. Y. Kramer, P. C. J. N. Rosielle, and M. Steinbuch, "The NANOMEFOS non-contact measurement machine for freeform optics," *Precision Engineering*, vol. 35, no. 4, pp. 607–624, 2011.
- [18] A. Schuler and A. Weckenmann, "Application of sensor tilting for enhanced measurement of microstructures," *Proceedings of the Institution of Mechanical Engineers, Part B: Journal of Engineering Manufacture*, vol. 227, no. 1, pp. 12–20, 2013.
- [19] A. Weckenmann, A. Schuler, and R. J. B. Ngassam, "Enhanced measurement of steep surfaces by slope-adapted sensor tilting," *Measurement Science and Technology*, vol. 23, no. 7, Article ID 074007, 2012.
- [20] J. W. Cui, L. Li, J. Y. Li, and J. B. Tan, "Fiber probe for micro-hole measurement based on detection of returning light energy," *Sensors and Actuators A: Physical*, vol. 190, pp. 13–18, 2013.
- [21] S. Z. Wang, T. B. Xie, and S. P. Chang, "A white light interference-based atomic force probe scanning microscopy," *Measurement Science and Technology*, vol. 22, no. 4, Article ID 045502, 2011.
- [22] J. A. Kramar, R. Dixon, and N. G. Orji, "Scanning probe microscope dimensional metrology at NIST," *Measurement Science and Technology*, vol. 22, no. 2, Article ID 024001, 2011.
- [23] W. Gao, B. Xu, T. Takeishi, Y. Shimizu, and S. Ito, "Self-calibration and compensation of setting errors for surface

profile measurement of a microstructured roll workpiece,” *Chinese Journal of Mechanical Engineering*, vol. 27, no. 1, pp. 14–22, 2014.

- [24] B. Xu, Y. Shimizu, S. Ito, and W. Gao, “Surface profile measurement of internal micro-structures,” *International Journal of Precision Engineering and Manufacturing*, vol. 14, no. 9, pp. 1535–1541, 2013.

## Research Article

# Frontal Cryosectioning: An Improved Protocol for Sectioning Large Areas of Fibrous Scaffolds

Casey P. Grey<sup>1</sup> and David G. Simpson<sup>2</sup>

<sup>1</sup>Department of Biomedical Engineering, Virginia Commonwealth University, Richmond, VA 23284, USA

<sup>2</sup>Department of Anatomy and Neurobiology, Virginia Commonwealth University, Richmond, VA 23298, USA

Correspondence should be addressed to Casey P. Grey; [greycp@vcu.edu](mailto:greycp@vcu.edu)

Received 30 January 2015; Accepted 22 April 2015

Academic Editor: Bei Peng

Copyright © 2015 C. P. Grey and D. G. Simpson. This is an open access article distributed under the Creative Commons Attribution License, which permits unrestricted use, distribution, and reproduction in any medium, provided the original work is properly cited.

Fibrous tissue engineering scaffolds, such as those produced by electrospinning, cannot achieve their clinical potential until deep cell-scaffold interactions are understood. Even the most advanced imaging techniques are limited to capturing data at depths of 100  $\mu\text{m}$  due to light scatter associated with the fibers that compose these scaffolds. Conventional cross-sectional analysis provides information on relatively small volumes of space and frontal sections are difficult to generate. Current understanding of cellular penetration into fibrous scaffolds is limited predominantly to the scaffold surface. Although some information is available from cross-sections, sections vary in quality, can distort spatial scaffold properties, and offer virtually no spatial cues as to what scaffold properties instigate specific cellular responses. Without the definitive ability to understand how cells interact with the architecture of an entire scaffold it is difficult to justify scaffold modifications or in-depth cell penetration analyses until appropriate techniques are developed. To address this limitation we have developed a cryosectioning protocol that makes it possible to obtain serial frontal sections from electrospun scaffolds. Microscopic images assembled into montage images from serial sections were then used to create three-dimensional (3D) models of cellular infiltration throughout the entire scaffold.

## 1. Introduction

Electrospinning is a technique that can be used to produce three-dimensional (3D) tissue engineering scaffolds composed of nano- to micron-sized fibers fabricated from natural proteins [1, 2], synthetic polymers [3–6], and blends of natural proteins and synthetic polymers [7–9]. The versatility of this technique allows for considerable control over the composition, mechanical (e.g., tensile strength, elasticity, etc.), and structural (e.g., fiber size, fiber alignment, scaffold shape, scaffold porosity, etc.) properties of the resulting constructs [4, 10–12]. Electrospinning produces a unique class of nanomaterials that can be utilized in a wide variety of biological applications; for example, electrospun scaffolds have been used to investigate how cells interact with 3D environments of varying compositions [13, 14], and, in a more esoteric application, electrospinning has been proposed as a method for fabricating organs and tissues targeted for replacement therapy [15–17]. Understanding, promoting,

and regulating the extent of cellular penetration and population of electrospun scaffolds is fundamental to each of these potential applications and considerable effort has been directed at achieving this objective [4, 8, 18].

The refractive nature of the fibers that comprise an electrospun scaffold limits the utility of conventional light and confocal microscopy in the analysis of electrospun scaffolds [19, 20]. Even with two-photon microscopy, the structural properties of these constructs limit imaging to a maximum depth of approximately 100  $\mu\text{m}$ , and even then the resulting  $z$ -stack data represents a small fraction of the entire surface area of the scaffold [20, 21]. Several laboratories, including our own, have used cross-sectional analysis of samples taken from frozen sections in order to judge the extent of cellular penetration into electrospun scaffolds [12, 22, 23]. However, given the complex surfaces and wide distribution of cells in electrospun materials it is difficult to characterize the depth and extent of cell penetration throughout an entire scaffold using these methods. Data collection in this type of analysis

is usually limited to a few selected sections taken from the scaffold and, without a comprehensive morphometric approach, this type of analysis often results in a subjective and biased analysis of the samples.

Tissue engineering scaffolds targeted for use in reconstructive therapy are typically designed to mimic the gross dimensional characteristics of the native target tissue [4, 10, 24, 25]. For example, the wall of a native, small diameter artery may reach nearly 500  $\mu\text{m}$  in thickness in an adult, ostensibly requiring a scaffold of approximately the same thickness to act as a graft [26, 27]. In this example, due to the inherent limitations imposed by the structure of the scaffold, the spatial cell-matrix information for the majority of the scaffold would be unobtainable. Developing methods to better understand how cells interact throughout the entirety of a tissue engineering scaffold represents an important element of the design process. Without this type of information it is difficult to make rational decisions concerning what changes in structure, nutrient support, and/or seeding conditions might be necessary to modulate cell distribution and function. Scaffold structural considerations are too often based on limited data (e.g., cross-sectional samples) at best and, at worst, academic guesswork. In this study we describe a method in which we are able to take serial frontal sections through the entire thickness of frozen electrospun scaffolds. This represents a method that provides nearly unambiguous information concerning the depth and spatial distribution of cells within a given scaffold design. By reconstructing data collected from the individual serial sections into a three-dimensional model it is also possible to explore how regional variations in scaffold structure impact cell-matrix interactions.

## 2. Materials and Methods

**2.1. Electrospinning.** All reagents were obtained from Sigma unless otherwise noted. Polycaprolactone (PCL: 65,000 M.W.) was suspended and electrospun from trifluoroethanol (TFE) at concentrations of 150 mg/mL (producing small diameter fibers) or 250 mg/mL (producing large diameter fibers). Electrospinning syringes were capped with a blunt-tipped 18-gauge needle and placed into a syringe driver (Fisher Scientific) set to deliver the electrospinning fluid into an 18–21 kV static electric field at a rate of 8 mL/hr across a 20 cm gap [4]. A solid cylindrical metal mandrel (length = 11.75 cm, diameter = 6.33 mm) or a perforated cylindrical metal mandrel was used as ground targets (functional length = 11.75 cm, mandrel diameter = 6.33 mm, and pore diameter = 0.75 mm spaced laterally 2 mm and vertically 1.5 mm) [4, 12]. The target mandrels were designed to rotate and translate laterally (4 cm/s over a 12 cm distance) in order to facilitate an even distribution of fibers.

**2.2. Cell Culture.** Human dermal fibroblasts (hDF, Cascade Biologics C-013-5C) were cultured in DMEM-F12 (Gibco) supplemented with 10% fetal bovine serum (FBS, Hyclone) and 1% penicillin/streptomycin (P/S, Invitrogen). For cell culture experiments 6 mm diameter and 1 mm thick circular samples were punch cut from electrospun scaffolds and sanitized in a 70% ethanol wash for 30 min followed by two

phosphate buffer solution (PBS) rinses and one media rinse. Scaffolds were seeded with 25,000 cells and cultured in an incubator set to 37°C and 5% CO<sub>2</sub>. Cell culture media were changed every 3 days. For analysis, populated scaffolds were fixed in 10% glutaraldehyde in phosphate buffer solution (PBS) for 10 minutes followed by two rinses in PBS. Samples were placed in fresh PBS and stored at 4°C until being processed for analysis. Samples were cut into 50  $\mu\text{m}$  thick serial sections as described subsequently in this study and stained with 4',6-diamidino-2-phenylindole (DAPI) and rhodamine phalloidin.

**2.3. Image Acquisition.** Montage images of each serial section were prepared from data captured with a Nikon TE300 microscope equipped with 10x and 20x objectives and a DXM 1200 digital camera, all images captured at a resolution of 1280 × 1024. Brightfield images were overlaid with fluorescence images using the Photomerge function of Adobe Photoshop CS4. 3D scaffold reconstruction was performed using Google SketchUp Make.

### 2.4. Cryosectioning Sample Preparation and Cutting Protocol

- (1) Samples were placed into a 30% sucrose solution prepared in PBS for 3 days at 4°C. This extended incubation period was used to ensure that the scaffolds were fully infiltrated with sucrose and cryoprotected during processing. Poor sucrose infiltration (e.g., short soak times) resulted in inconsistent cell preservation and catastrophic sample deformation during cutting (e.g., crush and fragmentation issues that prevented section recovery). This is one of the most critical steps in this protocol; typical procedures call for 1 hour submersion in sucrose which resulted in very poor frontal sectioning [28].
- (2) Samples were removed from the sucrose solution and placed directly into a “cryomold” containing sufficient optimal cutting temperature compound (OCT) embedding media to fully submerge the scaffolds. We have found that Fisher, flat-bottom culture dishes work as well as cryomolds. Extended scaffold exposure to unfrozen OCT was avoided as it was found to reduce rhodamine staining of actin.
- (3) A nonseeded (scrap) scaffold of identical size to the sample to be processed was placed directly on top of the cell seeded sample. This second scaffold was used as a “buffer” to reduce the risk of physically damaging the underlying scaffold of interest.
- (4) The entire cryomold was then placed onto the cryobar inside the cryostat (Figure 1) and, using a press tool, the sample was quickly submerged and flattened by pressing it down to the bottom of the cryomold until all OCT had solidified. In this step the scrap scaffold mitigates physical damage to the scaffold from the press tool and provides a backing for when the press tool is removed (see Figure 2). The press tool is ideally a semirigid, flat-bottom cylinder of similar size to the sample. We used a 5 mm diameter, 2.5 cm long cylindrical eraser refill for this study (Helix, Grandville, MI).

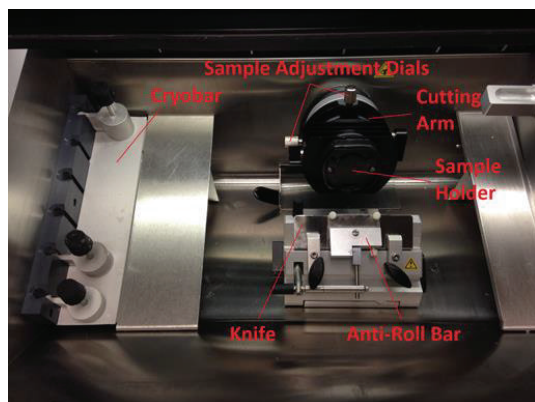


FIGURE 1: Typical cryosectioning chamber. Temperatures used were as follows: cryobar ( $-35^{\circ}\text{C}$ ), chamber ( $-25^{\circ}\text{C}$ ), and specimen ( $-34^{\circ}\text{C}$  to  $-36^{\circ}\text{C}$ ).

- (5) Once the OCT in the cryomold had solidified, the press tool was removed with a gentle twisting motion, keeping the sample on the cryobar at all times.
- (6) Frozen samples were allowed to fully solidify on the cryobar (3–5 min). At this point all tools needed for sample manipulation (forceps, brushes, knife, etc.) were placed into the cryochamber and allowed to cool to sectioning temperature. Room temperature tools will melt the OCT which can make handling the sample extremely difficult. Additionally any melted OCT that refreezes onto the knife increases cutting difficulty (the knife needs to be as clean as possible at all times).
- (7) Frozen scaffolds were recovered from the cryomold and affixed to a textured cryosectioning plate using OCT as an adhesive.
- (8) Once the sample was mounted onto the cryosectioning plate, the plate was secured to the sectioning arm of the cryostat and allowed to cool to sectioning temperature (3–5 minutes).
- (9) Aligning the sample with the knife edge is crucial. We accomplished this by bringing the sample as close to the knife as possible (without touching) and aligning it as flush as possible to the blade. If the sample is not aligned properly the ensuing cut will yield only a portion of the section. If this happens, realign the sample based on the previous cut and resection. We stored cut sections in 48-well tissue culture plates filled with PBS. Retain any sections that may have been taken misaligned as these and the realigned samples still represent the surface of the scaffold. Useful data can still be extracted from these samples. It takes practice and patience to properly align a scaffold.
- (10) For PCL scaffolds, a general sectioning speed of one rotation of the cutting cycle per second was used to process the frozen material. The rate of travel across the knife blade that produces the best sections can be expected to vary to some degree by the nature of the sample processed and is usually determined through experience.

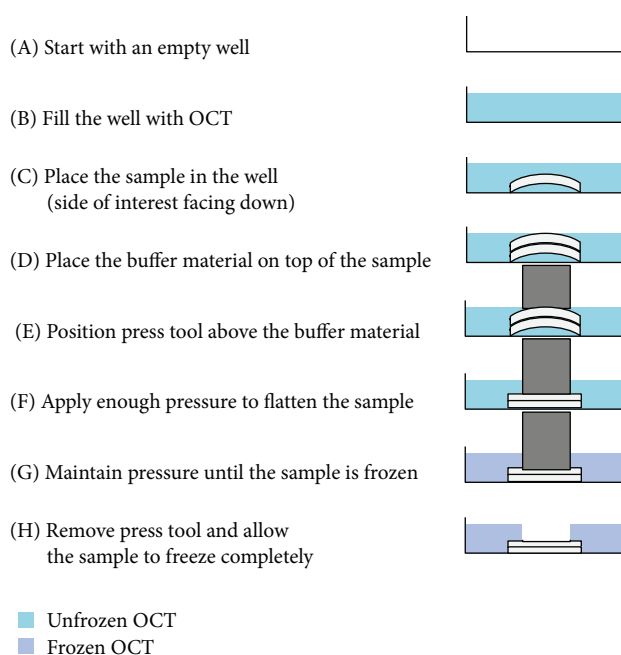


FIGURE 2: Flattening and freezing a sample for cryosectioning. The flattening process is critically important—ensuring the sample is flush with the bottom of the flat bottomed cryomold allows for accurate alignment of the first, crucial section. Steps (A)–(D) are completed outside of the cryosectioning chamber (room temperature) while steps (E)–(H) are completed inside the cryosectioning chamber, on the cryobar or on an equivalent precooled metal mass. Steps (E) and (F) must be completed quickly after placing the sample in the cryosectioning chamber to prevent the premature freezing of the sample in an unflattened state (e.g., if a sample has residual tension, such as when electrospinning onto a small diameter mandrel, it will tend to curl).

- (11) Once cut, each section was recovered from the knife surface with cold, fine-tipped forceps by grasping the frozen OCT that surrounds the cut section (rather than grasping the section itself) so as not to damage it. Each section was then placed in separate PBS-filled wells (24-, 36-, and 48-well plates work well for this process), rather than onto dry microscope slides. This serves a dual purpose; first, placing sections directly into PBS quickly dissolves any residual OCT and ensures that the sections stay hydrated; the hydration step improves overall image quality. Second, dissolving the residual OCT mitigates the concerns regarding reduced rhodamine staining mentioned above. Third, the PBS bath is very forgiving and helps to flatten or unfurl sections that may have folded during recovery. Manually flattening a section after placement onto a dry microscope slide is extremely difficult as the delicate sections tend to tear rather than unfold. Additionally, rehydration of cut sections allowed to dry on a microscope slide commonly results in air bubbles being trapped inside the fibrous network, reducing image quality.

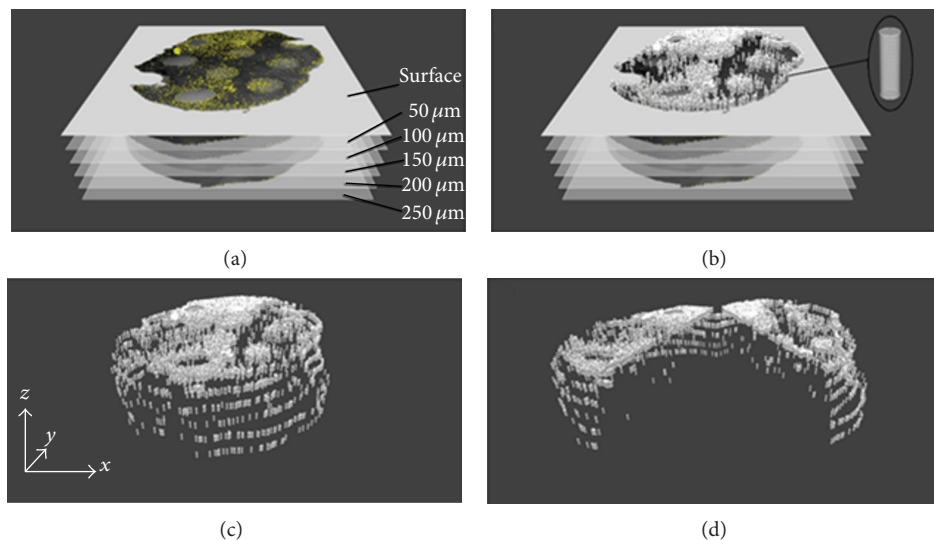


FIGURE 3: Construction of a three-dimensional model of cellular infiltration. (a) Images are imported into the workspace and separated on the  $z$ -axis by a factor of 10. (b) A three-dimensional object of choice is used to replace each of the DAPI positive nuclei to represent cell location in space. (c) The bright field channel images depicting the scaffold fibers are turned off. (d) To better visualize cell penetration within the scaffolds a digital section was prepared and the opposing images were rotated to reveal the distribution of cells within the scaffold.

- (12) Sections were either stored in PBS at  $4^{\circ}\text{C}$  (assuming slow scaffold degradation rates) or processed immediately. Regardless of treatment, all cut sections were washed with fresh PBS to remove residual OCT (which can reduce rhodamine staining as mentioned above). To image sections, a drop of PBS was placed onto a microscope slide or coverslip into which (using fine-tipped forceps) sections were transferred. Some less-stiff sections will fold in on themselves once they are moved from the wells but generally unfold once resubmerged in the PBS droplet, manual manipulation was rarely required with the PCL scaffolds. A coverslip was placed over the section and any excess PBS was removed so that the sections were flattened. The sections were then imaged and either placed back into its original well for storage or the coverslip was sealed and the section stored on the slide. Of note, placing the sections between two microscope coverslips (eliminating the thicker microscope slide) for imaging simplifies flipping the sections over to investigate either side of the scaffold in detail.

**2.5. Image Analysis.** Our objective is to develop methods to characterize the distribution of cells within an electrospun scaffold on a global scale. To achieve this objective we systematically captured overlapping images across the entire surface of each individual  $50\ \mu\text{m}$  thick cryosection. Prior to moving the image field of view images were first captured in the brightfield channel and then in the fluorescence channel; this insures registry between the two image data sets. Paired bright field and fluorescence images were combined to produce a composite image. Using the Photomerge function in Photoshop the individual composite images were then assembled into a montage that represented the entire surface area of each individual serial frontal section. The brightfield

channel was used in this assembly process because images collected from the fluorescence channel (especially if DAPI images are required) lack sufficient data density to for the Photomerge function to assemble the montage (i.e., an image of widely distributed nuclei does not have enough image terrain features to allow the algorithm to assemble the individual microscopic image fields into a montage).

Montage images from each individual frontal section were imported into Google SketchUp and placed in a  $z$ -stack orientation within the workspace (Figure 3). To facilitate modeling we increased the distance between each frontal section by a factor of ten to better visualize scaffold layer properties. Montage composite images were aligned in the vertical orientation using scaffold features or fiduciary marks placed within the scaffolds prior to embedding. This process was greatly simplified in this study because the exemplar scaffold was fabricated using air impedance electrospinning, a process that produces large scale features that penetrate the scaffold in the  $z$ -direction. Registry marks can be incorporated into the peripheral edges of conventional scaffolds using a small diameter needle to facilitate the alignment process.

To model cell position a 3D shaded rendering of a cylinder approximating the cross-sectional dimensions of a cell was created and used to replace the DAPI nuclear images marking the position of each cell within the scaffold (Figure 3(b)). We note here that the 3D shape used for cellular representation in this model is arbitrary. In some cases it may be helpful to use different shapes, such as spheres, to improve cell visualization; however, it should be noted that this is only a representation of the location of the cell, not a depiction of actual cell shape.

Once all of the cells have been represented by a shaded cylinder (or other 3D object) in the montage  $z$ -stacks, the brightfield image channel was turned off (Figure 3(c)) allowing just the 3D distribution of the cylinders that mark each

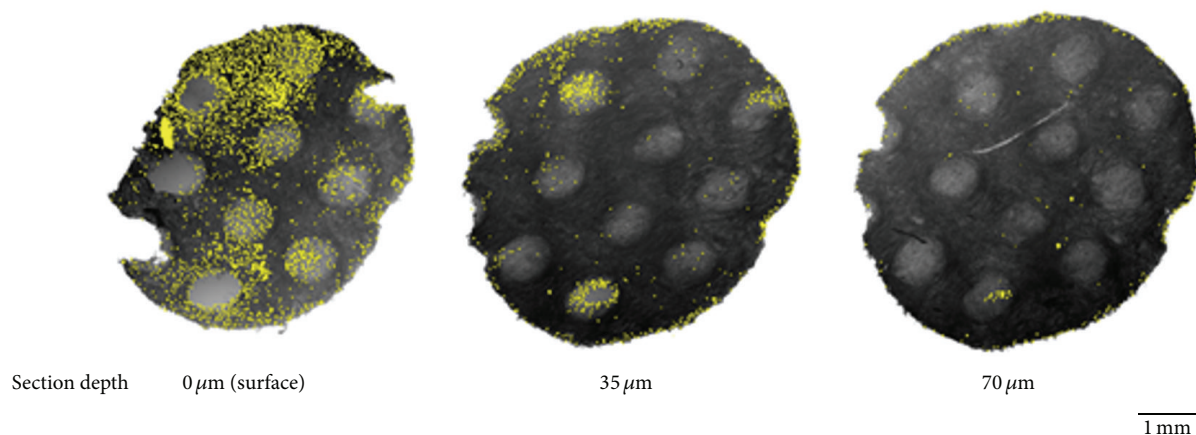


FIGURE 4: Consecutive frontal images of electrospun scaffolds seeded with human dermal fibroblasts stained with DAPI (yellow). Note how data management can be monitored by examining sections prior to image acquisition. Once some predetermined threshold of cells has been detected in the scaffold frontal sections the data sets are prepared for  $z$ -stack assembly. In this example, the majority of cells were present in the first  $70\ \mu\text{m}$  of the sample and subsequent frontal sections were excluded from the analysis. The large scale pores present in this scaffold were used to align the samples in the vertical direction prior to  $z$ -stack assembly.

cells' position to be visible. Because cells tend to primarily occupy the surface and sides of the represented scaffold we created a digital slice in the scaffold and rotated each half away to better reveal the position of cells that were embedded within the depth of the electrospun scaffold (Figure 3(d)).

### 3. Discussion

**3.1. Inadequacies of Current Techniques.** Conventional confocal optical imaging techniques are limited to approximately the first  $100\ \mu\text{m}$  of a fibrous scaffold and, as a result, cannot adequately provide data on the distribution of cells on a global scale within a large construct. Conventional cross-sectional analysis (sections taken perpendicular to the surface of a scaffold) can theoretically obtain data similar in nature to the data generated by a frontal section technique. While this is possible, pragmatically frontal sectioning has several advantages compared to conventional cross-sectioning. First, sections taken with this modified cryosectioning protocol retain better structural integrity and are subject to less physical damage. Second, only relevant frontal sections need be analyzed. As a hypothetical example, cells are seeded onto the top surface of an electrospun sample that is  $6\ \text{mm}$  in diameter and  $1\ \text{mm}$  thick. Then, assume this particular scaffold supports the infiltration of cells to a depth of  $200\ \mu\text{m}$  (cell penetration to this depth is common in our lab when seeding onto scaffolds consisting of large fibers—data not shown). It would require taking 120 total  $50\ \mu\text{m}$ -thick conventional cross-sections to capture data from the entire scaffold as cells would be present in each cross-section. From a practical perspective, it is unlikely that all 120 sections of this scaffold would be recovered, leaving gaps in the data set. In contrast, if frontal sections were taken, stained with DAPI, and assayed, the fluorescence marking the presence of cells would be present in only the first 5-6 frontal sections (Figure 4). Capturing data from only the relevant sections

of the sample simplifies data acquisition and accelerates image processing time. To summarize this example, cross-sectioning the entire scaffold would require 120 total sections, all of which would have to be stained and imaged whereas frontal sectioning would require 20 total sections, only 5 of which would have to be stained and imaged.

Storing frontal sections is also more convenient compared to storing conventional cross-sections. In the example described and using 48-well plates to store sections (each section in one well) from each scaffold, cross-sectioning would require 3 complete plates to store one scaffold whereas, using frontal sectioning, 2 separate scaffolds could be stored in a single plate. Because fewer wells are used, the total amount of imaging reagent (e.g., DAPI or other fluorescence markers) required for staining the frontal sections is greatly reduced compared to the conventional sections (despite cross-sectioned samples having a smaller volume, the amount of reagent necessary to cover a sample is dependent on the sample thickness which, in this case, is the same). From a data output standpoint, cross-sections depict the extent of cellular infiltration at a specific location (as does confocal microscopic analysis); data obtained from a frontal section reflects how local features impact the depth of penetration over a large surface area. This type of data might otherwise be lost in a conventional cross-section. In our study, despite the large scale nature of the pores induced by air impedance electrospinning that were present in the scaffolds, it was not possible to clearly identify these features in conventional cross-sectional analysis whereas they are easily distinguished in frontal sections (Figure 5).

**3.2. 3D Modeling.** As noted, cell distribution and the extent of cell infiltration can be rapidly determined from individual frontal sections (Figure 4). In this figure the scaffold sections have been aligned, placed side-by-side for examination, and projected with the appropriate depth and scaling

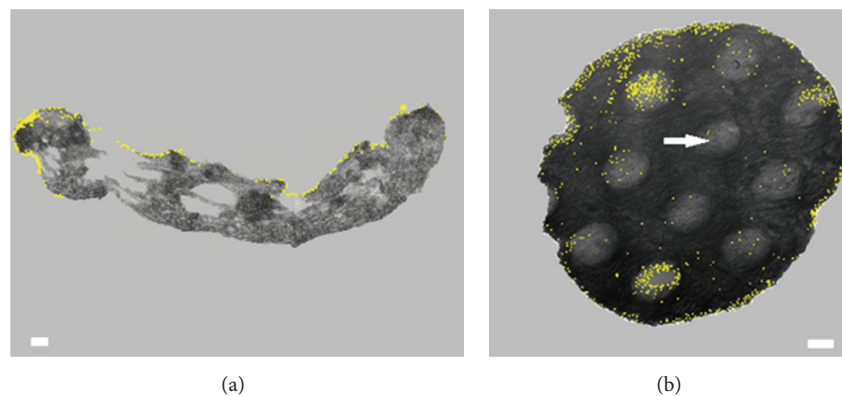


FIGURE 5: Cross-section (a) and frontal section (b) of an air impedance scaffold seeded with human dermal fibroblasts (yellow). Notice how the spatial scaffold properties, such as the macropores (arrow), are easily visible in the frontal section whereas in the cross-section no landmarks can be confidently identified. The ability to recognize scaffold features (e.g., macropores) improves our ability to correlate certain cellular events (e.g., infiltration) with changes in scaffold architectures. Left scale bar =  $200\ \mu\text{m}$  (for (a), cross-section image), right scale bar =  $500\ \mu\text{m}$  (for (b), frontal section image).

legends. However, frontal sections are highly amenable to 3D reconstruction and modeling. Entire scaffolds may be reconstructed in this manner.

Insufficient interfiber spacing and low scaffold porosity (despite the enormous void space that is present in these constructs) are commonly cited as factors that limit the penetration of cells into an electrospun scaffold. With caveats, our limited observations in this study largely support these assumptions. Scaffolds produced by air impedance electrospinning exhibit regions of lower fiber density and increased interfiber distances (Figure 4,  $35\ \mu\text{m}$  deep frontal section) which support localized areas of increased cellular penetration. However, this same analysis reveals that scattered cells are present in regions adjacent to these large scale features. It is unclear at this time if these scattered cells represent cells that have directly penetrated the scaffold or if these cells represent a population that first entered the large scale pores and then migrated laterally to reach these domains.

#### 4. Conclusions

We described a modified cryosectioning protocol that addresses a major limitation in the analysis of electrospun scaffolds. This method provides unambiguous data concerning the extent to which cells penetrate a scaffold on a global scale. Through the utilization of this frontal cryosectioning protocol researchers will be able to make definitive conclusions regarding how cellular infiltration and ECM interactions are influenced by specific scaffold structural properties. This information will lead to better scaffold design and an improved understanding of cellular infiltration.

#### Conflict of Interests

The authors declare that there is no conflict of interests regarding the publication of this paper.

#### Acknowledgment

The authors would like to thank the entire VCU microscopy staff for their assistance with this work.

#### References

- [1] J. A. Matthews, G. E. Wnek, D. G. Simpson, and G. L. Bowlin, "Electrospinning of collagen nanofibers," *Biomacromolecules*, vol. 3, no. 2, pp. 232–238, 2002.
- [2] D. G. Simpson, B. S. Jha, C. E. Ayres et al., "Electrospun collagen: a tissue engineering scaffold with unique functional properties in a wide variety of applications," *Journal of Nanomaterials*, vol. 2011, Article ID 348268, 15 pages, 2011.
- [3] P. A. Madurantakam, C. P. Cost, D. G. Simpson, and G. L. Bowlin, "Science of nanofibrous scaffold fabrication: strategies for next generation tissue-engineering scaffolds," *Nanomedicine*, vol. 4, no. 2, pp. 193–206, 2009.
- [4] C. P. Grey, S. T. Newton, G. L. Bowlin, T. W. Haas, and D. G. Simpson, "Gradient fiber electrospinning of layered scaffolds using controlled transitions in fiber diameter," *Biomaterials*, vol. 34, no. 21, pp. 4993–5006, 2013.
- [5] M. J. McClure, S. A. Sell, D. G. Simpson, B. H. Walpoth, and G. L. Bowlin, "Tri-layered electrospinning to mimic native arterial architecture using polycaprolactone, elastin, and collagen: a preliminary study," *Journal of visualized experiments*, vol. 47, article 2084, 2011.
- [6] M. A. Woodruff and D. W. Hutmacher, "The return of a forgotten polymer—polycaprolactone in the 21st century," *Progress in Polymer Science*, vol. 35, no. 10, pp. 1217–1256, 2010.
- [7] C. B. Weinberg and E. Bell, "A blood vessel model constructed from collagen and cultured vascular cells," *Science*, vol. 231, no. 4736, pp. 397–400, 1986.
- [8] I. Woods and T. C. Flanagan, "Electrospinning of biomimetic scaffolds for tissue-engineered vascular grafts: threading the path," *Expert Review of Cardiovascular Therapy*, vol. 12, no. 7, pp. 815–832, 2014.

- [9] Y. Zhang, H. Ouyang, T. L. Chwee, S. Ramakrishna, and Z.-M. Huang, "Electrospinning of gelatin fibers and gelatin/PCL composite fibrous scaffolds," *Journal of Biomedical Materials Research. Part B Applied Biomaterials*, vol. 72, no. 1, pp. 156–165, 2005.
- [10] C. P. Barnes, S. A. Sell, E. D. Boland, D. G. Simpson, and G. L. Bowlin, "Nanofiber technology: designing the next generation of tissue engineering scaffolds," *Advanced Drug Delivery Reviews*, vol. 59, no. 14, pp. 1413–1433, 2007.
- [11] E. D. Boland, B. D. Coleman, C. P. Barnes, D. G. Simpson, G. E. Wnek, and G. L. Bowlin, "Electrospinning polydioxanone for biomedical applications," *Acta Biomaterialia*, vol. 1, no. 1, pp. 115–123, 2005.
- [12] M. J. McClure, P. S. Wolfe, D. G. Simpson, S. A. Sell, and G. L. Bowlin, "The use of air-flow impedance to control fiber deposition patterns during electrospinning," *Biomaterials*, vol. 33, no. 3, pp. 771–779, 2012.
- [13] L. Moroni, R. Licht, J. de Boer, J. R. de Wijn, and C. A. van Blitterswijk, "Fiber diameter and texture of electrospun PEOT/PBT scaffolds influence human mesenchymal stem cell proliferation and morphology, and the release of incorporated compounds," *Biomaterials*, vol. 27, no. 28, pp. 4911–4922, 2006.
- [14] S. H. Lim and H.-Q. Mao, "Electrospun scaffolds for stem cell engineering," *Advanced Drug Delivery Reviews*, vol. 61, no. 12, pp. 1084–1096, 2009.
- [15] U. Boudriot, R. Dersch, A. Greiner, and J. H. Wendorff, "Electrospinning approaches toward scaffold engineering—a brief overview," *Artificial Organs*, vol. 30, no. 10, pp. 785–792, 2006.
- [16] J. Lannutti, D. Reneker, T. Ma, D. Tomasko, and D. Farson, "Electrospinning for tissue engineering scaffolds," *Materials Science & Engineering C*, vol. 27, no. 3, pp. 504–509, 2007.
- [17] M. Horst, S. Madduri, V. Milleret, T. Sulser, R. Gobet, and D. Eberli, "A bilayered hybrid microfibrous PLGA–Acellular matrix scaffold for hollow organ tissue engineering," *Biomaterials*, vol. 34, no. 5, pp. 1537–1545, 2013.
- [18] B. M. Baker, A. O. Gee, R. B. Metter et al., "The potential to improve cell infiltration in composite fiber-aligned electrospun scaffolds by the selective removal of sacrificial fibers," *Biomaterials*, vol. 29, no. 15, pp. 2348–2358, 2008.
- [19] F. Pampaloni, E. G. Reynaud, and E. H. K. Stelzer, "The third dimension bridges the gap between cell culture and live tissue," *Nature Reviews Molecular Cell Biology*, vol. 8, no. 10, pp. 839–845, 2007.
- [20] D. Semwogerere and E. R. Weeks, "Confocal microscopy," in *Encyclopedia of Biomaterials and Biomedical Engineering*, Taylor & Francis, 2005.
- [21] B. M. Whited, M. C. Hofmann, P. Lu et al., "Dynamic, non-destructive imaging of a bioengineered vascular graft endothelium," *PLoS ONE*, vol. 8, no. 4, Article ID e61275, 2013.
- [22] P. Deshpande, R. McKean, K. A. Blackwood et al., "Using poly(lactide-co-glycolide) electrospun scaffolds to deliver cultured epithelial cells to the cornea," *Regenerative Medicine*, vol. 5, no. 3, pp. 395–401, 2010.
- [23] H. M. Powell and S. T. Boyce, "Engineered human skin fabricated using electrospun collagen-PCL blends: morphogenesis and mechanical properties," *Tissue Engineering Part A*, vol. 15, no. 8, pp. 2177–2187, 2009.
- [24] C. E. Ayres, B. S. Jha, S. A. Sell, G. L. Bowlin, and D. G. Simpson, "Nanotechnology in the design of soft tissue scaffolds: innovations in structure and function," *Wiley Interdisciplinary Reviews: Nanomedicine and Nanobiotechnology*, vol. 2, no. 1, pp. 20–34, 2010.
- [25] B. S. Jha, R. J. Colello, J. R. Bowman et al., "Two pole air gap electrospinning: Fabrication of highly aligned, three-dimensional scaffolds for nerve reconstruction," *Acta Biomaterialia*, vol. 7, no. 1, pp. 203–215, 2011.
- [26] S. B. Kritchevsky, T. Shimakawa, G. S. Tell et al., "Dietary antioxidants and carotid artery wall thickness: the ARIC study," *Circulation*, vol. 92, no. 8, pp. 2142–2150, 1995.
- [27] C. Xu, R. Inai, M. Kotaki, and S. Ramakrishna, "Electrospun nanofiber fabrication as synthetic extracellular matrix and its potential for vascular tissue engineering," *Tissue Engineering*, vol. 10, no. 7–8, pp. 1160–1168, 2004.
- [28] D. Brown, J. Lydon, M. McLaughlin, A. Stuart-Tilley, R. Tyszkowski, and S. Alper, "Antigen retrieval in cryostat tissue sections and cultured cells by treatment with sodium dodecyl sulfate (SDS)," *Histochemistry and Cell Biology*, vol. 105, no. 4, pp. 261–267, 1996.

## Research Article

# Low-Temperature Sintering Bonding Using Silver Nanoparticle Paste for Electronics Packaging

Wei Guo,<sup>1</sup> Zhi Zeng,<sup>2</sup> Xiaoying Zhang,<sup>1</sup> Peng Peng,<sup>3</sup> and Shanping Tang<sup>1</sup>

<sup>1</sup>*School of Mechanical Engineering and Automation, Beihang University, Beijing 100191, China*

<sup>2</sup>*School of Mechanical, Electronic, and Industrial Engineering, University of Electronic Science and Technology of China, Chengdu 611731, China*

<sup>3</sup>*Mechanical and Mechatronics Engineering, University of Waterloo, Waterloo, ON, Canada N2L 3G1*

Correspondence should be addressed to Zhi Zeng; zhizeng@uestc.edu.cn

Received 22 January 2015; Revised 12 May 2015; Accepted 18 May 2015

Academic Editor: Changhong Ke

Copyright © 2015 Wei Guo et al. This is an open access article distributed under the Creative Commons Attribution License, which permits unrestricted use, distribution, and reproduction in any medium, provided the original work is properly cited.

Ag nanoparticles (NPs) with about 40 nm diameter covered with 5–8 nm organic shell were prepared by chemical reduction reaction. The thermal characteristics of Ag nanoparticle (NP) paste were measured by thermogravimetric analysis (TGA) and differential scanning calorimetry (DSC). The low-temperature sintering bonding processes using Ag NP paste were carried out at the temperature range of 150–350°C for 5 min under the pressure of 3 MPa. The microstructures of the sintered joint and the fracture morphology were evaluated by scanning electron microscopy (SEM). The shear strength was used to evaluate the mechanical property of the sintered joint. TGA-DSC test showed that the Ag content is approximately 95.5 mass% in Ag NP paste. The average shear strength of the joint fabricated at 250°C for 5 min under the pressure of 3 MPa was about 28 MPa, which could meet the requirements of electronics packaging working at high temperature. The joint shear strength increased with the increase of the sintering temperature due to much denser sintered Ag NPs and more comprehensive metallurgical bonds formed in the joint.

## 1. Introduction

Microelectronic devices and large power devices interconnection to the substrate is essential for device packaging, which provides paths for increased high power density electrical interconnection and high-efficiency heat dissipation [1]. However, the traditional eutectic or near eutectic Sn-Pb, Sn-Ag, and Sn-Ag-Cu solders and conductive adhesive used in die attachment are not reliable for high power density and high temperature electronic applications [2–4]. The Pb-containing solder alloys (Sn-Pb) have been temporarily exempted from the Restriction of Hazardous Substances (RoHS) directive in the European Union due to serious health threat to human being and heavy pollution to environment [5, 6]. On the other hand, it is reported that the joint using Pb-containing solder and Pb-free eutectic or near eutectic Sn-Ag and Sn-Ag-Cu solders is not suitable for long-term usage at elevated temperature due to crack formation at the intermetallic (IMC) layer between the solder and the metallized substrate on the devices [7–9]. Thus, the new

lead-free interconnection materials as alternative for device packaging have attracted much attention.

When material size is reduced down to nanoscale, some special characteristics, such as lower melting point [10], much higher surface energy [11], and diffusion coefficient [12], are significantly different from their parent materials in bulk. Therefore, a new low-temperature Pb-free interconnection method is developed using the sintering of nanomaterial, in particular, nanoparticles (NPs) [13–18]. Among those NPs, silver (Ag) has been demonstrated as a candidate because of its excellent properties, such as high electrical conductivity, high thermal conductivity, and excellent high temperature service performance [15]. At present, low-temperature sintering of Ag NPs has been developed for bonding of semiconductor devices onto metallized substrate [16–21]. Unlike traditional liquid solder wetting, solid-liquid interfacial reaction, and solidification process, Ag NPs sintering bonding process is achieved under quite low temperatures, usually at 150–350°C, through atomic diffusion and NP consolidation.

Organic compounds are usually used to disperse and stabilize Ag NPs, which will be adsorbed on the surface of Ag NPs. During the sintering process, the removal of organic shell is a requisite by heating and thus being certain of the temperature is needed. After sintering process, the joint shows high melting point of pure Ag (about 960°C) and excellent electrical and thermal properties as that of bulk Ag. Thereby, these sintered Ag NP joints produced at relatively low temperatures (below 350°C) could be used at elevated temperatures (beyond 350°C) at which the conventional solder joints could fail. Furthermore, this promising low-temperature Ag NPs sintering process has wide potential applications in flexible electronics, including rapid prototyping [22], flat-panel printing [23], organic electronics [24], and low-cost disposable microelectronic devices on plastic substrates applications [25]. However, the microstructure evolution of the sintered joint during the sintering process is less studied. On the other hand, usually, the Ag NPs application is restricted by the long sintering times as it requires about 20–30 min [26].

In this paper, Ag NP paste was fabricated by chemical reduction method. The morphology and size distribution of Ag NPs have been observed by scanning electron microscopy (SEM) and transmission electron microscopy (TEM). Thermogravimetric analysis (TGA) and differential scanning calorimetry (DSC) were used to evaluate thermal characteristics of Ag NP paste. The rapid sintering experiment was performed in the furnace at air atmosphere. The mechanical property of the joint was evaluated using shear strength. The microstructure evolutions of the joint and the fracture surface morphology were also observed by SEM.

## 2. Materials and Methods

Ag NPs used in the experiment were prepared by modified reducing silver nitrate ( $\text{AgNO}_3$ ) with ethylene glycol in the presence of polyvinylpyrrolidone (PVP) [27]. All of the chemical reagents were of analytical grade. First, 20 mL ethylene glycol solution of 0.3 M  $\text{AgNO}_3$  and 40 mL solution of PVP (0.9 M, K30) were prepared, respectively. The ethylene glycol solution was then heated to the reaction temperature of 160°C. The PVP solution was injected into the silver nitrite solution at a constant rate of 0.3 mL  $\text{s}^{-1}$ . When the solution color changed from colorless to gray (indicating the chemical reaction is completed), the solution was cooled rapidly through adding deionized water into the hot solution. Then, the Ag NP paste was collected by condensing the solution in a centrifuge (TW16-WS) with 7000 rpm for 30 min.

TGA and DSC analyses (STA 449 F3) were performed in air with the increase rate of 10.00 K  $\text{min}^{-1}$  to determine the organic content and the thermal properties of Ag NP paste. The morphology of Ag NPs and their size distribution were observed by SEM (JEOL 1530) and TEM (JEM-2100).

The nickel (Ni) and Ag layers plated Copper (Cu) discs were adopted as the electronics packaging connection samples in this work. The upper and bottom sizes of Cu discs were  $\Phi$  6 mm  $\times$  5 mm and  $\Phi$  10 mm  $\times$  5 mm, respectively. Prior to bonding, the as-received Cu discs were ultrasonically

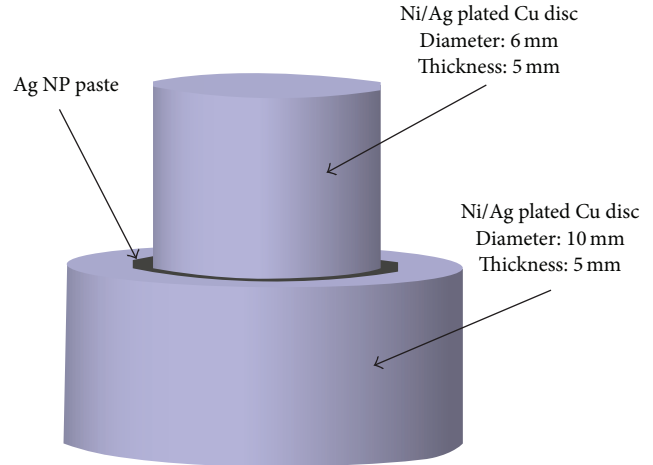


FIGURE 1: Schematic illustration of the sintering joint using Ag NP paste.

cleaned in acetone for 20 min to remove contaminants on the joining surface. Ag NP paste was blushed about 200  $\mu\text{m}$  on the surface of Cu discs and dried at 70°C on the heating plate for 10 min. And Ag NP paste was sandwiched between upper and bottom Cu discs (shown in Figure 1). The sintering experiments were performed in the muffle furnace in air atmosphere from 150 to 350°C for 5 min under the pressure of 3 MPa. In detail, the furnace was heated to sintering temperature, holding for about 20 min for uniform temperature, and then the joining assembly was put into the furnace and put the pressure on the assembly. After sintering process, the assembly was taken out from the furnace.

The shear strengths of the sintered joints were evaluated using a Gleeble thermomechanical simulator (1500 D) with a displacement speed of 5 mm  $\text{min}^{-1}$  at room temperature. The interfacial microstructures of the joints and fracture surfaces were examined by SEM (CS3400 and JEOL 1530).

## 3. Results and Discussion

**3.1. Morphologies of Ag NPs.** Figure 2(a) shows the typical morphology of as-prepared Ag NPs. It can be seen that most of Ag NPs are polyhedron in shape. The distribution of Ag NP size was in the range of 20–80 nm (shown in Figure 3) and the average diameter of Ag NPs was about 40 nm. Transmission electron microscopy (TEM) image of Ag NPs is displayed in Figure 2(b). An organic shell with a thickness of 5–8 nm is observed on the surface of Ag NPs, which prevented the oxidation and aggregation of Ag NPs.

**3.2. Thermal Characteristics of Ag NP Paste.** Figure 4 shows the TGA and DSC results of Ag NP paste. Two exothermic peaks in DSC curve are recognized at around 350 and 400°C, respectively. When the temperature is above approximately 150°C, some organic compositions covered on Ag NP may start to vaporize, oxidize, or burn out by reacting with oxygen in air or being adsorbed on Cu disc surface [28]. As known, nanoparticles tend to aggregate because of much

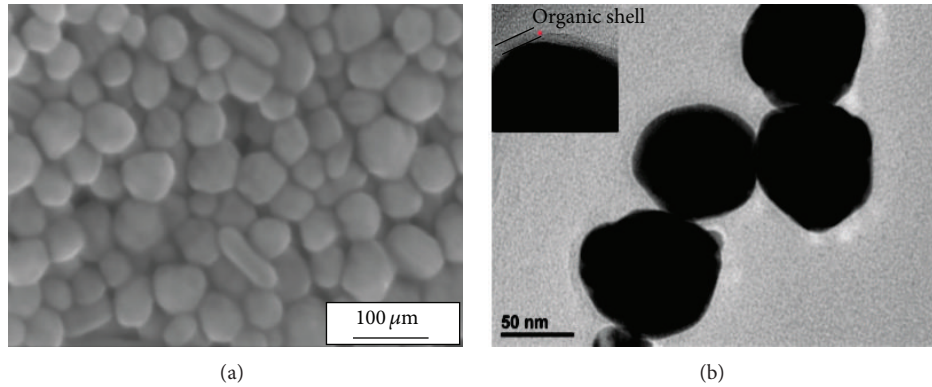


FIGURE 2: SEM (a) and TEM (b) images of Ag NPs.

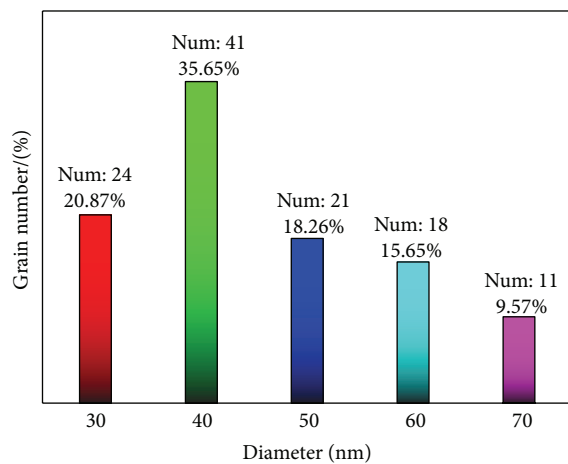


FIGURE 3: Ag NP size distribution.

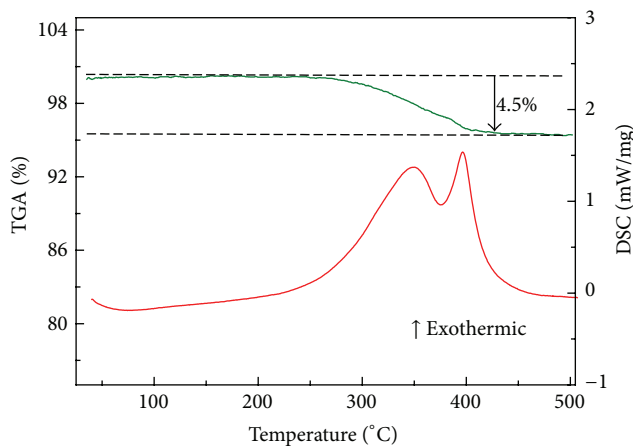


FIGURE 4: TGA and DSC curves of Ag NP paste.

higher surface energy [18, 29]. The exothermic peak at around 350°C is mainly due to the decomposition of organic shell. The exothermic peak at ~400°C is possibly attributed to the oxidation of C derived from PVP [30]. As shown in TGA curve, the weight of the dried paste gradually decreases as

the temperature increases from room temperature to 450°C, which can be attributed to vaporization and decomposition of the organic compounds in the paste. The Ag content of Ag NP paste was approximately 95.5 mass%, which is significantly higher than 85 mass% in conventional Ag NP paste [13]. Since the bonding process is atom diffusion and sintering of Ag NPs with the vaporization and decomposition of the organic components. When the organic component reduces, Ag NPs aggregate and sinter together under the annealing temperature and pressure. Because of the much lower organic content of the Ag NP paste used in this research, it is reasonable to predict that it will have lower sintering temperature and shorter sintering time during bonding compared with the conventional Ag NP paste.

**3.3. Microstructures of the Sintered Joint.** Figures 5(a)–5(c) give the low magnification microstructures of the joint at the temperature of 150°C, 250°C, and 350°C, respectively. Macrocracks were observed between Ag coated layer and Ag NP sintered zone of the joint at 150°C as arrows indicated in Figure 5(a). Since only few organics vaporized and oxidized at the temperature of 150°C as shown in DSC curve in Figure 4, these cracks format the interlayer between Ag coated substrate and Ag NP sintered zone due to the residual organics in Ag NP paste. No significant macrocracks could be observed when the sintering temperature increased to 250°C and 350°C (see Figures 5(b)–5(c)), indicating that the joint strength would be increased. Meanwhile, a high magnification image of the connection areas of the joint is given in Figures 5(d)–5(f). It was found that the sintered zone of the joint at 150°C (Figure 5(d)) was composed of small size Ag NPs (several hundred nanometer diameter) with high percentage of pores. With the temperature increasing to 250°C, a uniform and denser Ag NP sintered layer was formed between the Ni/Ag plated Cu discs (Figure 5(e)). Since the more intense sintering happened at higher temperature, Ag NPs sintered and grew together causing the increase of material density and decrease of the porosity. As the sintering temperature reached 350°C, much better metallurgical combination of joining zone was attained as shown in Figure 5(f). Some submicron voids still existed in the sintered layer but the porosity of the joint

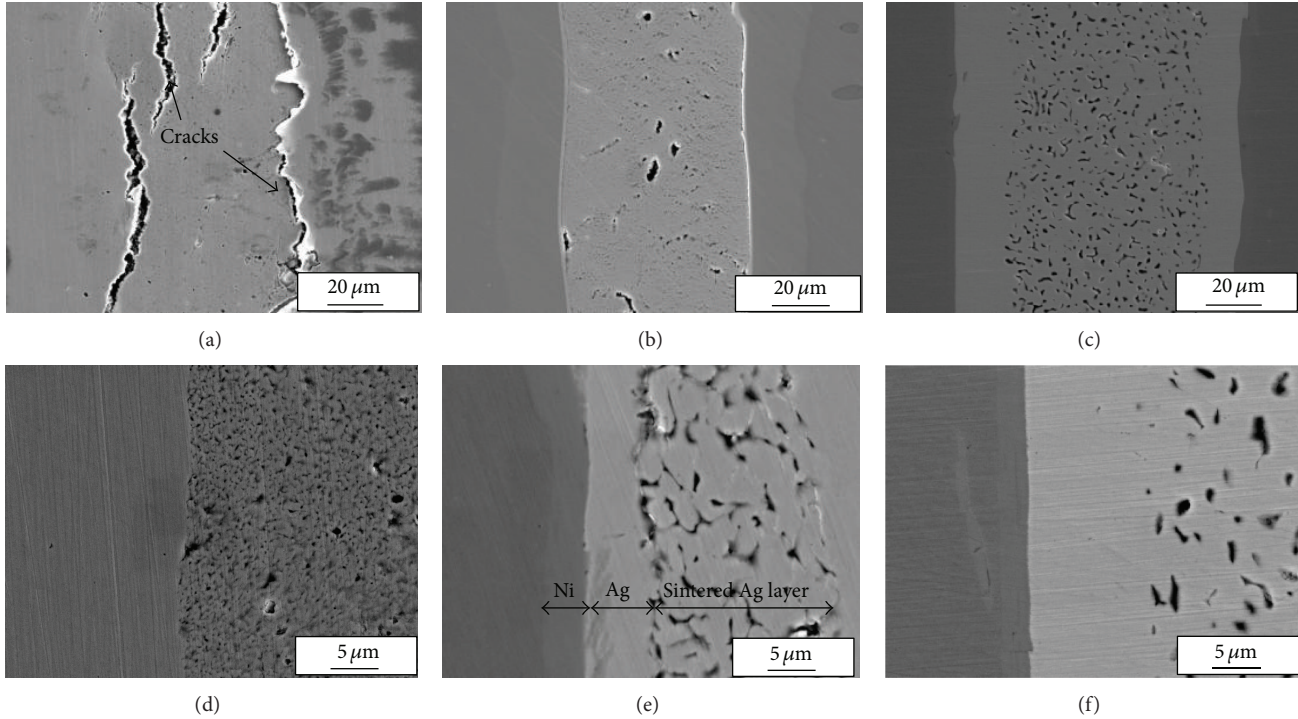


FIGURE 5: SEM images of interface microstructure of joints with different sintering temperatures: (a) low magnification at 150°C; (b) low magnification at 250°C; (c) low magnification at 350°C; (d) high magnification at 150°C; (e) high magnification at 250°C; (f) high magnification at 350°C.

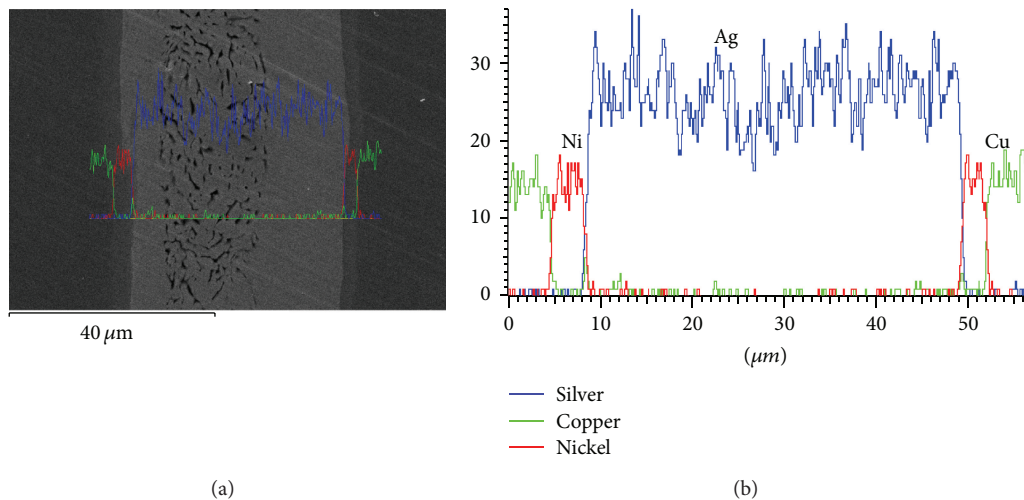


FIGURE 6: Microstructure of the joint: (a) line scan; (b) element distribution.

decreased compared with that at 250°C. It is worth mentioning that the volume of the single pore increased with the sintering temperature from a few hundreds of nanometers to several microns. Benefiting from such porous structures, this sintered material could help relieve the thermomechanical stresses during operation. Moreover, the presence of such pores could balance the elastic modulus or other mechanical properties like strength and fatigue properties [31] of joints with the substrates, especially the plastic substrates. The chemical element distributions across the joining interface

are shown in Figure 6. It can be seen that Ag content drops much sharply at the edge of Ni coating, and Ni coating does well on impeding Ag diffusion due to much lower solution of Ag in Ni. No voids are discovered near the edge of Ni coating.

**3.4. Mechanical Property of the Joints.** Figure 7 shows the average shear strength of the sintered joints as a function of sintering temperature. The average strength of the joints at 150°C and 200°C was about 8 MPa and 10 MPa,

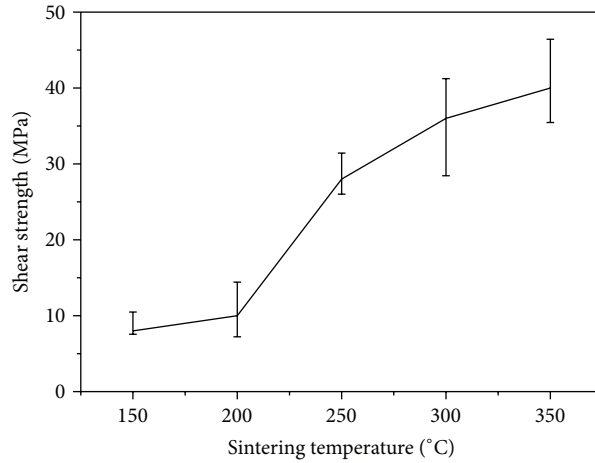


FIGURE 7: Average shear strength of sintered joints at different sintering temperatures.

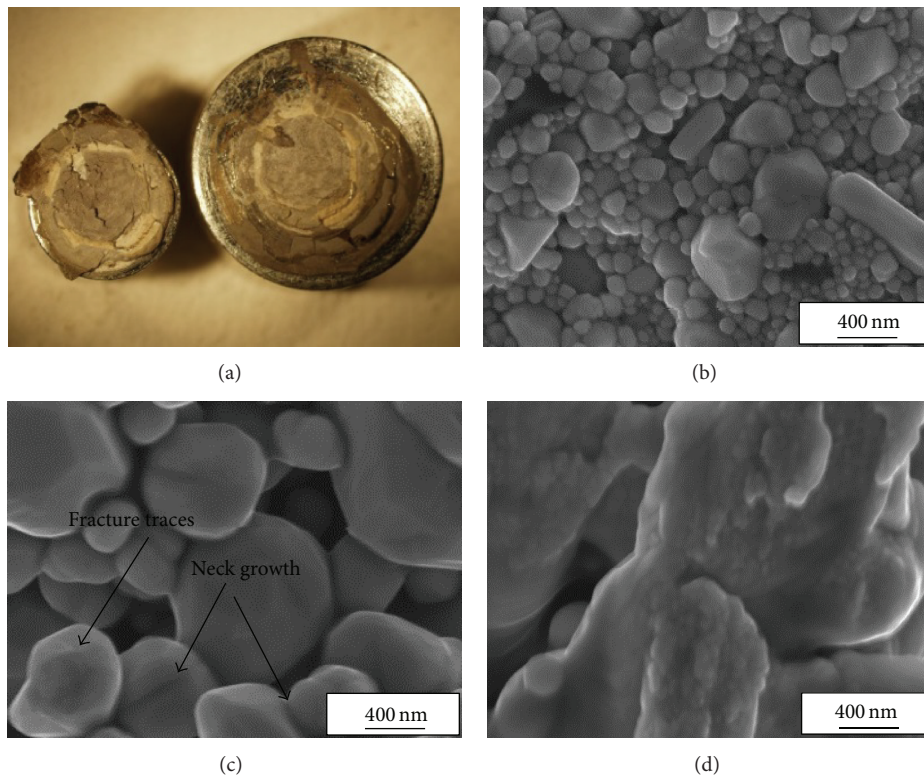


FIGURE 8: The fracture surface morphology of the joints. (a) Macromorphology. (b) Fracture at 150°C. (c) Fracture at 250°C. (d) Fracture at 350°C.

respectively. When the sintering temperature increased to 250°C, the average shear strength of the joint significantly increased to 28 MPa, which is comparable to the traditional lead solder and lead-free solder, suggesting that it could meet the requirements of electronic packaging (24 MPa) in practical applications [13]. The average shear strength of 40 MPa was achieved at sintering temperature of 350°C. The higher temperatures are beneficial to the contact, diffusion, and sintering process between Ag NPs and substrate [32]. Therefore, higher sintering temperature could promote

the sintering between Ag NPs and also between Ag NPs and substrates, which results in a better strength of joint.

Figure 8(a) shows the macrofracture surface of the joint. The ring-like structure on the fracture surface of the sintered joint as observed by Rautio et al. [33] due to the coffee ring effect caused by the rheological property of Ag NP paste was not obvious because of a very high content of Ag NPs in the paste. Figures 8(b)–8(d) show the fracture morphology of sintered Ag NPs joint at different temperatures from 150 to 350°C. At low temperature of 150°C (Figure 8(b)),

the majority of the Ag NPs were sintered together with clear the edges and corners, indicating that the Ag NPs maintained the original shape and sintering was feeble at low temperature. When the sintering temperature is 250°C (Figure 8(c)), obvious neck growth and particle growth were observed and sintering densification occurred. At 350°C, the particle size grew further and large grain appeared resulting in a much denser sintering structure (see Figure 8(d)). The Ag NP size increased with the increase of the sintering temperature, as shown in Figures 8(b)–8(d). After measuring, it was found that Ag NPs on fracture surface sintered at 150°C, 250°C, and 350°C were about 150 nm, 0.8  $\mu\text{m}$ , and 1.2  $\mu\text{m}$ , respectively. The phenomenon can be explained by the fact that the organic shell covered on Ag NPs decomposed faster and more completely at higher temperature [33]. The diffusion rate increased with the increasing of the sintering temperature, which resulted in the rapid coarsening of Ag NPs. Moreover, at high temperatures such as 250 to 350°C in this work, the Ag NPs became rounded and the corners were tuned (Figures 8(c) and 8(d)), which suggested that the liquid phase might appear during sintering. The liquid involved sintering would have much higher sintering speed than that of solid state sintering. It is worth mentioning that this liquid might only present on the surface of Ag NPs, the so-called surface melting [34], because the sintering temperatures are below the melting temperature of Ag NPs.

#### 4. Conclusions

Ag NP paste with an average diameter of about 40 nm covered with organic shell 5–8 nm thick was synthesized via chemical reduction reaction. The organic shell can prevent the oxidation and aggregation of Ag NPs. TGA-DSC curves showed that the silver content was approximately 95.5 mass% in Ag NP paste and the organic shell vaporized, oxidized, or decomposed by reacting with the oxygen during the heating process in air. The sintered joint with Ag NP paste was successfully achieved at different temperatures with a rapid sintering process. With the increase of the sintering temperature, the interfacial microstructure of joint became denser. The average shear strength of the joint fabricated at 250°C for 5 min under 3 MPa is 28 MPa because of metallurgical bond formed between the silver plated layer and the sintered Ag NP layer, which could meet the requirements of electronics packaging. It suggests that this Ag NP paste as an alternative low-temperature connection material is suitable for high power semiconductor devices packaging with a rapid sintering process, which could also be applied to flexible electronic packaging.

#### Conflict of Interests

The authors declare that there is no conflict of interests regarding the publication of this paper.

#### Acknowledgments

This work was supported by International Science and Technology Cooperation Program of China (Grant no.

2013DFR50590) and the Fundamental Research Funds for the central University (30420100042, 3042012112, and 30420120771).

#### References

- [1] R. R. Tummala, E. J. Rymaszewski, and A. G. Klopfenstein, *Microelectronics Packaging Handbook: Semiconductor Packaging, Part II*, Chapman & Hall, New York, NY, USA, 1997.
- [2] H. K. Kim, H. K. Liou, and K. N. Tu, “Three-dimensional morphology of a very rough interface formed in the soldering reaction between eutectic SnPb and Cu,” *Applied Physics Letters*, vol. 18, pp. 2337–2339, 1995.
- [3] F. P. McCluskey, M. Dash, Z. Wang, and D. Huff, “Reliability of high temperature solder alternatives,” *Microelectronics Reliability*, vol. 46, no. 9–11, pp. 1910–1914, 2006.
- [4] I. E. Anderson, “Development of Sn-Ag-Cu and Sn-Ag-Cu-X alloys for Pb-free electronic solder applications,” in *Lead-Free Electronic Solders*, pp. 55–76, Springer, New York, NY, USA, 2007.
- [5] K. J. Puttlitz and G. T. Galyon, “Impact of the ROHS directive on high-performance electronic systems,” in *Lead-Free Electronic Solders*, pp. 347–365, Springer, New York, NY, USA, 2007.
- [6] Y. Li, K.-S. Moon, and C. P. Wong, “Electronics without lead,” *Science*, vol. 308, no. 5727, pp. 1419–1420, 2005.
- [7] A. Katz, C. H. Lee, and K. L. Tai, “Advanced metallization schemes for bonding of InP-based laser devices to CVD-diamond heatsinks,” *Materials Chemistry and Physics*, vol. 37, no. 4, pp. 303–328, 1994.
- [8] A. J. Tessmer, L. S. Plano, and D. L. Dreifus, “High-temperature operation of polycrystalline diamond field-effect transistors,” *IEEE Electron Device Letters*, vol. 14, no. 2, pp. 66–68, 1993.
- [9] Y. Sugawara, “SiC devices for high voltage high power applications,” *Materials Science Forum*, vol. 457–460, pp. 963–968, 2004.
- [10] M. Zhang, M. Y. Efremov, F. Schiettekatte et al., “Size-dependent melting point depression of nanostructures: nanocalorimetric measurements,” *Physical Review B*, vol. 62, no. 15, pp. 10548–10557, 2000.
- [11] Q. Jiang, S. H. Zhang, and J. C. Li, “Grain size-dependent diffusion activation energy in nanomaterials,” *Solid State Communications*, vol. 130, no. 9, pp. 581–584, 2004.
- [12] K. Katayama, H. Nomura, H. Ogata, and T. Eitoku, “Diffusion coefficients for nanoparticles under flow and stop-flow conditions,” *Physical Chemistry Chemical Physics*, vol. 11, no. 44, pp. 10494–10499, 2009.
- [13] E. Ide, S. Angata, A. Hirose, and K. F. Kobayashi, “Metal-metal bonding process using Ag metallo-organic nanoparticles,” *Acta Materialia*, vol. 53, no. 8, pp. 2385–2393, 2005.
- [14] J. R. Groza and A. Zavaliangos, “Nanostructured bulk solids by field activated sintering,” *Reviews on Advanced Materials Science*, vol. 5, no. 1, pp. 24–33, 2003.
- [15] M. Jakubowska, M. Jarosz, K. Kielbasinski, and A. Młoniak, “New conductive thick-film paste based on silver nanopowder for high power and high temperature applications,” *Microelectronics Reliability*, vol. 51, no. 7, pp. 1235–1240, 2011.
- [16] J. G. Bai, Z. Z. Zhang, J. N. Calata, and G.-Q. Lu, “Low-temperature sintered nanoscale silver as a novel semiconductor device-metallized substrate interconnect material,” *IEEE Transactions on Components and Packaging Technologies*, vol. 29, no. 3, pp. 589–593, 2006.

- [17] J. Yan, G. Zou, X. Wang, H. Bai, F. Mu, and A. Wu, "Large-scale synthesis of Ag nanoparticles by polyol process for low temperature bonding application," in *Proceedings of the 12th International Conference on Electronic Packaging Technology and High Density Packaging (ICEPT-HDP '11)*, pp. 1–6, IEEE, Shanghai, China, August 2011.
- [18] K. S. Moon, H. Dong, R. Maric et al., "Thermal behavior of silver nanoparticles for low-temperature interconnect applications," *Journal of Electronic Materials*, vol. 34, no. 2, pp. 168–175, 2005.
- [19] J. Li, C. M. Johnson, C. Buttay, W. Sabbah, and S. Azzopardi, "Bonding strength of multiple SiC die attachment prepared by sintering of Ag nanoparticles," *Journal of Materials Processing Technology*, vol. 215, pp. 299–308, 2015.
- [20] S. Wang, M. Y. Li, H. J. Ji, and C. Q. Wang, "Rapid pressureless low-temperature sintering of Ag nanoparticles for high-power density electronic packaging," *Scripta Materialia*, vol. 69, no. 11–12, pp. 789–792, 2013.
- [21] K. S. Siow, "Mechanical properties of nano-silver joints as die attach materials," *Journal of Alloys and Compounds*, vol. 514, pp. 6–19, 2012.
- [22] W. S. Liao, T. Yang, E. T. Castellana, S. Kataoka, and P. S. Cremer, "A rapid prototyping approach to ag nanoparticle fabrication in the 10–100 nm range," *Advanced Materials*, vol. 18, no. 17, pp. 2240–2243, 2006.
- [23] M. Yang, M. W. Chon, J. H. Kim et al., "Mechanical and environmental durability of roll-to-roll printed silver nanoparticle film using a rapid laser annealing process for flexible electronics," *Microelectronics Reliability*, vol. 54, no. 12, pp. 2871–2880, 2014.
- [24] K. Kardarian, T. Busani, I. Osório et al., "Sintering of nanoscale silver coated textiles, a new approach to attain conductive fabrics for electromagnetic shielding," *Materials Chemistry and Physics*, vol. 147, no. 3, pp. 815–822, 2014.
- [25] M. Layani, M. Grouchko, S. Shemesh, and S. Magdassi, "Conductive patterns on plastic substrates by sequential inkjet printing of silver nanoparticles and electrolyte sintering solutions," *Journal of Materials Chemistry*, vol. 22, no. 29, pp. 14349–14352, 2012.
- [26] H. Yu, L. L. Li, and Y. J. Zhang, "Silver nanoparticle-based thermal interface materials with ultra-low thermal resistance for power electronics applications," *Scripta Materialia*, vol. 66, no. 11, pp. 931–934, 2012.
- [27] Y. Sun and Y. Xia, "Shape-controlled synthesis of gold and silver nanoparticles," *Science*, vol. 298, no. 5601, pp. 2176–2179, 2002.
- [28] S. Li, P. Liu, and Q. Wang, "Study on the effect of surface modifier on self-aggregation behavior of Ag nano-particle," *Applied Surface Science*, vol. 263, pp. 613–618, 2012.
- [29] L. Mo, D. Liu, W. Li, L. Li, L. Wang, and X. Zhou, "Effects of dodecylamine and dodecanethiol on the conductive properties of nano-Ag films," *Applied Surface Science*, vol. 257, no. 13, pp. 5746–5753, 2011.
- [30] D. L. Chen, M. N. Liu, Q. Q. Chen et al., "Large-scale synthesis and enhanced visible-light-driven photocatalytic performance of hierarchical Ag/AgCl nanocrystals derived from freeze-dried PVP-Ag<sup>+</sup> hybrid precursors with porosity," *Applied Catalysis B: Environmental*, vol. 144, pp. 394–407, 2014.
- [31] J. Li, *Thermo-Mechanical Reliability of Sintered Silver Joint Versus Lead-Free Solder for Attaching Large Area Device*, Virginia Polytechnic Institute and State University (Materials Science and Engineering), Blacksburg, Va, USA, 2010.
- [32] G. S. Zou, J. F. Yan, F. W. Mu, A. Wu, J. Ren, and A. Hu, "Low temperature bonding of Cu metal through sintering of Ag nanoparticles for high temperature electronic application," *The Open Surface Science Journal*, vol. 3, no. 1, pp. 70–75, 2011.
- [33] J. Rautio, P. Perämäki, J. Honkamo, and H. Jantunen, "Effect of synthesis method variables on particle size in the preparation of homogeneous doped nano ZnO material," *Microchemical Journal*, vol. 91, no. 2, pp. 272–276, 2009.
- [34] H. A. Alarifi, M. Atiş, C. Özdoğan, A. Hu, M. Yavuz, and Y. Zhou, "Determination of complete melting and surface pre-melting points of silver nanoparticles by molecular dynamics simulation," *The Journal of Physical Chemistry C*, vol. 117, no. 23, pp. 12289–12298, 2013.

## Research Article

# Butterfly-Inspired 2D Periodic Tapered-Staggered Subwavelength Gratings Designed Based on Finite Difference Time Domain Method

Houxiao Wang,<sup>1,2,3</sup> Wei Zhou,<sup>2,3</sup> Er Ping Li,<sup>3</sup> and Rakesh Ganpat Mote<sup>3,4</sup>

<sup>1</sup>School of Mechanical Engineering, Jiangsu University, 301 Xuefu Road, Zhenjiang 212013, Jiangsu, China

<sup>2</sup>School of Mechanical and Aerospace Engineering, Nanyang Technological University, 50 Nanyang Avenue, Singapore 639798

<sup>3</sup>Advanced Photonics and Plasmonics Division, A\*STAR Institute of High Performance Computing, 1 Fusionopolis Way, No. 16-16 Connexis, Singapore 138632

<sup>4</sup>Department of Mechanical Engineering, Indian Institute of Technology Bombay, Powai, Mumbai 400076, India

Correspondence should be addressed to Houxiao Wang; wanghx@ujs.edu.cn, Wei Zhou; wzhou@cantab.net, and Er Ping Li; eplee@ihpc.a-star.edu.sg

Received 19 October 2014; Revised 23 December 2014; Accepted 18 January 2015

Academic Editor: Yaling Liu

Copyright © 2015 Houxiao Wang et al. This is an open access article distributed under the Creative Commons Attribution License, which permits unrestricted use, distribution, and reproduction in any medium, provided the original work is properly cited.

The butterfly-inspired 2D periodic tapered-staggered subwavelength gratings were developed mainly using finite difference time domain (FDTD) method, assisted by using focused ion beam (FIB) nanoscale machining or fabrication. The periodic subwavelength structures along the ridges of the designed gratings may change the electric field intensity distribution and weaken the surface reflection. The performance of the designed SiO<sub>2</sub> gratings is similar to that of the corresponding Si gratings (the predicted reflectance can be less than around 5% for the bandwidth ranging from 0.15 μm to 1 μm). Further, the antireflection performance of the designed *x*-unspaced gratings is better than that of the corresponding *x*-spaced gratings. Based on the FDTD designs and simulated results, the butterfly-inspired grating structure was fabricated on the silicon wafer using FIB milling, reporting the possibility to fabricate these FDTD-designed subwavelength grating structures.

## 1. Introduction

Nowadays, there is an increasing trend to learn from nature to analyze natural structures and develop bioinspired devices/elements through mimicking or replicating natural structures [1–11]. It has been reported that the moth eyes have inspired the researchers to develop antireflective structured photovoltaic materials and devices (e.g., solar cells) for higher light-to-electricity conversion efficiency [12–18], and the lotus leaves have excited the investigators to design the self-cleaning/hydrophobic structures or surfaces [19, 20]. Like the nanostructures of moth eyes and lotus leaves, the structures of butterfly wings, which may contribute to their own colors [2, 5–10, 21–30], carry the potential to develop new materials, techniques, and devices for different applications.

The reported butterfly-inspired technologies/products consist of the hydrophobic or self-cleaning materials/surfaces

[6–8, 21, 22], the high-efficiency solar panels [5, 9, 23, 24], the vapor or gas nanosensors [6, 8, 10, 25], the iridescent ZrO<sub>2</sub> photonic crystals [26], the optical beam splitter [27], and the magneto-optic structures [28]. Differently, in this study, the butterfly-inspired newly designed 2D periodic tapered-staggered subwavelength gratings were developed using finite difference time domain (FDTD) simulation method, assisted by using focused ion beam (FIB) nanoscale machining or fabrication (the already achieved grating designs and their antireflection performance were obtained based on FDTD simulation).

## 2. Materials and Methods

The butterfly species used in this study consisted of the *Palm King* and the *Hebomoia leucippe*. The FIB system was used

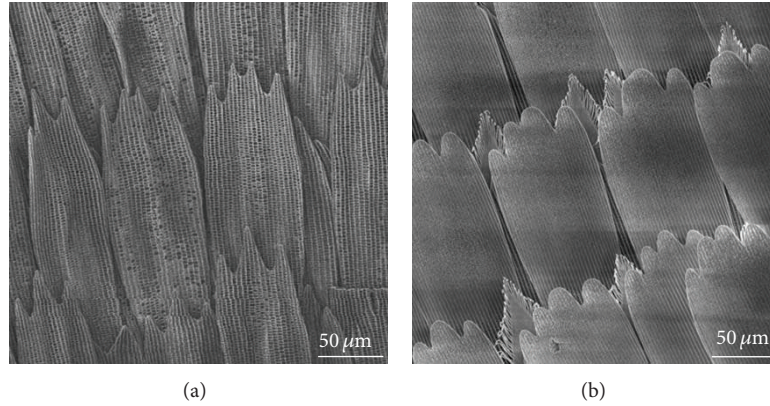


FIGURE 1: Pigmented microscales on butterfly wings for (a) *Palm King* and (b) *Hebomoia leucippe*.

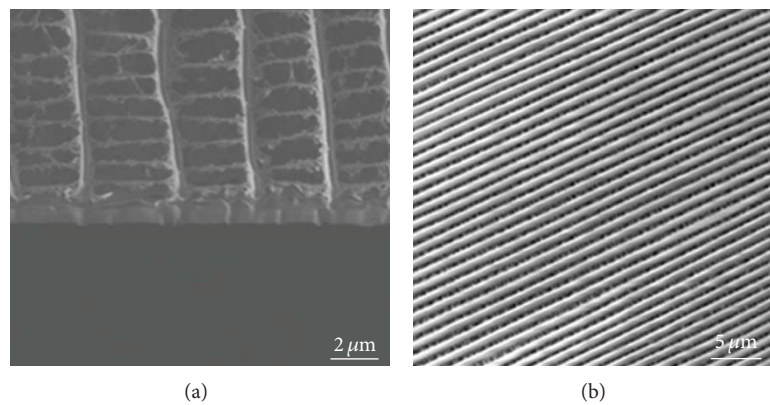


FIGURE 2: (a) Cross section after removing pigment granules using FIB and (b) flute-like gratings in the wing scales of *Hebomoia leucippe*.

for nanomachining and imaging. The FDTD method was utilized for design and optical performance computation. The designed grating structure was fabricated on the silicon wafer.

### 3. Structural Analysis for Butterfly Wings Using FIB Nanomachining

The butterfly wings are the translucent and/or pigmented chitin membranes covered with lots of transparent and/or pigmented microscopic light-interacting scales. These microscales may have the function for coloration, waterproofing characteristics (repel water-like roof tiles), and/or solar energy collection (Figure 1). These thin and nanopatterned chitin scales overlap one another, which may allow the dynamic control of light flow and photon interaction by selectively filtering out certain wavelengths through refraction, interference, and/or absorption while reflecting others for visual colorations, subject to the real scale structure and the scale layer distance.

The structures in the scales of the observed butterfly wings are shown in Figures 2 and 3. The general structures in each wing scale are grating-based which consist of the taper- or flute-shaped longitudinal ridges with subwavelength grating substructures and the transverse ribs with/without

ovoid pigment granules. The pigment granules on the cross ribs of the wing scales of the *Hebomoia leucippe* can be removed using FIB, and the exposed structures after FIB nanomachining are shown in Figures 2(a) and 3(b), which appear similar to those of the *Palm King* (Figure 3(a)) despite the flute-like grating structures shown in Figure 2(b).

### 4. 2D Periodic Tapered-Staggered Subwavelength Gratings

The inverse-V structures of the black wings of butterfly *Ornithoptera goliath* may achieve good antireflection property (99% absorption and 1% reflection in visible light spectrum 380–795 nm, the reflectance of the reverse V-type surface is around 1/13 of that in the flat plate). Thus, they show promising antireflection applications for the optical instruments, sensors, thermal detectors, and solar cells [24]. However, as shown in Figure 3, the observed tapered grating ridges have lots of subwavelength periodic grating substructures, whose antireflection performance has not been reported, without mentioning the other functions of these ridge-directional subwavelength periodic grating substructures.

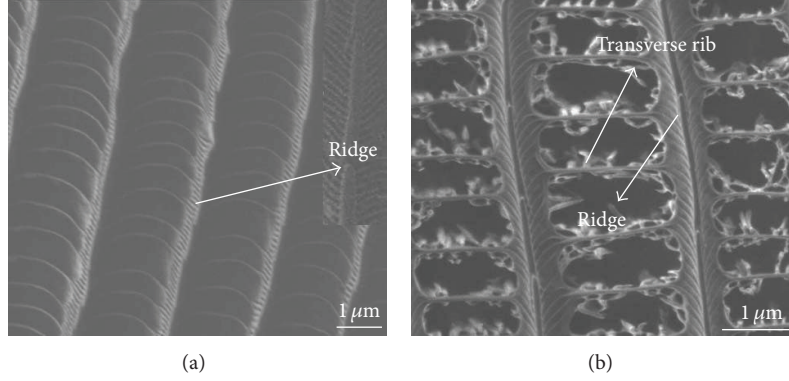


FIGURE 3: Subwavelength structures in the wing scales for (a) *Palm King* and (b) *Hebomoia leucippe*.

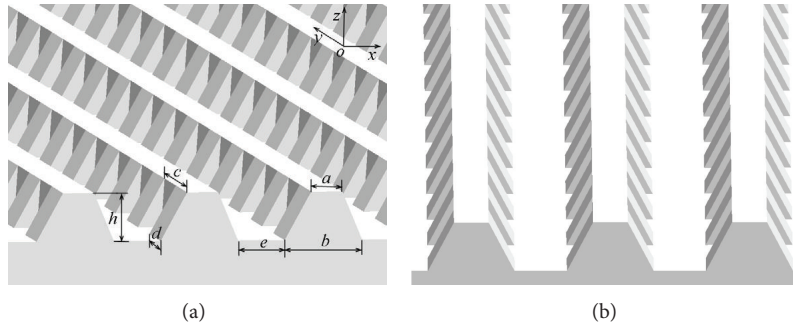


FIGURE 4: FDTD design of  $x$ -spaced 2D periodic tapered-staggered gratings.

TABLE 1: Geometry parameters for  $\text{SiO}_2$  gratings designed in Figure 4.

| $a$ (nm) | $b$ (nm) | $c$ (nm) | $d$ (nm) | $e$ (nm) | $h$ (nm) |
|----------|----------|----------|----------|----------|----------|
| 100      | 200      | 200      | 100      | 100      | 100      |

TABLE 2: Geometric dimensions for gratings designed in Figure 5.

| $a$ (nm) | $b$ (nm) | $c$ (nm) | $d$ (nm) | $h$ (nm) |
|----------|----------|----------|----------|----------|
| 50       | 100      | 100      | 50       | 200      |

Accordingly, inspired by the nanostructures observed in the scales of the butterfly wings (Figure 3), the 2D periodic tapered-staggered subwavelength gratings were developed. The designed 2D periodic tapered-staggered subwavelength gratings are shown in Figures 4 and 5 (the mimic design of the grating structures of the observed butterfly wings), and the designed grating dimensions are given in Tables 1 and 2. The calculated normal-incident reflectance for the designed gratings at various wavelengths and polarization angles is given in Figures 6–8, where the reference axis for the polarization angles ( $0^\circ$  and  $90^\circ$ ) is the  $x$ -axis.

Different from the reflective performance of the general right-angled gratings (geometric dimensions designed:  $\Lambda =$

200 nm,  $F = 50\%$ , and  $h = 200$  nm), the periodic subwavelength structures along the ridges of the 2D periodic tapered-staggered gratings may change the electric field intensity distribution (sensitive to light polarization) and weaken the surface reflection (Figure 6). Moreover, the performance of the designed 2D periodic tapered-staggered subwavelength  $\text{SiO}_2$  gratings is similar to that of the corresponding Si gratings, and the predicted reflectance can be less than around 5% for the bandwidth ranging from  $0.15 \mu\text{m}$  to  $1 \mu\text{m}$  (Figure 7). In addition, as shown in Figures 7 and 8, the antireflection performance of the gratings designed in Figure 5 and Table 2 is better than that of the gratings designed in Figure 4 and Table 1.

On the basis of the FDTD designs and simulated results, as shown in Figure 9, the butterfly-inspired 2D periodic tapered-staggered subwavelength grating structure was fabricated on the silicon substrate using FIB milling for reporting the possibility to fabricate these FDTD-designed grating structures.

## 5. Conclusions

The butterfly-inspired 2D periodic tapered-staggered subwavelength gratings were newly developed mainly using the FDTD method. The normal-incident reflectance of the

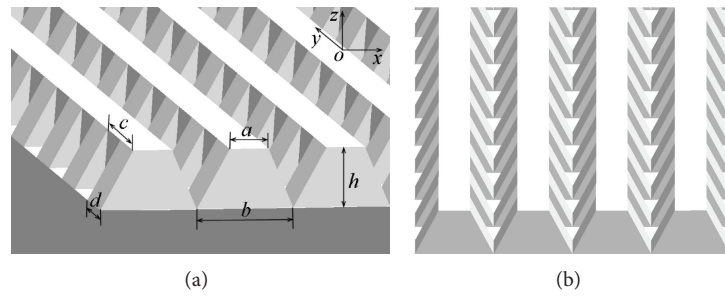


FIGURE 5: FDTD design of  $x$ -unspaced 2D periodic tapered-staggered gratings.

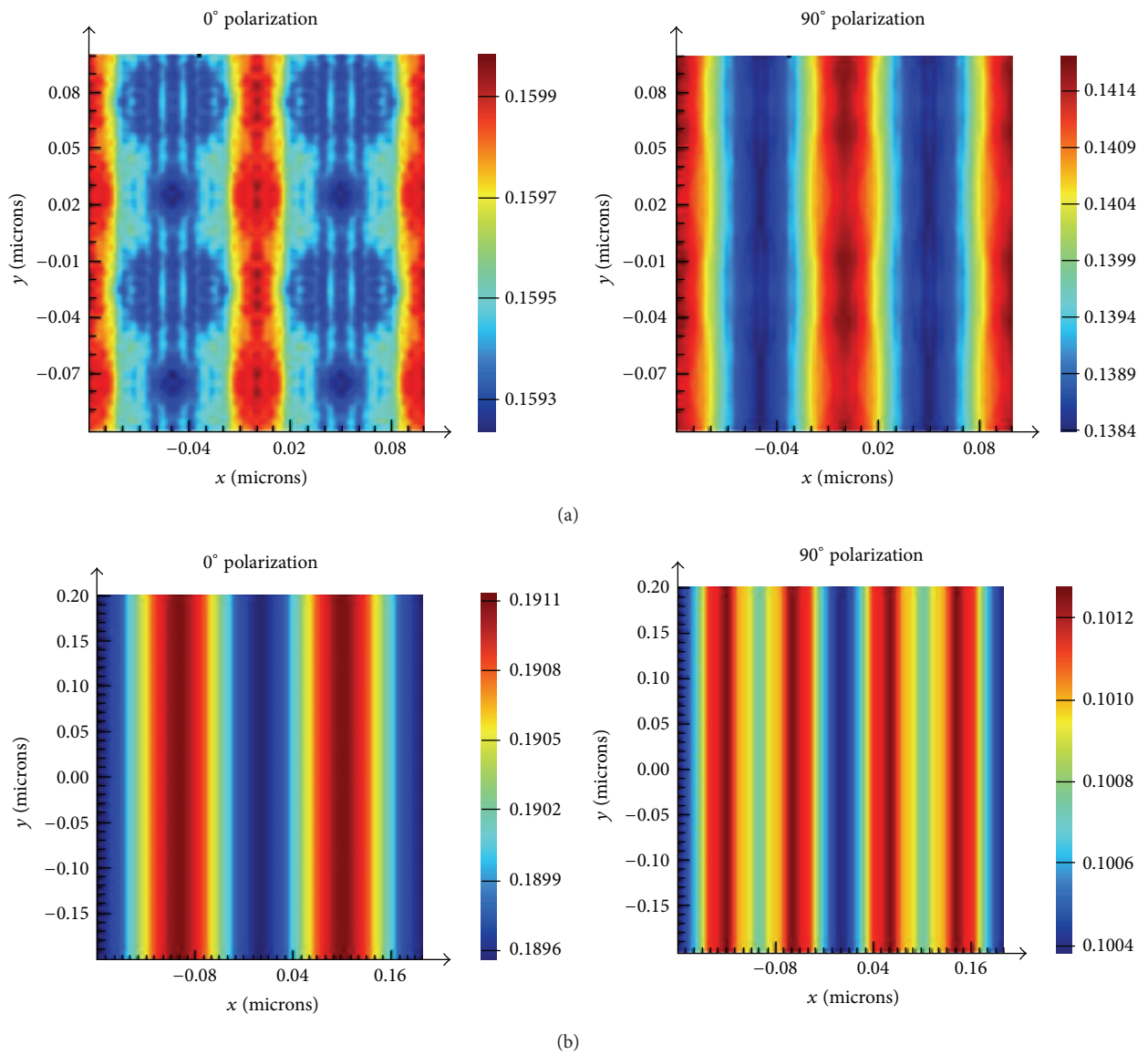


FIGURE 6: Calculated reflected electric intensity distributions for (a)  $x$ -unspaced 2D periodic tapered-staggered and (b) general right-angled Si gratings.

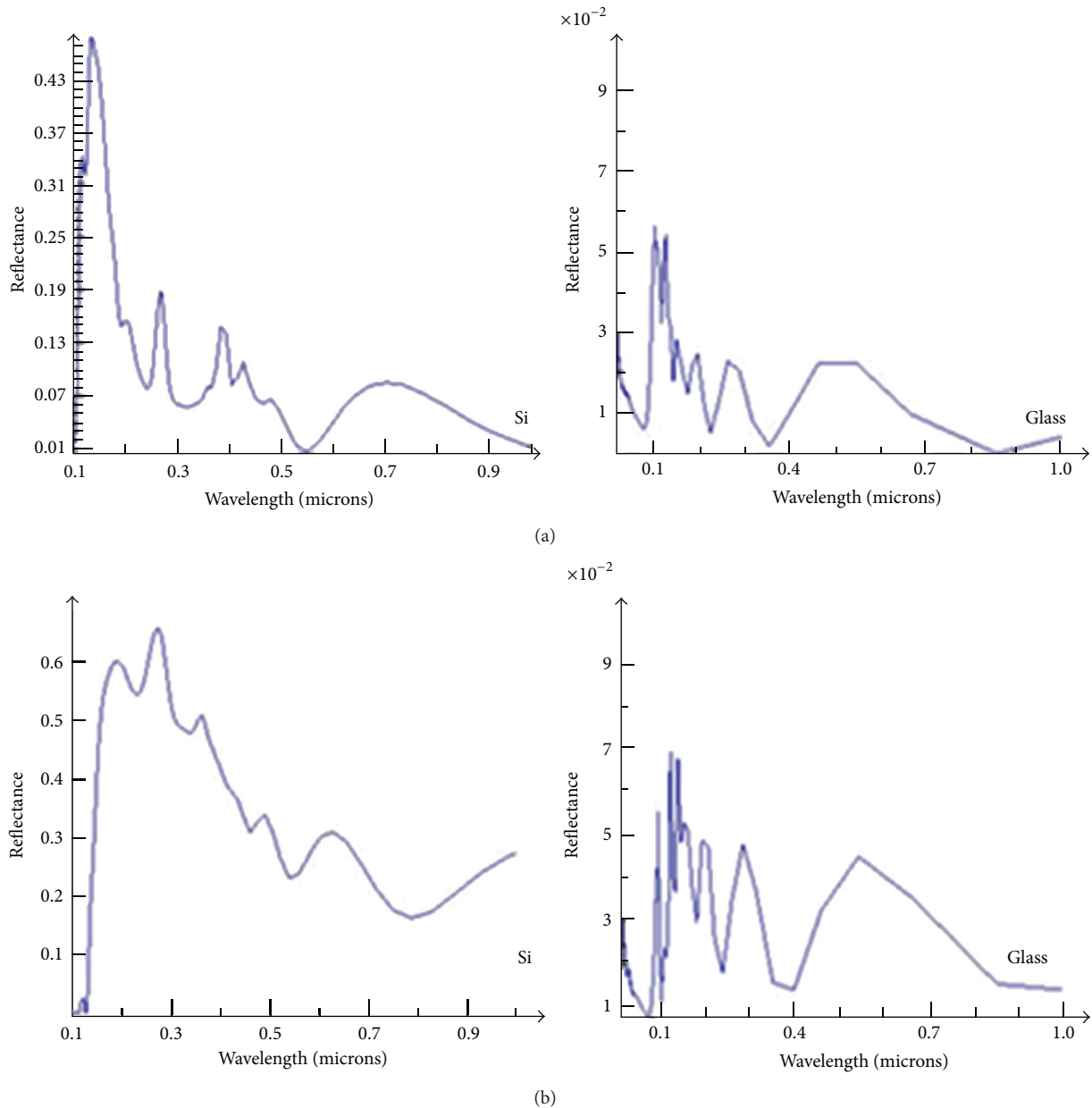


FIGURE 7: Calculated reflectance at various wavelengths for  $x$ -unspaced 2D periodic tapered-staggered gratings at (a)  $0^\circ$  and (b)  $90^\circ$  polarization.

designed gratings at different wavelengths and polarization angles was analyzed. It was shown that the 2D periodic tapered-staggered subwavelength gratings have different reflective performance from those of the general right-angled gratings. Moreover, the periodic subwavelength substructures along the ridges of the designed gratings may change the electric field intensity distribution (sensitive to light polarization) and weaken the surface reflection. Further, the performance of the designed  $\text{SiO}_2$  gratings is similar to that of the corresponding Si gratings, and the predicted reflectance can be less than around 5% for the bandwidth ranging from  $0.15 \mu\text{m}$  to  $1 \mu\text{m}$ . The antireflection performance

of the designed  $x$ -unspaced gratings is better than that of the corresponding  $x$ -spaced gratings. Based on the FDTD designs and simulated results, the butterfly-inspired 2D periodic tapered-staggered subwavelength grating structure was fabricated on the silicon substrate using FIB milling, reporting the possibility to fabricate these FDTD-designed grating structures.

### Conflict of Interests

The authors declare that there is no conflict of interests regarding the publication of this paper.

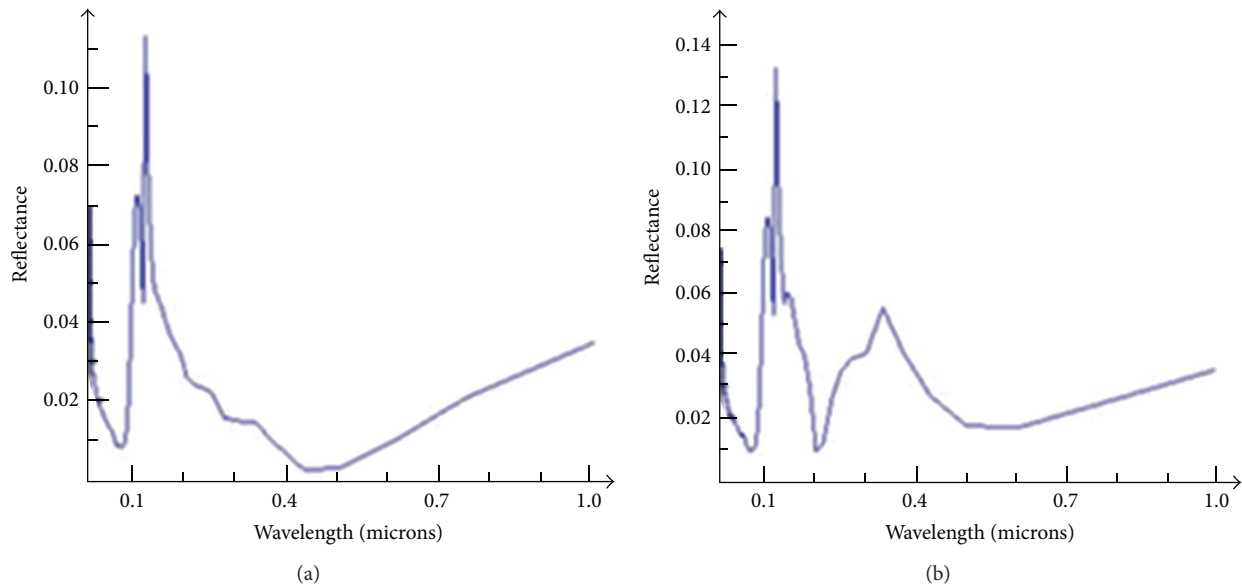


FIGURE 8: Calculated reflectance at various wavelengths for  $x$ -spaced 2D periodic tapered-staggered  $\text{SiO}_2$  gratings at (a)  $0^\circ$  and (b)  $90^\circ$  polarization.

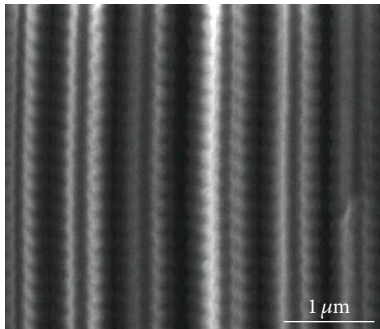


FIGURE 9: FIB-fabricated 2D periodic tapered-staggered subwavelength Si gratings measured using scanning electron microscope.

## Acknowledgments

The work is supported by the Research Foundation for Advanced Talents of Jiangsu University under Grant no. 14JDG020, China, and the A\*STAR (Agency for Science, Technology and Research) under SERC Grant no. 072 101 0023, Singapore.

## References

- [1] Y. Li, J. Zhang, and B. Yang, "Antireflective surfaces based on biomimetic nanopillared arrays," *Nano Today*, vol. 5, no. 2, pp. 117–127, 2010.
- [2] H. X. Wang, W. Zhou, and E. P. Li, "Focused ion beam nano-precision machining for analyzing photonic structures in butterfly," *Key Engineering Materials*, vol. 447–448, pp. 174–177, 2010.
- [3] Y. Hou, B. L. Abrams, P. C. K. Vesborg et al., "Bioinspired molecular co-catalysts bonded to a silicon photocathode for solar hydrogen evolution," *Nature Materials*, vol. 10, no. 6, pp. 434–438, 2011.
- [4] J.-W. Yoo, D. J. Irvine, D. E. Discher, and S. Mitragotri, "Bio-inspired, bioengineered and biomimetic drug delivery carriers," *Nature Reviews Drug Discovery*, vol. 10, no. 7, pp. 521–535, 2011.
- [5] D. Zhang, W. Zhang, J. Gu et al., "Bio-Inspired functional materials templated from nature materials," *KONA Powder and Particle Journal*, vol. 28, pp. 116–130, 2010.
- [6] K. Liu and L. Jiang, "Bio-inspired design of multiscale structures for function integration," *Nano Today*, vol. 6, no. 2, pp. 155–175, 2011.
- [7] Z. Guo, W. Liu, and B.-L. Su, "Superhydrophobic surfaces: from natural to biomimetic to functional," *Journal of Colloid and Interface Science*, vol. 353, no. 2, pp. 335–355, 2011.
- [8] F. Song, H. Su, J. Han, D. Zhang, and Z. Chen, "Fabrication and good ethanol sensing of biomorphic  $\text{SnO}_2$  with architecture hierarchy of butterfly wings," *Nanotechnology*, vol. 20, no. 49, Article ID 495502, 2009.
- [9] L. Jin, J. Zhai, L. Heng et al., "Bio-inspired multi-scale structures in dye-sensitized solar cell," *Journal of Photochemistry and Photobiology C: Photochemistry Reviews*, vol. 10, no. 4, pp. 149–158, 2009.
- [10] R. A. Potyrailo, H. Ghiradella, A. Vertiatchikh, K. Dovidenko, J. R. Cournoyer, and E. Olson, "Morpho butterfly wing scales demonstrate highly selective vapour response," *Nature Photonics*, vol. 1, no. 2, pp. 123–128, 2007.
- [11] R. Boruah, P. Nath, D. Mohanta, G. A. Ahmed, and A. Choudhury, "Photonic properties of butterfly wing infiltrated with Ag-nanoparticles," *Nanoscience and Nanotechnology Letters*, vol. 3, no. 4, pp. 458–462, 2011.
- [12] S. A. Boden and D. M. Bagnall, "Tunable reflection minima of nanostructured antireflective surfaces," *Applied Physics Letters*, vol. 93, no. 13, Article ID 133108, 2008.
- [13] Q. Chen, G. Hubbard, P. A. Shields et al., "Broadband moth-eye antireflection coatings fabricated by low-cost nanoimprinting," *Applied Physics Letters*, vol. 94, no. 26, Article ID 263118, 2009.

- [14] L. Yang, Q. Feng, B. Ng, X. Luo, and M. Hong, "Hybrid moth-eye structures for enhanced broadband antireflection characteristics," *Applied Physics Express*, vol. 3, no. 10, Article ID 102602, 2010.
- [15] C.-H. Sun, P. Jiang, and B. Jiang, "Broadband moth-eye antireflection coatings on silicon," *Applied Physics Letters*, vol. 92, no. 6, Article ID 061112, 2008.
- [16] W. L. Min, B. Jiang, and P. Jiang, "Bioinspired self-cleaning antireflection coatings," *Advanced Materials*, vol. 20, no. 20, pp. 3914–3918, 2008.
- [17] N. Yamada, T. Ijio, E. Okamoto, K. Hayashi, and H. Masuda, "Characterization of antireflection moth-eye film on crystalline silicon photovoltaic module," *Optics Express*, vol. 19, no. s2, pp. A118–A125, 2011.
- [18] S. A. Boden and D. M. Bagnall, "Sunrise to sunset optimization of thin film antireflective coatings for encapsulated, planar silicon solar cells," *Progress in Photovoltaics: Research and Applications*, vol. 17, no. 4, pp. 241–252, 2009.
- [19] Y. C. Chang, G. H. Mei, T. W. Chang, T. J. Wang, D. Z. Lin, and C. K. Lee, "Design and fabrication of a nanostructured surface combining antireflective and enhanced-hydrophobic effects," *Nanotechnology*, vol. 18, no. 28, Article ID 285303, 2007.
- [20] O. Sato, S. Kubo, and Z. Z. Gu, "Structural color films with lotus effects, superhydrophilicity, and tunable stop-bands," *Accounts of Chemical Research*, vol. 42, no. 1, pp. 1–10, 2009.
- [21] F. Liu, Y. Liu, L. Huang et al., "Replication of homologous optical and hydrophobic features by templating wings of butterflies *Morpho menelaus*," *Optics Communications*, vol. 284, no. 9, pp. 2376–2381, 2011.
- [22] D. Byun, J. Hong, Saputra et al., "Wetting characteristics of insect wing surfaces," *Journal of Bionic Engineering*, vol. 6, no. 1, pp. 63–70, 2009.
- [23] W. Zhang, D. Zhang, T. Fan et al., "Novel photoanode structure templated from butterfly wing scales," *Chemistry of Materials*, vol. 21, no. 1, pp. 33–40, 2009.
- [24] Q. Zhao, T. Fan, J. Ding, D. Zhang, Q. Guo, and M. Kamada, "Super black and ultrathin amorphous carbon film inspired by anti-reflection architecture in butterfly wing," *Carbon*, vol. 49, no. 3, pp. 877–883, 2011.
- [25] X. Yang, Z. Peng, H. Zuo, T. Shi, and G. Liao, "Using hierarchy architecture of *Morpho* butterfly scales for chemical sensing: experiment and modeling," *Sensors and Actuators A: Physical*, vol. 167, no. 2, pp. 367–373, 2011.
- [26] Y. Chen, J. Gu, S. Zhu, T. Fan, D. Zhang, and Q. Guo, "Iridescent large-area  $ZrO_2$  photonic crystals using butterfly as templates," *Applied Physics Letters*, vol. 94, no. 5, Article ID 053901, 2009.
- [27] J. Huang, X. Wang, and Z. L. Wang, "Controlled replication of butterfly wings for achieving tunable photonic properties," *Nano Letters*, vol. 6, no. 10, pp. 2325–2331, 2006.
- [28] W. Peng, X. Hu, and D. Zhang, "Bioinspired fabrication of magneto-optic hierarchical architecture by hydrothermal process from butterfly wing," *Journal of Magnetism and Magnetic Materials*, vol. 323, no. 15, pp. 2064–2069, 2011.
- [29] R. T. Lee and G. S. Smith, "Detailed electromagnetic simulation for the structural color of butterfly wings," *Applied Optics*, vol. 48, no. 21, pp. 4177–4190, 2009.
- [30] S. Kinoshita, S. Yoshioka, and J. Miyazaki, "Physics of structural colors," *Reports on Progress in Physics*, vol. 71, no. 7, Article ID 076401, 2008.

## Research Article

# Changes in Nanoscaled Mechanical and Rheological Properties of Asphalt Binders Caused by Aging

Ben Liu, Junan Shen, and Xuyan Song

Road Engineering Research Center, Suzhou University of Science and Technology, Suzhou 215011, China

Correspondence should be addressed to Junan Shen; shenjunan@hotmail.com

Received 28 January 2015; Accepted 30 March 2015

Academic Editor: Changhong Ke

Copyright © 2015 Ben Liu et al. This is an open access article distributed under the Creative Commons Attribution License, which permits unrestricted use, distribution, and reproduction in any medium, provided the original work is properly cited.

Aging of an asphalt binder causes the changes in the microstructure and, consequently, in the nanomechanical and rheological properties of the aged asphalt binder. Short-term aging on asphalt binders was simulated using rotating thin film oven (RTFO). These changes in the microstructure and nanomechanical and rheological properties were measured using atomic force microscope (AFM) and dynamic shear rheometer (DSR). The results indicated that (1) the adhesive force of the asphalt binder from AFM tests was increased after RTFO aging; (2)  $G'$  of the asphalt binder from DSR tests increased after RTFO aging; (3) the results from AFM were consistent with those from DSR, explaining the mechanism of the changes of rheological properties.

## 1. Introduction

Asphalt binder plays an important role in the performance of asphalt mixture, which accounted for 29% of rut depth at high temperature, according to the strategic highway research program (SHRP) research. Rheology is a very powerful tool for characterizing and quantifying materials properties. Since the rheological properties of asphalt change during production and continue to change subsequently in service, there is necessity to study the phenomenon of aging [1]. As a result of the global climate, air temperature of most areas in China in the summer is higher and higher and lasts for a long time, making the rutting and water damage particularly more prominent than ever before. The DSR is widely used for characterizing asphalt binders and is required for specifications in many countries. DSR can accurately measure the rheological responses of asphalt films adhesion to aggregate's surfaces [2]. As a special material, asphalt binder has viscoelastic property and is more complicated than other pavement materials. The testing involves using rotating thin film oven (RTFO) aged binders to mimic the state of binder aging in the mixture beams [3]. Because of its complexity in compositions, the rheological properties of asphalt binder are dependent on the aging, the temperature tested, and the test methods. A number of studies have recognized that binders of nearly

identical SHRP performance grades can show differences in fracture properties that vary significantly [4–6]. In order to understand the changes in nanoscale caused by the aging of short and long terms, the frontier of atomic force microscope (AFM) was used to explore the nanomechanical forces. The adhesion, nanoforce curve, and rheological properties were tested on an asphalt binder before and after aging through rotating thin film oven (RTFO) aging.

## 2. Materials and Methods

**2.1. Materials.** This research used Shell Pen 70# as asphalt. The properties of Pen asphalt were shown in Table 1.

It is indicated from Table 1 that the asphalt conformed to the requirements of the Chinese specifications.

In addition, the materials used for atomic force microscope test including acetone solution and carbon disulfide solution are all commercially available.

**2.2. Methods.** AFM analysis uses BRUKER company's icon type atomic force microscope. Its principle is that there is a small tip which is very sensitive to the weak force at the other end of micro-cantilever. Tip gently contacted the sample surface, due to the extremely weak repelling force between needle tip atoms and the sample surface atoms, the force will

TABLE 1: Properties of Shell Pen 70# asphalt.

| Test index                           | Unit   | Pen 70 | Specs | Test method |
|--------------------------------------|--------|--------|-------|-------------|
| Penetration (25°C, 5 s, 100 g)       | 0.1 mm | 68     | 60~80 | T0604       |
| Ductility (5 cm/min, 15°C)           | cm     | >100   | ≥100  | T0605       |
| Softening point (global method)      | °C     | 58     | ≥46   | T0606       |
| Dynamic viscosity (60°C)             | Pa·s   | 230    | ≥180  | T0625       |
| The residue after thin film oven     |        |        |       | T0609       |
| Quality loss                         | %      | 0.04   | ≤±0.8 | T0609       |
| Ductility (5 cm/min, 15°C)           | cm     | 27     | 15    | T0605       |
| Penetration ratio (25°C, 5 s, 100 g) | %      | 69     | ≥58   | T0604       |

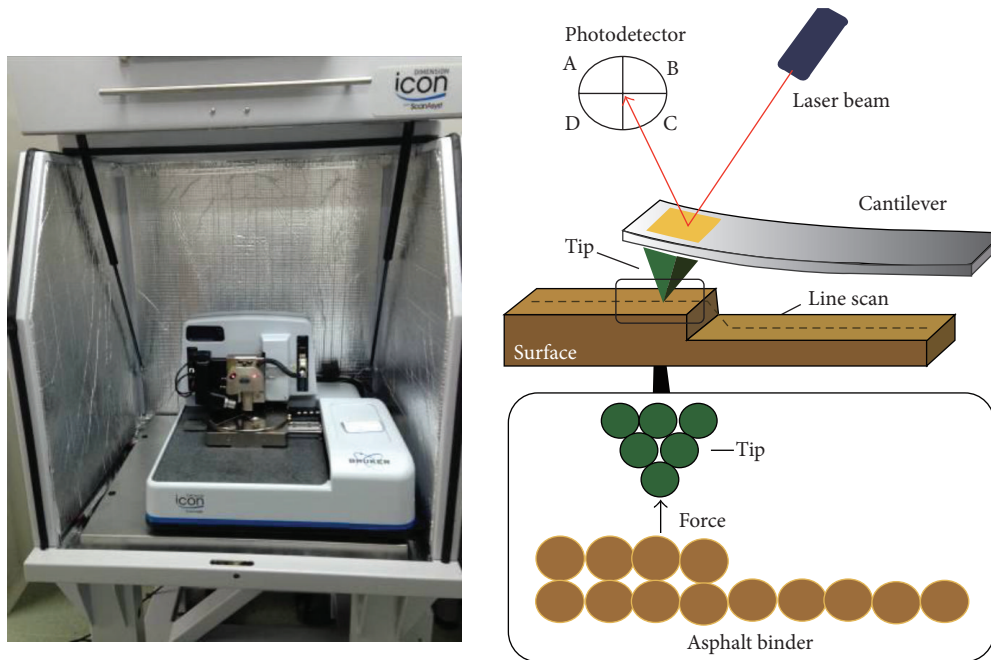


FIGURE 1: Atomic force microscope used in the study.

be kept constant in the scan control. A sharp tip probes the surface of a sample while collecting data. The cantilever tip is usually only several microns in length, and is located at the free end of a cantilever. Vertical displacement and lateral distortion in the cantilever is measured and mapped as the tip probes the surface of the specimen. The surface information will be measured by nanoscaled resolution. The operation mode of the atomic force microscope was classified in the form of acting force between tip and sample classification. There are mainly three kinds of operating modes: contact mode, noncontact mode, and tapping mode, with atomic force microscope structure model as shown in Figure 1.

The nanomechanical properties of the asphalt before and after aging are conducted by contact model. The probe model of the cantilever used in the study is SCANASYST—AIR, and its elasticity coefficient is 0.4 N/m. After correction, deflection sensitivity value of the cantilever beam is 51.48 nN/V, and the  $K$  of the spring coefficient is 0.4840 N/m.

This study followed the steps below [7]:

- (1) Weigh the asphalt before and after aging separately, with the weight ratio of carbon disulfide and asphalt 1:9.
- (2) Wipe completely glass slide with acetone solution to remove surface dust and make sure the slide surface is clean.
- (3) Absorb by glue rubber head a drop of the asphalt solution prepared and release it on a glass slide.
- (4) Let the drop of solution be a thin film.

Dynamic shear rheometer (DSR) is a machine that determines the rheological properties of asphalt binders for Superpave system: rutting resistance at high temperature and fatigue resistance at intermediate temperature. It belongs to the plate type rheometer. Asphalt samples were placed between parallel plates as shown in Figure 2, at a certain rate of rotating

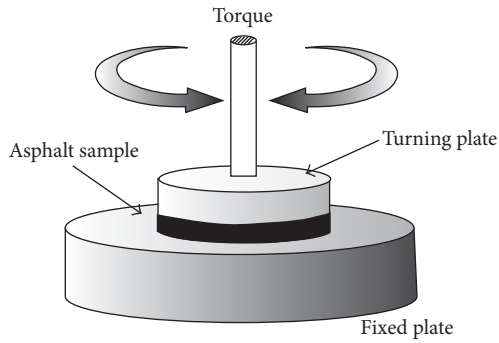


FIGURE 2: Asphalt sample loading way.

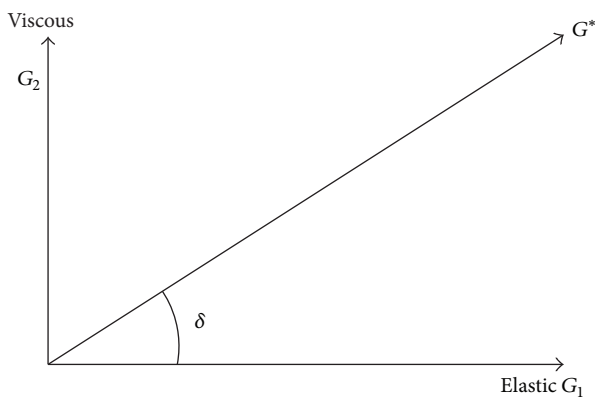


FIGURE 3: Viscoelastic complex modulus.

shearing, determining binder plural shear modulus  $G^*$  and phase angle of the  $\delta$ , charactering its viscoelastic properties.  $G^*$  is material repeated shear deformation measurement of total resistance, composed of elastic (recoverable) part of  $G_1$  and  $G_2$  of part of the viscosity (irreversible). The  $\delta$  is elastic and viscous deformation amount of relative index. The smaller the  $\delta$  is, the closer the material is in the elastomer, complex shear modulus ( $G^*$ ), and its two components: storage modulus ( $G_1$ ) and loss modulus ( $G_2$ ) [8], as shown in Figure 3.

### 3. Results and Discussion

**3.1. Nanoscaled Results from AFM.** Nanoscaled mechanical properties, that is, adhesion of asphalt binders before and after RTFO, were studied by using AFM. Nanoadhesion and nanoforce were measured, respectively [9]. AFM test probe of the elastic coefficient of cantilever beam is 0.4 N/m and correction of the cantilever beam of  $K$  value was 0.4840 N/m, with sweeping range of 20 microns  $\times$  20 microns. The results of the nanoadhesion and nanoforce of the asphalt before and after RTFO aging are shown in Figures 4–7, respectively.

Figures 4 and 5 are the results of nanoadhesion taken for asphalt before and after aging. These figures showed the nanoadhesion distribution on the area of asphalt of 20 microns  $\times$  20 microns. The darker the color, the smaller the adhesion. It is clear that the dark area was smaller and light

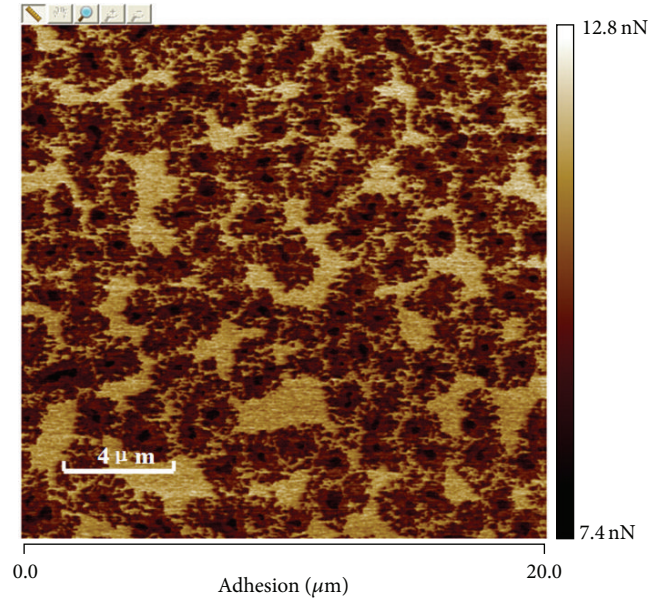


FIGURE 4: Nanoadhesion of asphalt.

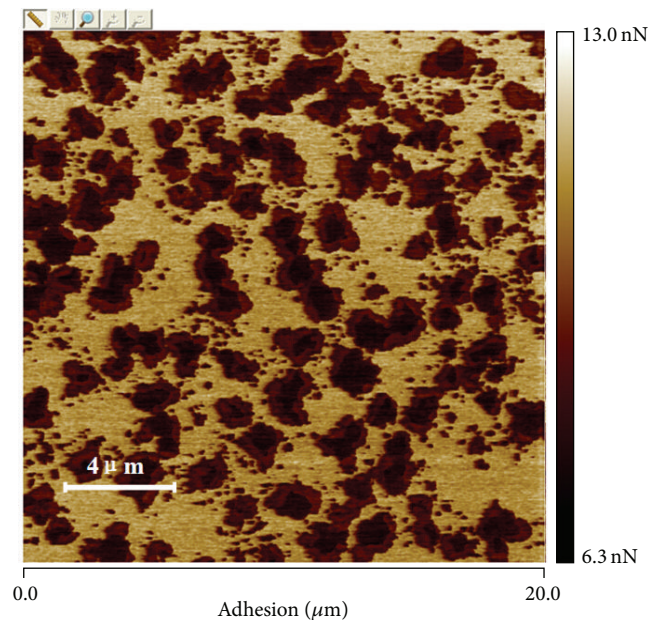


FIGURE 5: Nanoadhesion of RTFO residual.

color area was increased after RTFO aging, indicating that the whole area of adhesion was increased.

Figures 6 and 7 are the nanoforce curves of the binder before and after aging, a typical result taken from asphalt; both had the same trend. Here are the exploration and explanation for Figure 6. A nanoforce curve result can be divided into two parts—engagement part (curve A, abscissa from right to left), retraction part (curve B, abscissa from left to right). Curve A is characterization of the process that needle got closing to the sample, concave valley of curve A was caused by the van der Waals force (② part) between probe and sample molecules, it mainly showed the attraction force

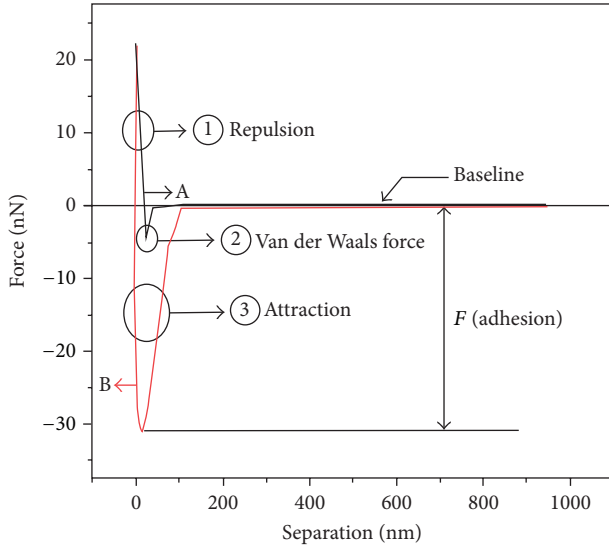


FIGURE 6: Nanoforce of asphalt.

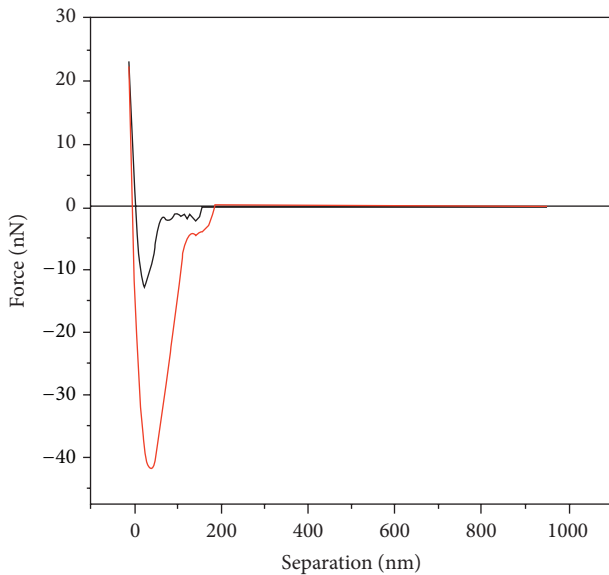
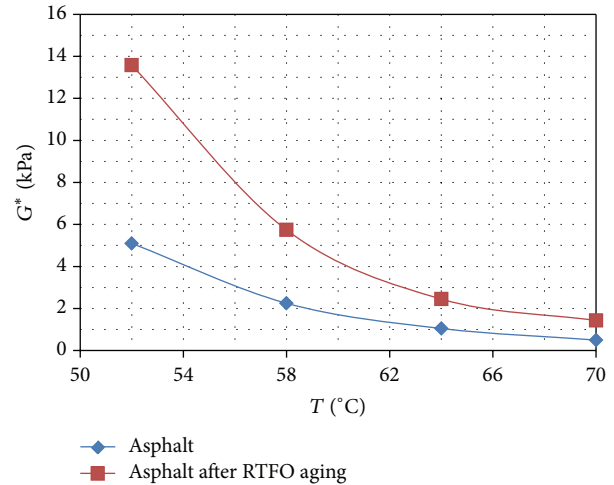


FIGURE 7: Nanoforce of asphalt RTFO residual.

at this time. As the probe kept getting close to the sample, the nanorepulsive force between tip and sample increased (①part represented repulsion part above the baseline). When the nanorepulsive force reached the maximum, the distance between the sample and probe became the closest, while the probe began to retract, that is, leaving the sample. Curve B in Figure 6 showed that the probe began to leave the sample (③part represented attraction part below the baseline). The adhesion of the sample can be reflected by the difference between the lowest point of retract part of the force curve (Curve B) and the baseline. The lowest point meant the largest attraction when the probe retracted out in the process of the sample of the binder sample. The point was often used to reflect the information of binding force of the asphalt binder sample. Work of adhesion is associated with the energy

TABLE 2: Adhesion force of different asphalt aging stage.

| Degree of aging | Adhesion force of asphalt (nN) |
|-----------------|--------------------------------|
| Original        | 30.7                           |
| RTFO residual   | 41.5                           |

FIGURE 8:  $G^*$ , temperature of asphalt before and after RTFO aging.

necessary to promote adherence. The behavior of the work of adhesion is similar to that observed for the adhesive force [10]. In principle, the value of separation cannot be negative, which was negative in some of Figures 4–7. The reason may be caused by the overloaded ramp force that can be solved by reducing the value of trigger threshold during the process of AFM experiment.

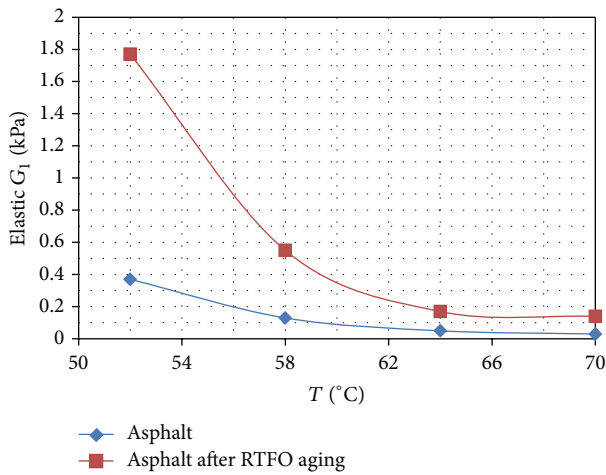
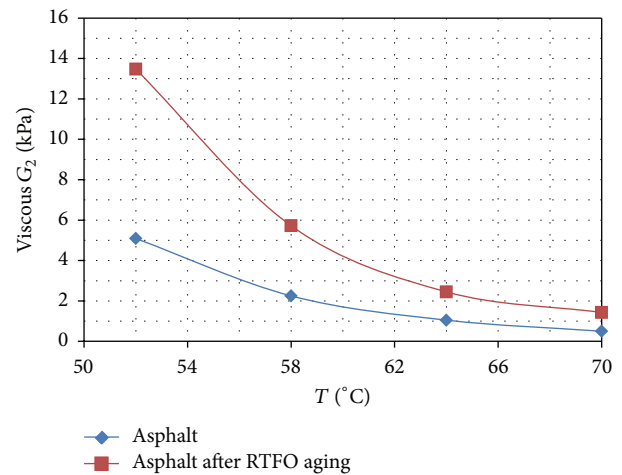
Figures 6 and 7 indicated that the adhesion can be reflected by retraction of nanoforce curve (i.e., the difference between the lowest part of the valley in the force curve B and the baseline). The point of valley means the largest attraction at the process of probe exiting samples. After that point, the probe can get rid of attraction and the force curve reaches the baseline. It can be seen from Table 2 that the adhesion values were 30.7 nN and 41.5 nN for asphalt and RTFO residuals, respectively. Adhesion force increased after RTFO aging.

**3.2. Rheological Results from DSR.** DSR measured rheological properties of asphalt before and after aging under temperatures from 52°C to 70°C, respectively, in accordance with the American AASHTOTP-93 requirements. DSR test results of asphalt are shown in Table 3. The relationship of different temperatures with  $G^*$ ,  $G_1$ ,  $G_2$ , and  $G^*/\sin(\delta)$  was shown in Figures 8, 9, 10, and 11, and respectively.

Figures 8, 9, 10, and 11 presented the complex shear modulus  $G^*$ , elastic modulus  $G_1$ , viscous modulus  $G_2$ , and  $G^*/\sin(\delta)$  of asphalt binders before and after RTFO aging. The greater the  $G^*/\sin(\delta)$ , a rutting factor, the better the asphalt material resistant to high temperature deformation. A higher  $G^*$  value indicates that the asphalt binder has higher stiffness to resist rutting, and low phase angle ( $\delta$ )

TABLE 3: Rheological properties of asphalt before and after RTFO tests.

| Test project               | Test temperature/°C | Asphalt | RTFO aged asphalt residual |
|----------------------------|---------------------|---------|----------------------------|
| $G^* / \sin(\delta)$ (KPa) | 52                  | 5.10    | 13.70                      |
|                            | 58                  | 2.25    | 5.77                       |
|                            | 64                  | 1.05    | 2.46                       |
|                            | 70                  | 0.50    | 1.44                       |
| Phase angle (°)            | 52                  | 85.8    | 82.5                       |
|                            | 58                  | 86.7    | 84.5                       |
|                            | 64                  | 87.2    | 86                         |
|                            | 70                  | 86.3    | 84.4                       |
| $G^*$ (KPa)                | 52                  | 5.10    | 13.58                      |
|                            | 58                  | 2.25    | 5.74                       |
|                            | 64                  | 1.05    | 2.45                       |
|                            | 70                  | 0.50    | 1.43                       |
| Elastic $G_1$ (KPa)        | 52                  | 0.37    | 1.77                       |
|                            | 58                  | 0.13    | 0.55                       |
|                            | 64                  | 0.05    | 0.17                       |
|                            | 70                  | 0.03    | 0.14                       |
| Viscous $G_2$ (KPa)        | 52                  | 5.09    | 13.47                      |
|                            | 58                  | 2.25    | 5.72                       |
|                            | 64                  | 1.05    | 2.45                       |
|                            | 70                  | 0.50    | 1.43                       |

FIGURE 9:  $G_1$ , temperature of asphalt before and after RTFO aging.FIGURE 10:  $G_2$ , temperature of asphalt before and after RTFO aging.

value ensures that the asphalt becomes more elastic to recover part of deformation [11]. Overall, the  $G^*$  decreased as the testing temperature increased for both the original and RTFO residual. Moreover,  $G^*$  of the asphalt after RTFO had a higher value than that of the original. However, the difference between the  $G^*$  of RTFO residual and that of the original one decreased as the temperature increased; see Figure 8. It can be concluded that RTFO aging had much more influence on the  $G^*$  when the temperature is low. The  $G_1$ ,  $G_2$ , and  $G^* / \sin(\delta)$  changed with the temperature in a similar way to that of  $G^*$ ; that is, the trend of the change of  $G^*$  with the temperature

is true for the other properties presented (see Figures 8–11 again).

Apparent changes in viscoelastic properties (e.g.,  $G^*$ ,  $G^* / \sin(\delta)$ ) with number of cycles of loading are used to define fatigue performance of asphalt binder. However, the mechanisms responsible for apparent changes in these viscoelastic properties were previously not well understood [12]; it is necessary to make further study of micromechanical mechanism of asphalt binders. Nano-adhesion of the asphalt binder from both the image figure and curve was higher for RTFO residual than the original one. This was consistent with the increase of  $G^*$  of the binder before and after RTFO aging.

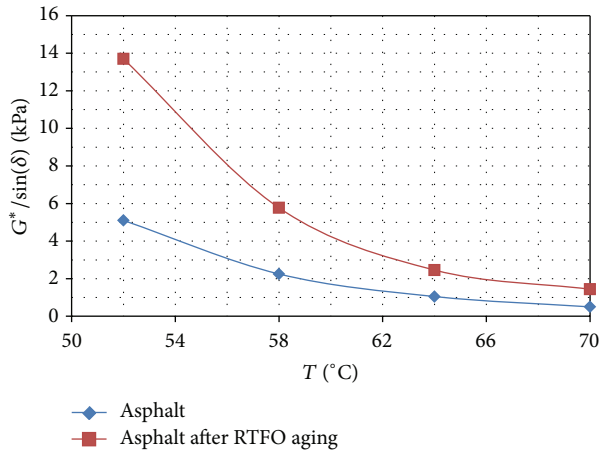


FIGURE 11:  $G^*/\sin(\delta)$ , temperature of asphalt before and after RTFO aging.

#### 4. Summary and Conclusions

In the study, the changes in nanomechanical properties were measured on base binder of both original and RTFO residuals using atomic force microscope (AFM), and the rheological properties were tested by dynamic shear rheometer (DSR). Conclusions can be drawn as follows:

- (1) The nanoadhesion was successfully measured from AFM of the picture and curve and it was found that it increased after RTFO aging for base binders. Nano-force curve from AFM showed that adhesion force is 30.7 nN and 41.5 nN for asphalt and RTFO residuals, respectively.
- (2)  $G^*$  of the binders was higher for RTFO residual than for the original one. The influence between the  $G^*$  of the RTFO residual and that of the original was temperature-dependent and decreased as the temperature increased.
- (3) The rheological properties of the asphalt changed consistently with the nanomechanical properties with the aging.
- (4) From the tests of AFM and RTFO, the results had a good correlation of base asphalt with the aging; SBS modified asphalt and other asphalt with different modifying agents should be tested in the future study to understand the aging mechanism of different asphalt better.

#### Conflict of Interests

The authors declare that there is no conflict of interests regarding the publication of this paper.

#### Acknowledgment

This research was supported financially by Chinese National Science Foundation with Grant no. 51378328.

#### References

- [1] C. Joshi, A. Patted, M. R. Archana, and M. S. Amarnath, "Determining the rheological properties of asphalt binder using dynamic shear rheometer (DSR) for selected pavement stretches," *International Journal of Research in Engineering and Technology*, no. 11, pp. 192–196, 2013.
- [2] D.-W. Cho and H. U. Bahia, "New parameter to evaluate moisture damage of asphalt-aggregate bond in using dynamic shear rheometer," *Journal of Materials in Civil Engineering*, vol. 22, no. 3, pp. 267–276, 2010.
- [3] C. M. Johnson, H. U. Bahia, and H. Wen, "Evaluation of strain-controlled asphalt binder fatigue testing in the dynamic shear rheometer," in *Proceedings of the 4th International SIIV Congress*, pp. 1–11, Palermo, Italy, 2007.
- [4] T. R. Hoare and S. A. M. Hesp, "Low-temperature fracture testing of asphalt binders," *Transportation Research Record*, vol. 1782, pp. 36–42, 2000.
- [5] D. A. Anderson, L. Lapalu, M. O. Marasteanu, Y. M. Le Hir, J.-P. Planche, and D. Martin, "Low-temperature thermal cracking of asphalt binders as ranked by strength and fracture properties," *Transportation Research Record*, vol. 1766, no. 1, pp. 1–6, 2001.
- [6] F. Olard and H. Di Benedetto, "Fracture toughness and fracture energy of bituminous binders at low temperature," in *Proceedings of the 5th International RILEM Conference on Reflective Cracking in Pavements*, vol. 37, pp. 359–366, Limoges, France, May 2004.
- [7] B. McCarron, X. Yu, and M. Tao, *The Investigation of "Be-Structures" in Asphalt Binders*, Department of Physics, Worcester Polytechnic Institute, 2011.
- [8] T. Khedaywi, G. Al-Khateeb, and M. Irfaeya, "Effect of medical ash on shear properties of asphalt binder using superpave dynamic shear rheometer (DSR)," *Journal of Solid Waste Technology and Management*, vol. 38, no. 1, pp. 19–27, 2012.
- [9] R. G. Allen, D. N. Little, and A. Bhasin, "Structural characterization of micromechanical properties in asphalt using atomic force microscopy," *Journal of Materials in Civil Engineering*, vol. 24, no. 10, pp. 1317–1327, 2012.
- [10] E. R. Dourado, R. A. Simao, and L. F. M. Leite, "Mechanical properties of asphalt binders evaluated by atomic force microscopy," *Journal of Microscopy*, vol. 245, no. 2, pp. 119–128, 2012.
- [11] G. G. Al-Khateeb and K. Z. Ramadan, "Investigation of the effect of rubber on rheological properties of asphalt binders using superpave DSR," *KSCE Journal of Civil Engineering*, vol. 19, no. 1, pp. 127–135, 2015.
- [12] C. Hintz and H. Bahia, "Understanding mechanisms leading to asphalt binder fatigue in the dynamic shear rheometer," *Road Materials and Pavement Design*, vol. 14, supplement 2, pp. 231–251, 2013.

## Research Article

# Size-Dependent Optical Properties of Nanoscale and Bulk Long Persistent Phosphor $\text{SrAl}_2\text{O}_4:\text{Eu}^{2+}$ , $\text{Dy}^{3+}$

Xiaoxia Duan,<sup>1</sup> Lixin Yi,<sup>2</sup> Xiqing Zhang,<sup>2</sup> and Shihua Huang<sup>2</sup>

<sup>1</sup>Department of Chemistry, School of Science, Beijing Jiaotong University, Beijing 100044, China

<sup>2</sup>Key Laboratory of Luminescence and Optical Information, Ministry of Education, Institute of Optoelectronic Technology, Beijing Jiaotong University, Beijing 100044, China

Correspondence should be addressed to Xiaoxia Duan; [xxduan@bjtu.edu.cn](mailto:xxduan@bjtu.edu.cn)

Received 27 December 2014; Revised 13 March 2015; Accepted 14 March 2015

Academic Editor: Yong Zhu

Copyright © 2015 Xiaoxia Duan et al. This is an open access article distributed under the Creative Commons Attribution License, which permits unrestricted use, distribution, and reproduction in any medium, provided the original work is properly cited.

Nanoscale long persistent phosphor  $\text{SrAl}_2\text{O}_4:\text{Eu}^{2+}$ ,  $\text{Dy}^{3+}$  was prepared by autocombustion of citrate gel. The energy level shift of activator  $\text{Eu}^{2+}$  and coactivator  $\text{Dy}^{3+}$  was analyzed according to the emission and the excitation spectra. The band gap change of  $\text{SrAl}_2\text{O}_4$  and the resulting trap depth change with particle size were discussed on the basis of analyzing the visible spectra, the vacuum ultraviolet (VUV) excitation spectra, and the thermoluminescence (TL) spectra. The fluorescence quenching and the shallow traps originating from surface adsorption or surface defects explain the weak initial persistent phosphorescence and the fast phosphorescence decay in nanometer  $\text{SrAl}_2\text{O}_4:\text{Eu}^{2+}$ ,  $\text{Dy}^{3+}$ . It is confirmed that energy level, band gap, trap depth, defect, and surface adsorption are deeply related with each other in this nanoscale long persistent phosphor.

## 1. Introduction

The theoretical model of long persistent phosphor is generally composed of three parts: matrix lattice, emitters, and traps [1], among which, emitters and traps are named as activator centers [2]. Emitters are centers capable of emitting radiation after being excited. Traps can be lattice defects originating from material itself or coactivator [2]. They usually do not emit radiation but store excitation energy and release it gradually to the emitters because of thermal or other physical stimulations. The trap energy level should be at a suitable position in forbidden band. Thus the emission wavelength of a persistent phosphor is mainly determined by the emission centers; the afterglow intensity and decay time are determined by the trap state (type and distribution) [1].

Long persistent phosphors have been rapidly developed in the past decades. Many of them have already been commercialized and are being widely used as night-vision materials in various important fields (e.g., security signs, emergency route signs, traffic signage, dials and displays, medical diagnostics, and optical probes in bioimaging) [3–11].

Among all the works, most researchers pay more attention to finding some new materials with long afterglow time

and stability. In fact, to improve the original properties and to study the persistent luminescence mechanisms are also very important [11–13]. Traps play very important role in long persistent phosphor. Trap depth is defined as the energy difference between the bottom of the conduction band and the trap energy level. The band gap of matrix lattice increases because of quantum confining effect when the particle size is minimized to nanometer, but the trap energy level is localized. So, theoretically the trap depth will increase. In view of this, it is predicted that the long afterglow properties will get better if the particle size is minimized to nanometer.

In this work, nanoscale and bulk long persistent phosphor were prepared. The size-dependent spectroscopy properties were studied systematically. This is very important for deeply exploring the persistent luminescence mechanism.

## 2. Experimental

Nanoscale and bulk  $\text{SrAl}_2\text{O}_4:\text{Eu}^{2+}$ ,  $\text{Dy}^{3+}$  were prepared, respectively, with the method described previously [14]. The solution was controlled at pH 7. The quantity of citric acid was denoted by formula  $n_{\text{CA}}/n_{\text{M}}^{n+} = 2$ , where  $n_{\text{CA}}$  is

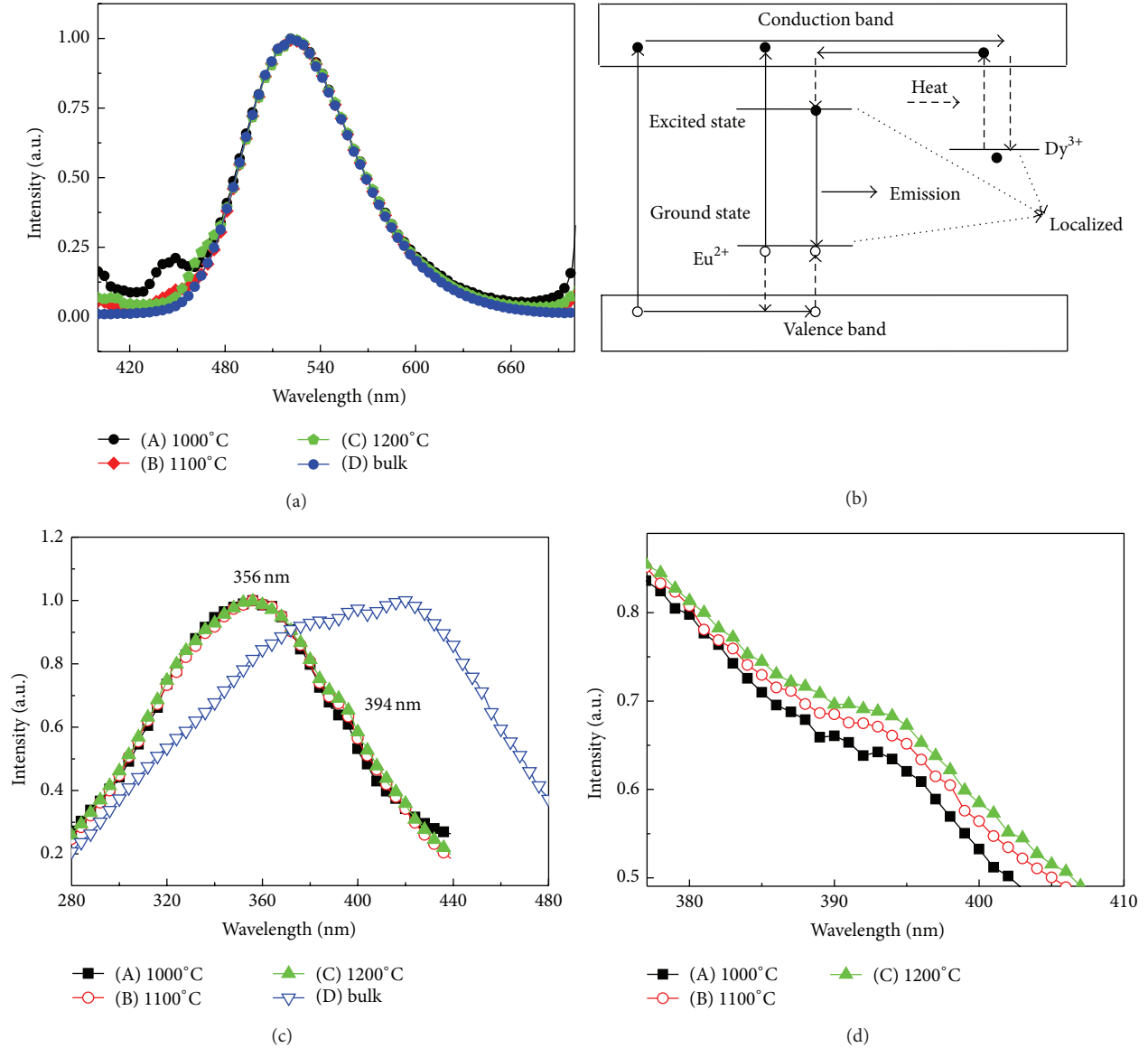


FIGURE 1: Emission spectra and excitation spectra. (a) Emission spectra of nanoscale and bulk SrAl<sub>2</sub>O<sub>4</sub>:Eu<sup>2+</sup>, Dy<sup>3+</sup>,  $\lambda_{\text{Ex}} = 360$  nm. (b) Afterglow mechanism of long persistent phosphor. (c) Excitation spectra of nanoscale and bulk SrAl<sub>2</sub>O<sub>4</sub>:Eu<sup>2+</sup>, Dy<sup>3+</sup>,  $\lambda_{\text{Em}} = 520$  nm. (d) The enlarged drawing of excitation spectra of nanoscale SrAl<sub>2</sub>O<sub>4</sub>:Eu<sup>2+</sup>, Dy<sup>3+</sup> in the vicinity of 394 nm,  $\lambda_{\text{Em}} = 520$  nm. (A), (B), and (C) correspond, respectively, to the nanomaterial prepared at 1000°C, 1100°C, and 1200°C and (D) corresponds to the bulk material. The particle size is  $R_A < R_B < R_C < R_D$ .

the mole number of citric acid and  $n_M^{n+}$  is the mole number of all the metal ion. The sintering temperature was separately set at 900°C, 1000°C, 1100°C, and 1200°C. The particle size of the obtained nanomaterial increases with the sintering temperature.

The emission spectra of the samples were measured by using INS-150-122B CCD spectrometer with a Xe lamp as light source. The excitation spectra were measured using a Flurolog-3 fluorescent spectrometer. The VUV excitation spectra were measured with a vacuum ultraviolet spectrometer. The TL glow curves of all the samples were carried out with FJ-4272 thermoluminescence instrument. The surface

adsorption was analyzed by using GX Fourier transform infrared (FTIR) spectrometer. The afterglow decay was analyzed by using Keithley 2410 and optical power meter. All the measurements were conducted at room temperature.

### 3. Results and Discussion

**3.1. Emission Spectra and Excitation Spectra.** Figure 1(a) shows the emission spectra of nanometer and bulk SrAl<sub>2</sub>O<sub>4</sub>:Eu<sup>2+</sup>, Dy<sup>3+</sup>. The exciting wavelength is 360 nm. (A), (B), and (C) refer, respectively, to nanometer material prepared at 1000°C, 1100°C, and 1200°C and (D) refers

to the bulk material. The particle size is listed as follows:  $R_A < R_B < R_C < R_D$ . The emission at 522 nm is attributed to  $4f^65d^1-4f^7$  transition of  $\text{Eu}^{2+}$ . The emission peaks of nanoscale  $\text{SrAl}_2\text{O}_4:\text{Eu}^{2+}$ ,  $\text{Dy}^{3+}$  are essentially coincident with that of the bulk phosphor. 5d electrons are exposed out of  $\text{Eu}^{2+}$ . Generally speaking, the energy level of rare earth ions is strongly localized. This is fit for activators ( $\text{Eu}^{2+}$ ) and traps ( $\text{Dy}^{3+}$ ) listed in Figure 1(b). The energy level difference between the lowest excited state  $4f^65d^1$  and the ground state  $4f^7$  does not change clearly when the particle size is reduced to nanometer scale, so the peak wavelength remains motionless.

The excitation spectra corresponding to the emission spectra in Figure 1(a) are shown in Figure 1(c). The detection wavelength was set at 520 nm. Compared to the emission spectra, the regularity of excitation spectra shows great difference. Firstly, the excitation spectra of the nanoparticles show obvious blue shift. Next, it can be seen in Figure 1(d) that the intensity value at 394 nm decreases with particle size decreasing. The emission intensity ratio ( $\beta_1 = I_{356\text{nm}}/I_{394\text{nm}}$ ) increases with particle size decreasing although the excitation spectra of nanoscale  $\text{SrAl}_2\text{O}_4:\text{Eu}^{2+}$ ,  $\text{Dy}^{3+}$  do not show obvious blue shift compared to the bigger nanoparticles. Besides, the luminous intensity of the nanoparticles inclines to decrease from 356 nm to 420 nm, but the bulk material inclines to increase in this range. All these three aspects indicate that the phosphor with the smaller size inclines to absorb the shorter wavelength irradiation.

From the above analysis, it can be concluded that the two luminescence related energy levels of  $\text{Eu}^{2+}$  in  $\text{SrAl}_2\text{O}_4:\text{Eu}^{2+}$ ,  $\text{Dy}^{3+}$  do not move clearly with particle size and crystal field has a greater influence on the higher excited state than on the lower excited state of emission center (activator here is  $\text{Eu}^{2+}$ ). In  $\text{SrAl}_2\text{O}_4:\text{Eu}^{2+}$ ,  $\text{Dy}^{3+}$ , the coactivator  $\text{Dy}^{3+}$  and the activator  $\text{Eu}^{2+}$  have similar electron shell structure and the trap level lies between the two luminescence related energy levels, so the trap level tends to lie in a relatively stable position. It can be deduced that the trap level provided by  $\text{Dy}^{3+}$  ions will not move up or down greatly with particle size decreasing (Figure 1(d)). This determines the trap level will be maintained at the original station when the particle size of  $\text{SrAl}_2\text{O}_4:\text{Eu}^{2+}$ ,  $\text{Dy}^{3+}$  decreases to nanometer scale.

**3.2. VUV Excitation Spectra and Band Gap.** Figure 2(a) shows the VUV excitation spectra of nanometer and bulk  $\text{SrAl}_2\text{O}_4:\text{Eu}^{2+}$ ,  $\text{Dy}^{3+}$ . Lines (A), (B), (C), and (D), respectively, refer to the nanometer samples prepared at 900°C, 1000°C, 1100°C, and 1200°C. Line (E) refers to the bulk material. The band gap of host crystal  $\text{SrAl}_2\text{O}_4$  is 6.52 eV, and the corresponding absorption edge should be at about 190 nm. It can be seen from Figure 2(a) that the band edges locate just near 190 nm. Here, the detection wavelength was set at 520 nm, which is the characteristic emission peak of  $\text{Eu}^{2+}$  ion. This means that the energy can be well transferred between the emission centers ( $\text{Eu}^{2+}$ ) and the host crystal ( $\text{SrAl}_2\text{O}_4$ ) [13, 15, 16]. The VUV excitation spectra actually reflect the light absorption of host crystal  $\text{SrAl}_2\text{O}_4$  when detecting 520 nm of emission.

For bulk semiconductor, the energy of the valence band and the conduction band distributes continuously. Band gap width is the distance between the valence band and the conduction band. For nanometer semiconductor, the energy of the valence band and the conduction band is no longer continuous and the band gap width increases when the particle size decreases (Figure 2(c)), which can be seen in Figure 2(b) (the enlarged picture of the band edge between 168 nm and 180 nm in Figure 2(a)). The VUV excitation spectra of the nanometer  $\text{SrAl}_2\text{O}_4:\text{Eu}^{2+}$ ,  $\text{Dy}^{3+}$  shift to the shorter wavelength compared to that of the bulk one. At the same time, the spectra of the nanoparticles shift to the shorter wavelength one by one with particle size decreasing from (B) to (E). Besides, there are two peaks at  $\lambda_1 = 168$  nm and  $\lambda_2 = 180$  nm in VUV excitation spectra. It is clear that the ratio  $\beta_2 = I_{168\text{nm}}/I_{180\text{nm}}$  gets bigger and bigger with particle size decreasing from (A) to (E). This novel phenomenon indicates that the shorter wavelength absorption plays more and more important role when the particle size decreases. Therefore, it can be concluded that nanoscale  $\text{SrAl}_2\text{O}_4$  should have wider band gap than the bulk one and the band gap inclines to increase with particle size decreasing.

**3.3. Thermoluminescence Spectra and Trap Depth.** According to the above analysis, the band gap of the nanoscale  $\text{SrAl}_2\text{O}_4$  is wider than that of the bulk one. In addition, it has been mentioned in Section 3.1 that the traps energy level provided by  $\text{Dy}^{3+}$  will not shift greatly with particle size decreasing. It can be deduced furtherly that the nanoscale  $\text{SrAl}_2\text{O}_4:\text{Eu}^{2+}$ ,  $\text{Dy}^{3+}$  has deeper traps than the bulk one. This is so-called quantum effect.

In order to find out what change has happened to the traps with particle size decreasing, TL spectra were measured after the samples were irradiated for 2 minutes by UV lamp (Figure 3). (A), (B), and (C), respectively, correspond to nanometer  $\text{SrAl}_2\text{O}_4:\text{Eu}^{2+}$ ,  $\text{Dy}^{3+}$  prepared at 900°C, 1000°C, and 1100°C and (D) corresponds to bulk  $\text{SrAl}_2\text{O}_4:\text{Eu}^{2+}$ ,  $\text{Dy}^{3+}$ . Each temperature peak in TL spectra corresponds to one kind of electron trap. Usually, the trap depth can be calculated according to Chen's equation [17] based on the peak temperature  $T_m$  and the shape of the TL curve. One has

$$E = \frac{c_\tau k T_m^2}{\tau} - b_\tau 2k T_m,$$

$$c_\tau = 1.51 + 3(\mu_g - 0.42),$$

$$b_\tau = 1.58 + 4.52(\mu_g - 0.42),$$

$$\tau = T_m - T_1,$$

$$\delta = T_2 - T_m,$$

$$\omega = T_2 - T_1,$$

$$\mu_g = \frac{\delta}{\omega},$$
(1)

where  $T_1$ ,  $T_m$ , and  $T_2$  represent the temperature of half intensity at low-temperature side, peak temperature, and temperature of half intensity at high-temperature side of TL peak,  $\tau$

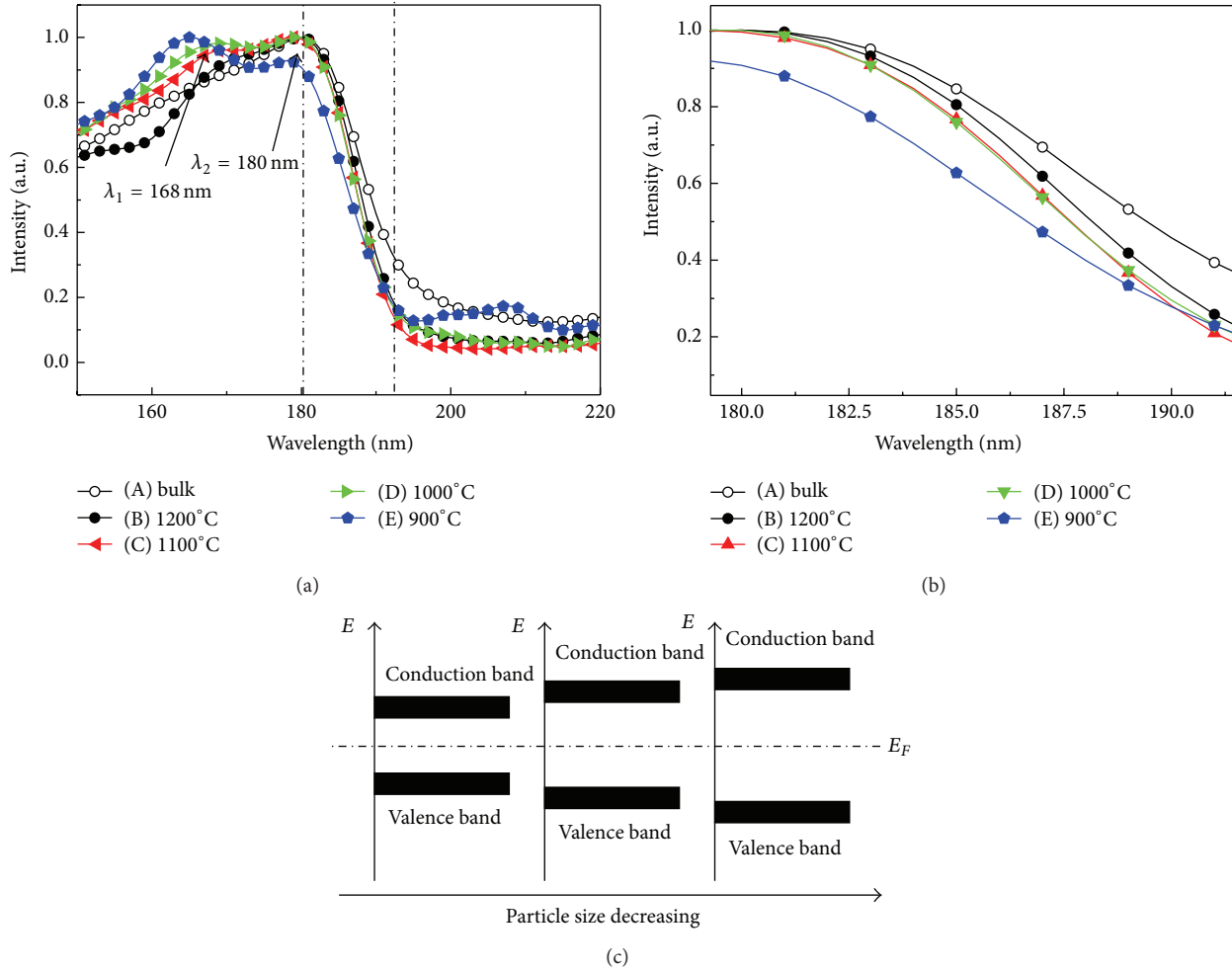


FIGURE 2: VUV excitation spectra and band gap. (a) VUV excitation spectra of nanoscale and bulk  $\text{SrAl}_2\text{O}_4:\text{Eu}^{2+}, \text{Dy}^{3+}$ ,  $\lambda_{\text{Em}} = 520$  nm. (b) Enlarged picture of VUV excitation spectra for nanoscale and bulk  $\text{SrAl}_2\text{O}_4:\text{Eu}^{2+}, \text{Dy}^{3+}$ ,  $\lambda_{\text{Em}} = 520$  nm. (c) Relationship between band gap and particle size of nanoscale semiconductor.

is the left half width,  $\delta$  is the right half width,  $\omega$  is the total half intensity width,  $k$  is Boltzmann's constant, and  $\mu_g$  is the symmetry factor.

As shown in Figure 3(a), curve (A) has only one weak peak at about 350 K, curve (B) or curve (D) has one strong asymmetric peak, and curve (C) has two peaks at 350 K and 400 K. But the above method has its own unavoidable drawbacks. It is only fit for individual peaks and is limited when the spectra overlap partially together. Here, the trap depths were estimated using equation  $E = T_m/500$  [17, 18].

It is clear that sample (A) has only one kind of shallow trap because it has only one weak TL peak at low temperature between 300 K and 350 K. Figures 3(b), 3(c), and 3(d) are the Gauss fitted results of curve (B), curve (C), and curve (D) in Figure 3(a). All the Gauss fitted peaks match very well with the original peaks. The peak at 350 K is considered originating from traps related with surface vacancy in nanoparticle. The 350 K peak intensity in line (B) is much stronger than that in line (A) because the luminescence quenching originated by

surface vacancy decreases with particle size increasing. The 375 K peak is considered originating from the traps deepened by quantum size effect of the surface vacancy. The peaks at 400 K in lines (C) and (D) are considered originating from the inner vacancy. Besides, the peak at the highest temperature 460 K must have something to do with  $\text{Dy}^{3+}$ .

It can be seen in Figures 3(c) and 3(d) that the higher temperature peak plays more and more important role with particle size increasing. This can be deduced from the peak area. According to Urbach model  $E = T_m/500$ , the trap depth at 350 K, 375 K, 400 K, and 460 K is, respectively, 0.70 eV, 0.75 eV, 0.80 eV, and 0.92 eV. In bulk material, the traps were provided by inner vacancy and  $\text{Dy}^{3+}$ . This is beyond all doubt. In nanoscale  $\text{SrAl}_2\text{O}_4:\text{Eu}^{2+}, \text{Dy}^{3+}$ , there should have been  $\text{Dy}^{3+}$  related peak at higher temperature according to the deduction at the beginning in Section 3.3. In fact, the electrons in this trap perhaps relax quickly to the surface state without giving emission. This supposed deep trap did not and will not appear in thermoluminescence spectra.

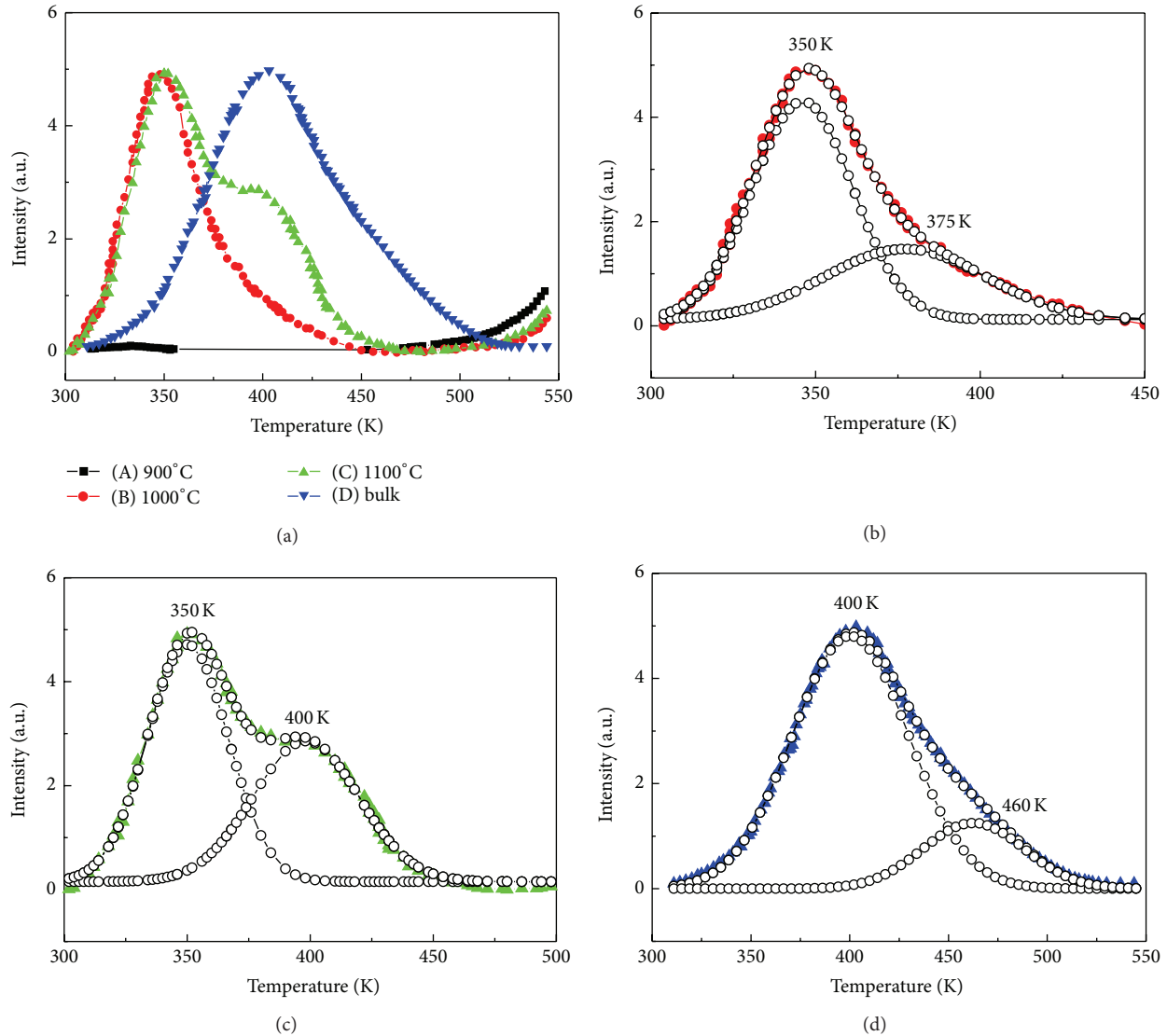


FIGURE 3: Size-dependent thermoluminescence spectra of  $\text{SrAl}_2\text{O}_4:\text{Eu}^{2+}, \text{Dy}^{2+}$  phosphors. (a) Thermoluminescence spectra of nanoscale  $\text{SrAl}_2\text{O}_4:\text{Eu}^{2+}, \text{Dy}^{2+}$  prepared by sol-gel method at 900°C (A), 1000°C (B), and 1100°C (C) and bulk phosphors (D) prepared by solid-state reaction method. (b) The Gauss fitted result of curve (B) in (a). (c) The Gauss fitted result of curve (C) in (a). (d) The Gauss fitted result of curve (D) in (a). The solid circles, up triangles, and down triangles correspond to the measured value and the open circles correspond to the Gauss fitted data.

**3.4. Surface Adsorption and Fluorescence Quenching [11].** Surface defects and surface adsorption are intrinsic and unavoidable in nanoscale materials. The surface adsorption was characterized with GX Fourier transform infrared spectrometer in order to confirm the relation between luminous intensity and surface state (Figure 4). There are many absorption peaks in the region of 400–900  $\text{cm}^{-1}$ , which are ascribed to the monoclinic crystal structure of  $\text{SrAl}_2\text{O}_4$ . No difference is found between all the samples in this region. This indicates that all the prepared samples have the same crystal structure and this determines all the above comparing is effective. The most interesting thing is all the samples display excellent regularity in the other wave number range. The absorption

peaks at 1632  $\text{cm}^{-1}$  are due to C=O; the peaks at 1340–1572  $\text{cm}^{-1}$  are due to the symmetric stretching vibration and the asymmetric stretching vibration of  $-\text{CO}_2^-$ . The absorption peaks at 3460  $\text{cm}^{-1}$  correspond to O-H bond adsorbed on the surface of nanoscale and bulk particles. It is very clear that the absorption intensity increases with particle size decreasing. This trend is consistent with surface effect of nanomaterials. In fact, all these adsorbed functional groups can also be regarded as special defects.

In general, the phonon energy originating from the interaction between the crystal field and luminescence center is very weak. The functional groups adsorbed on the surface are very light compared to rare earth ions. Their vibration

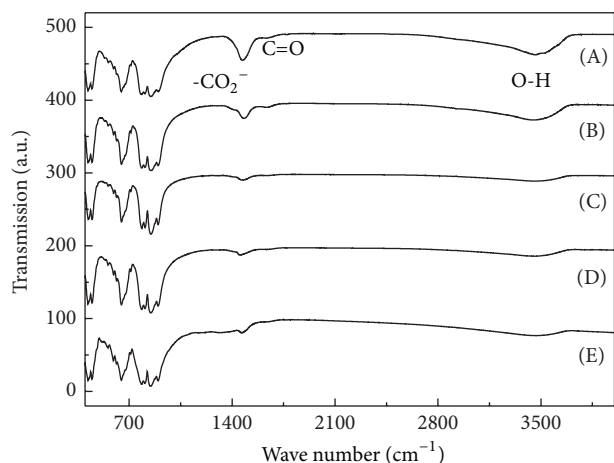


FIGURE 4: FTIR spectra of nanosized  $\text{SrAl}_2\text{O}_4:\text{Eu}^{2+}, \text{Dy}^{2+}$  phosphors prepared by sol-gel method at  $900^\circ\text{C}$  (A),  $1000^\circ\text{C}$  (B),  $1100^\circ\text{C}$  (C), and  $1200^\circ\text{C}$  (D) and bulk phosphors prepared by solid-state reaction method (E).

energy is very strong. The luminescent center near the surface couples with the vibration modes of those functional groups. The phonon energy provided by these vibration modes is relatively strong, so the electrons of luminescence center can easily relax to the lower energy level in nonradiative relaxation form and will not give out light. This process causes fluorescence quenching [19, 20] and this is just why the assumed deep traps did not work.

**3.5. Long Persistent Phosphorescence and Decay Curve.** According to the above analysis, deep traps play a leading role in bulk  $\text{SrAl}_2\text{O}_4:\text{Eu}^{2+}, \text{Dy}^{3+}$ . But for nanoscale  $\text{SrAl}_2\text{O}_4:\text{Eu}^{2+}, \text{Dy}^{3+}$ , the assumed deep traps originating from quantum size effect do not play their role due to the intrinsic surface defects and the unavoidable surface adsorptions. The electrons in the shallow traps are excited into the conduction band by thermal disturbance so easily that the long persistent luminescence decays quickly. Figure 5 is the luminous power versus time curve of nanoscale material prepared at  $1100^\circ\text{C}$  and the bulk material. The detected wavelength was set at the peak emission wavelength 520 nm. It is clear that the phosphorescence of nanoscale material decays much faster than that of the bulk one. In addition, the initial intensity of nanoscale long persistent phosphor is lower than that of the bulk phosphor and the final intensity of  $\text{SrAl}_2\text{O}_4:\text{Eu}^{2+}, \text{Dy}^{3+}$  tends to be much lower than that of the bulk  $\text{SrAl}_2\text{O}_4:\text{Eu}^{2+}, \text{Dy}^{3+}$ .

## 4. Conclusions

Nanoscale long persistent phosphors  $\text{SrAl}_2\text{O}_4:\text{Eu}^{2+}, \text{Dy}^{3+}$  with different size were prepared by autocombustion of citrate gelatin at  $900^\circ\text{C}$ ,  $1000^\circ\text{C}$ ,  $1100^\circ\text{C}$ , and  $1200^\circ\text{C}$ . The emission related energy levels of activator  $\text{Eu}^{2+}$  and the persistent luminescence related energy levels of coactivator  $\text{Dy}^{3+}$  do not change very clearly with particle size. The band gap of

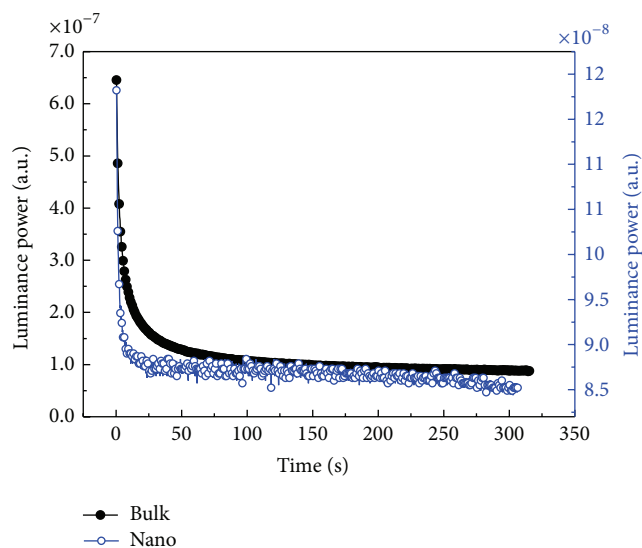


FIGURE 5: Decay curves at 520 nm emission peak of nanoscale (hollow circle) and bulk (solid circle)  $\text{SrAl}_2\text{O}_4:\text{Eu}^{2+}, \text{Dy}^{3+}$  phosphor. The right luminance power refers to nanoscale  $\text{SrAl}_2\text{O}_4:\text{Eu}^{2+}, \text{Dy}^{3+}$ , the left one refers to bulk  $\text{SrAl}_2\text{O}_4:\text{Eu}^{2+}, \text{Dy}^{3+}$ .

$\text{SrAl}_2\text{O}_4$  matrix crystal becomes wider and wider with particle size decreasing because of quantum effect. The smaller nanoparticles lead to the more serious surface adsorption and surface defects, which lead to nonradiative relaxation and fluorescence quenching. These factors are fatal for long persistent phosphor in nanoscale  $\text{SrAl}_2\text{O}_4:\text{Eu}^{2+}, \text{Dy}^{3+}$ . The deep traps originating from quantum size effect do not play their role because of surface effect. The shallow traps originating from surface defects give weak thermoluminescence or persistent phosphorescence. The afterglow of the nanoscale  $\text{SrAl}_2\text{O}_4:\text{Eu}^{2+}, \text{Dy}^{3+}$  decays faster than that of the bulk one.

## Conflict of Interests

The authors declare that there is no conflict of interests regarding the publication of this paper.

## Acknowledgments

The authors gratefully acknowledge the support from the Fundamental Research Funds for the Central Universities (no. 2013JBM099) and the National Natural Science Foundation of China (nos. 60977017 and 61275058).

## References

- [1] Z. W. Pan, Y. Y. Lu, and F. Liu, "Sunlight-activated long-persistent luminescence in the near-infrared from  $\text{Cr}^{3+}$ -doped zinc gallogermanates," *Nature Materials*, vol. 11, no. 1, pp. 58–63, 2012.
- [2] W. M. Yen, S. Shionoya, and H. Yamamoto, *Phosphor Handbook*, CRC Press, 2007.
- [3] Q. L. M. De Chermont, C. Chanéac, J. Seguin et al., "Nanoprobes with near-infrared persistent luminescence for *in vivo* imaging,"

- Proceedings of the National Academy of Sciences of the United States of America*, vol. 104, no. 22, pp. 9266–9271, 2007.
- [4] L. C. V. Rodrigues, H. F. Brito, J. Hölsä, and M. Lastusaari, “Persistent luminescence behavior of materials doped with  $\text{Eu}^{2+}$  and  $\text{Tb}^{3+}$ ,” *Optical Materials Express*, vol. 2, no. 4, pp. 382–390, 2012.
- [5] W. Zeng, Y. Wang, S. Han, W. Chen, G. Li, and Y. Wen, “Design, synthesis and characterization of a novel yellow long-persistent phosphor:  $\text{Ca}_2\text{BO}_3\text{Cl}:\text{Eu}^{2+}, \text{Dy}^{3+}$ ,” *Journal of Materials Chemistry C*, vol. 1, no. 17, pp. 3004–3011, 2013.
- [6] W. Chen and J. Zhang, “Using nanoparticles to enable simultaneous radiation and photodynamic therapies for cancer treatment,” *Journal of Nanoscience and Nanotechnology*, vol. 6, no. 4, pp. 1159–1166, 2006.
- [7] K. van den Eeckhout, P. F. Smet, and D. Poelman, “Persistent luminescence in  $\text{Eu}^{2+}$ -doped compounds: a review,” *Materials*, vol. 3, no. 4, pp. 2536–2566, 2010.
- [8] B.-Y. Wu, H.-F. Wang, J.-T. Chen, and X.-P. Yan, “Fluorescence resonance energy transfer inhibition assay for  $\alpha$ -fetoprotein excreted during cancer cell growth using functionalized persistent luminescence nanoparticles,” *Journal of the American Chemical Society*, vol. 133, no. 4, pp. 686–688, 2011.
- [9] A. Abdukayum, J. T. Chen, Q. Zhao et al., “Functional near infrared-emitting  $\text{Cr}^{3+}/\text{Pr}^{3+}$  Co-doped zinc gallogermanate persistent luminescent nanoparticles with superlong afterglow for in vivo targeted bioimaging,” *Journal of the American Society*, vol. 135, no. 38, pp. 14125–14133, 2013.
- [10] M. Hepel and C. J. Zhong, “Persistent luminescence nanoparticles for diagnostics and imaging,” in *Functional Nanoparticles for Bioanalysis, Nanomedicine, and Bioelectronic Devices*, vol. 2, pp. 1–25, American Chemical Society, Washington, DC, USA, 2012.
- [11] G. F. Ju, Y. H. Hu, L. Chen, X. Wang, and Z. Mu, “Recent progress in  $\text{Eu}^{2+}$ -activated phosphate persistent phosphors,” *Optical Materials*, vol. 36, no. 11, pp. 1920–1923, 2014.
- [12] H. F. Brito, J. Hölsä, T. Laamanen, M. Lastusaari, M. Malkamäki, and L. C. V. Rodrigues, “Persistent luminescence mechanisms: human imagination at work,” *Optical Materials Express*, vol. 2, no. 4, pp. 371–381, 2012.
- [13] J. Hassinen, J. Hölsä, J. Niittykoski et al., “UV-VUV spectroscopy of rare earth doped persistent luminescence materials,” *Optical Materials*, vol. 31, no. 12, pp. 1751–1754, 2009.
- [14] X. X. Duan, S. H. Huang, F. T. You, Z. Xu, F. Teng, and L. Yi, “Electrooptical characteristics of nanoscale and bulk long persistent phosphor  $\text{SrAl}_2\text{O}_4:\text{Eu}, \text{Dy}$ ,” *Journal of Experimental Nanoscience*, vol. 4, no. 2, pp. 169–176, 2009.
- [15] A. N. Belsky and J. C. Krupa, “Luminescence excitation mechanisms of rare earth doped phosphors in the VUV range,” *Displays*, vol. 19, no. 4, pp. 185–196, 1999.
- [16] M. Kamada, J. Murakami, and N. Ohno, “Excitation spectra of a long-persistent phosphor  $\text{SrAl}_2\text{O}_4:\text{Eu}, \text{Dy}$  in vacuum ultraviolet region,” *Journal of Luminescence*, vol. 87–89, pp. 1042–1044, 2000.
- [17] C. S. Shalgaonkar and A. V. Narlikar, “Review: a review of the recent methods for determining trap depth from glow curves,” *Journal of Materials Science*, vol. 7, no. 12, pp. 1465–1471, 1972.
- [18] R. Chen, Y. Hu, L. Chen, X. Wang, Y. Jin, and H. Wu, “Luminescent properties of a novel afterglow phosphor  $\text{Sr}_3\text{Al}_2\text{O}_5\text{Cl}_2:\text{Eu}^{2+}, \text{Ce}^{3+}$ ,” *Ceramics International*, vol. 40, no. 6, pp. 8229–8236, 2014.
- [19] S. H. Huang, F. T. You, and H. S. Peng, “Influence of surface on spectroscopic properties of rare earth ions in nanocrystals,” *Journal of Rare Earth*, vol. 25, no. 4, pp. 396–401, 2007.
- [20] S. S. Pitale, S. K. Sharma, R. N. Dubey, M. S. Qureshi, and M. M. Malik, “Thermoluminescence glow curve analysis of UV irradiated long persistence  $\text{CaS}:\text{Pr}^{3+}$  phosphor through computerized glow curve deconvolution technique,” *Nuclear Instruments and Methods in Physics Research, Section B: Beam Interactions with Materials and Atoms*, vol. 266, no. 9, pp. 2027–2034, 2008.

## Research Article

# Impact of NiO<sub>x</sub> Buffer Layers on the Dielectric Properties of BaTiO<sub>3</sub> Thin Films on Nickel Substrates Fabricated by Polymer Assisted Deposition

Hui Du,<sup>1</sup> Yang Li,<sup>1</sup> Wei Zheng Liang,<sup>1</sup> Yu Xuan Wang,<sup>1</sup> Min Gao,<sup>1</sup>  
Wen Huang,<sup>1</sup> Yin Zhang,<sup>1</sup> and Yuan Lin<sup>1,2</sup>

<sup>1</sup>State Key Laboratory of Electronic Thin Films and Integrated Devices, University of Electronic Science and Technology of China, Chengdu, Sichuan 610054, China

<sup>2</sup>Institute of Electronic and Information Engineering in Dongguan, University of Electronic Science and Technology of China, Dongguan, Guangdong 523808, China

Correspondence should be addressed to Yuan Lin; linyuan@uestc.edu.cn

Received 26 January 2015; Revised 23 May 2015; Accepted 28 May 2015

Academic Editor: Joydeep Dutta

Copyright © 2015 Hui Du et al. This is an open access article distributed under the Creative Commons Attribution License, which permits unrestricted use, distribution, and reproduction in any medium, provided the original work is properly cited.

Structural health monitoring with piezoelectric thin films integrated on structural metals shows great advantages for potential applications. However, the integration of piezoelectric thin films on structure metals is still challenged. In this paper, we report the piezoelectric barium titanate [BaTiO<sub>3</sub> (BTO)] thin films deposited on polycrystalline Ni substrates by the polymer assisted deposition (PAD) method using NiO<sub>x</sub> as the buffer layers. The NiO<sub>x</sub> buffer layers with different thicknesses were prepared by varying immersing time from 5 minutes to 4 hours in H<sub>2</sub>O<sub>2</sub> solution. The dielectric and leakage current properties of the thin films have been studied by general test systems. The BTO/Ni heterostructure with 2-hour immersing time exhibits better dielectric properties with a dielectric constant over 1500 and a 34.8% decrease of the dielectric loss compared to that with 5-minute immersing time. The results show that the leakage current density is strongly affected by the thickness of the NiO<sub>x</sub> buffer layer. The conduction mechanisms of the BTO/Ni heterostructure have been discussed according to the *J-V* characteristic curves.

## 1. Introduction

Nanomaterials, including nanodots, nanowires, nanothin films, and related composites, have been immensely investigated in the last few decades due to their wide potential applications [1–5]. Barium titanate [BaTiO<sub>3</sub> (BTO)] thin film, noted for its high dielectric constant and ferroelectric and piezoelectric properties, has aroused much attention for its potential applications in dynamic random access memories, optical modulators, waveguides, structural health monitoring (SHM), and microelectromechanical system (MEMS) [6–8]. With the increasing demands on embedded high density capacitors in the microelectronic packages and piezoelectric-based SHM, investigation on the fabrication of BTO thin films on base metallic substrates such as Ni or Cu has been initiated. Particularly, piezoelectric-thin-film-based built-in active SHM sensors with nondestructive evaluation abilities

have shown great advantages compared to the bulk ones due to their seamless atomic bond between the active sensor and the structure as well as their low voltage requirement [9]. However, major challenges exist in the fabrication of piezoelectric thin films on structural materials due to the difficulties in controlling the oxidation of the structural metallic substrates, the interdiffusion, and the crystallization of the oxide piezoelectric thin films. The growth of BTO thin films on noble metals such as Pt and Au coated Si substrates or metal-oxide substrates has been widely reported by using the techniques of pulsed laser deposition (PLD), sputtering, or chemical solution deposition (CSD) [10–13]. Nevertheless, only a few groups have initiated the efforts of how to fabricate BTO thin films on nickel foils using CSD and PLD methods [14–17].

In 2004, a chemical solution deposition technique named polymer assisted deposition (PAD) [18–20] was reported,

which has proved itself as a promising complementary film fabrication technique with the advantages of low cost, precursor solution stability, and process controllability [21]. We have demonstrated that BTO films could be directly deposited on nickel substrates by using the PAD technique [22–24]. Specifically,  $\text{NiO}_x$  layer must be formed on the Ni substrate by pretreating it in  $\text{H}_2\text{O}_2$  solution prior to the thin film deposition and the precursor wet films must be thermally treated in a reduced environment. On one hand,  $\text{NiO}_x$  layer serves as a buffer layer to improve the wettability of the substrates and prevent interdiffusion at the interface during annealing. On the other hand, the free energy of BTO ( $-1854$  kJ/mol, at 1100 K) is much lower than that of NiO ( $-315$  kJ/mol, at 1100 K) [25], and BTO has the ability to deprive oxygen from  $\text{NiO}_x$  layer. In other words,  $\text{NiO}_x$  buffer layer also serves as the oxygen source during the annealing process of the BTO films in a reduced environment, which would to some degree release the concern of oxygen vacancies in the as-prepared BTO films. Reasonable dielectric constant and dielectric loss can be achieved for the optimized as-prepared BTO thin films. Decreased leakage current densities have been observed in the films with the pretreated  $\text{NiO}_x$  layers compared to the reference sample. To get a deep understanding on the effect of  $\text{NiO}_x$  layer, a systematic study on the leakage mechanism in this specific structure is necessary.

## 2. Materials and Methods

Details for the preparation of BTO film on nickel substrate by PAD method have been reported in our previous work [22–24]. Firstly, nickel substrates whose thickness is 0.5 mm were polished to get a smooth and shiny surface. However, this kind of surface has a very poor wettability to the water-based precursor solutions used in PAD. Thus we immersed the nickel substrate into 10% hydrogen peroxide solution at  $50^\circ\text{C}$ , and the nickel on the surface was oxidized gradually. An oxide buffer layer  $\text{NiO}/\text{Ni}_2\text{O}_3$  was formed to improve its wettability. In this experiment, by varying the immersing time of the Ni substrates in the  $\text{H}_2\text{O}_2$  solution, different thicknesses of  $\text{NiO}_x$  buffer layers could be formed. We selected five different samples, and their immersing time in the  $\text{H}_2\text{O}_2$  solution was 5 min (as the reference sample), 30 min, 1 h, 2 h, and 4 h, respectively.

The precursor solutions containing  $\text{Ba}^{2+}$  and  $\text{Ti}^{4+}$  were prepared according to the literature reports [18, 19]. Technically,  $\text{Ba}^{2+}$  solution was made by adding barium nitrate to the water solution of ethylenediaminetetraacetic acid (EDTA) and polyethyleneimine (PEI, from Sigma-Aldrich, average  $M_n \approx 60,000$ ,  $M_w \approx 750,000$ ). The solution was then purified and concentrated in an Amicon filtration unit to yield a solution with  $\text{Ba}^{2+}$  ions. To prepare the  $\text{Ti}^{4+}$  solution, titanium chloride was slowly added to 30% peroxide solution, then the solution was added slowly to the mixture of EDTA and PEI solution, and finally the solution was purified and concentrated to get a solution containing  $\text{Ti}^{4+}$  ions. The concentrations of  $\text{Ba}^{2+}$  and  $\text{Ti}^{4+}$  in the solutions were 19.8 and 12.4 mg/mL, respectively, measured by Inductively

Coupled Plasma Optical Emission Spectrometer (ICP-OES). Figure 1(a) shows the pictures of the  $\text{Ba}^{2+}$  and  $\text{Ti}^{4+}$  solutions. The  $\text{Ba}^{2+}$  and  $\text{Ti}^{4+}$  solutions were then mixed in the molar ratio of 1:1 to yield a homogenous precursor solution for BTO.

The as-prepared solution was spin-coated on the pretreated nickel substrates with a spin rate of 3000 rpm for 30 seconds. The as-prepared samples were put into a furnace for heat treatment. The spin coating and thermal treatment process were repeated for 5 times. We treated the first layer of BTO thin films at  $800^\circ\text{C}$  to get distinct interface and the other layers at  $600^\circ\text{C}$  to avoid excessive thermal exposure of the nickel substrates. Then, the BTO thin films were annealed at  $800^\circ\text{C}$  in order to get fine crystallization. To avoid the oxidation of the Ni substrates, the whole thermal treatment process was performed in the flowing forming gas of 96%  $\text{N}_2$  and 4%  $\text{H}_2$  with a flow rate of 100 mL/min. After SEM detection, the final thickness of the BTO thin films is about 400 nm. Figure 1(b) schematically shows the heat treatment process.

The crystallinity of the films was first examined by the X-ray diffraction (XRD) technique. To measure the dielectric properties of the BTO thin films, Au electrodes with an area of  $20\ \mu\text{m} \times 20\ \mu\text{m}$  were deposited on the surfaces of BTO thin films by lithography and magnetron sputtering methods as the top electrodes. Dielectric properties of the samples were tested using an Agilent-4294A Precision LCR meter. Leakage currents were measured using an Agilent B2901A Precision Source/Measure Unit. Figure 2 shows the test sketch of BTO/Ni samples and dielectric property and leakage current test system. The applied voltage varied from  $-10$  V to 0 V and then from 0 V to  $+10$  V for the leakage current measurements.

## 3. Results and Discussion

XRD was performed using Cu K radiation to examine crystal structure of the BTO/Ni heterostructures. It is interesting to see that all the samples exhibit similar diffraction patterns. Typical results are shown in Figure 3 (only two samples with immersing time of 5 min and 4 h are shown here).

The characteristic peaks of polycrystalline nickel and pseudocubic BTO can be identified from the XRD pattern. Characteristic peaks of NiO and  $\text{Ni}_2\text{O}_3$  cannot be observed despite different immersing time of nickel substrates in  $\text{H}_2\text{O}_2$  solution (which refers to the oxidation time of nickel substrate). The results of XRD demonstrate that the BTO thin films have been successfully fabricated on polycrystalline nickel substrates without detectable nickel oxide phases.

Figures 4 and 5 show the dielectric constant and loss of these BTO/Ni heterostructures treated in  $\text{H}_2\text{O}_2$  solution with different immersing time. The measurements were executed at 100 kHz and room temperature. From these two figures, the dielectric constant and the dielectric loss with immersing time of 5 min, 30 min, 1 h, 2 h, and 4 h are, respectively, 1722, 1657, 1600, 1581, and 253 and 2.3%, 2.2%, 1.9%, 1.5%, and 0.3%. Both dielectric constant and dielectric loss reduce with the increase of immersing time. This is mainly because of

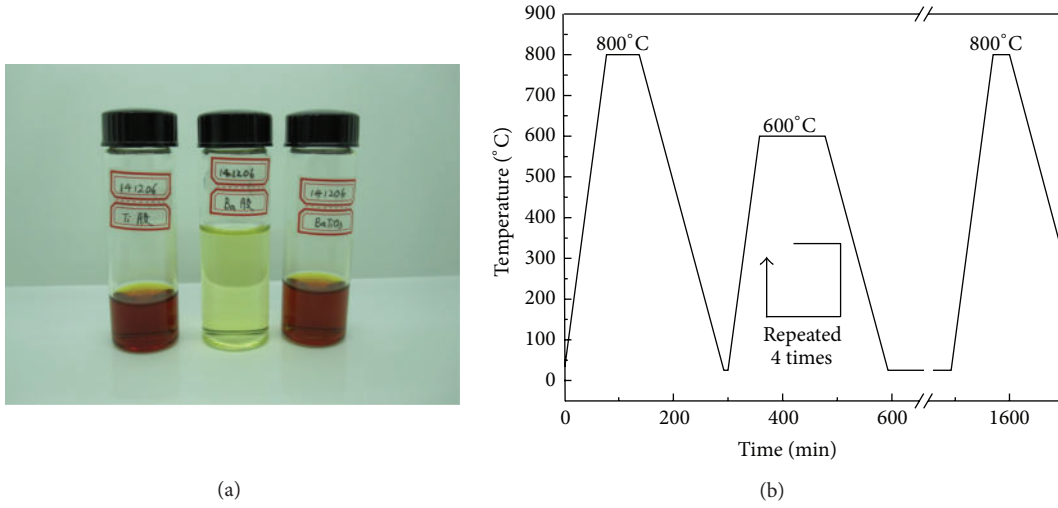


FIGURE 1: (a) Pictures of  $Ba^{2+}$  solution and  $Ti^{4+}$  solution. (b) Schematic of heat treatment process of BTO/Ni samples.

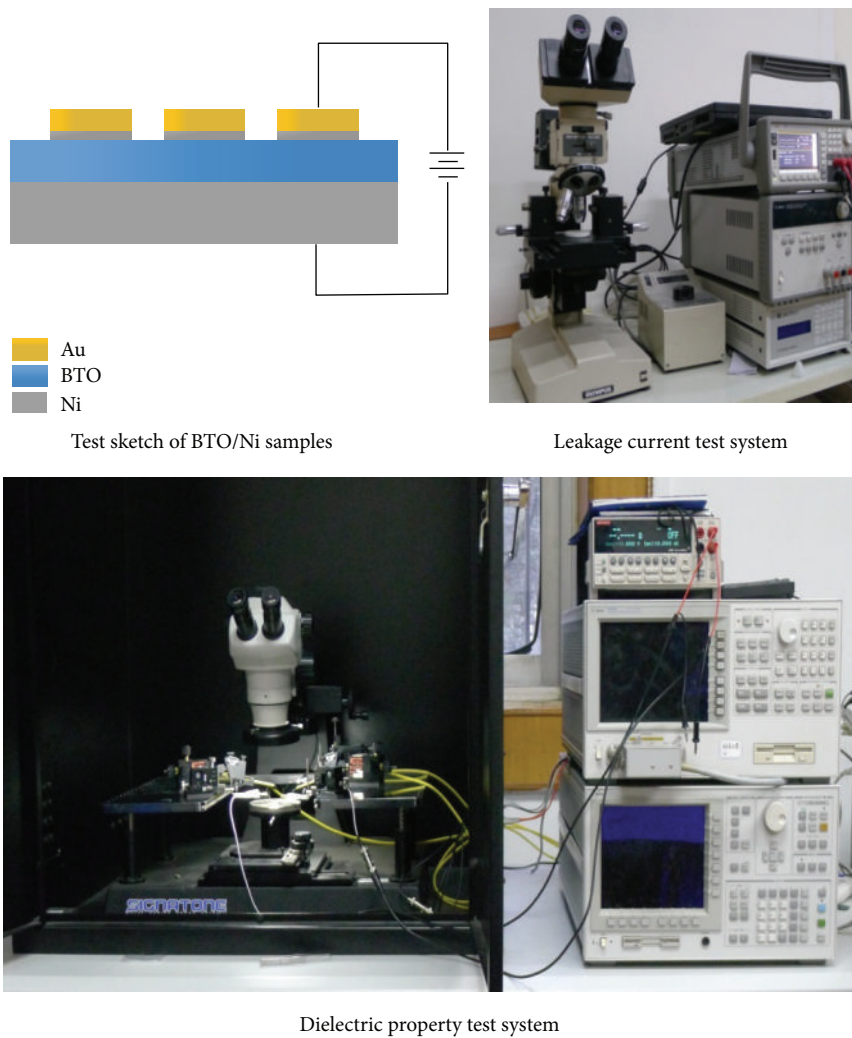


FIGURE 2: The test sketch of BTO/Ni samples and dielectric property and leakage current test system.

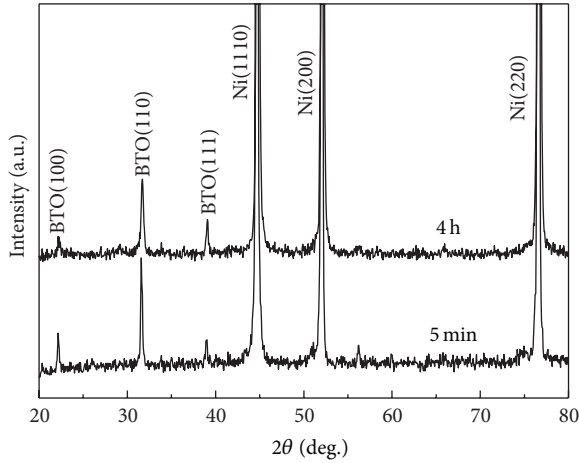


FIGURE 3: XRD patterns from  $\theta$ - $2\theta$  scans of BTO/Ni samples.

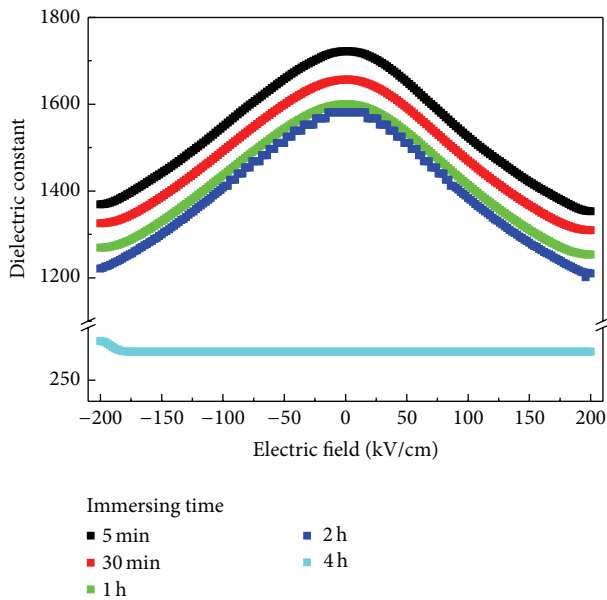


FIGURE 4: The dielectric constant characteristic curves of the BTO/Ni samples.

the influence of the nickel oxide buffer layers between the BTO thin films and the Ni substrates. The nickel oxide layer could block the interface diffusion between the Ni and the BTO layer and thus improve the quality of the BTO thin films and reduce the leakage current and dielectric loss. However,  $\text{NiO}_x$  layer has a much lower dielectric constant compared to the BTO layer, which implies that the heterostructure is actually a big capacitor of BTO in series with a small capacitor of  $\text{NiO}_x$ . Thus, the as-measured dielectric constant should be lower when  $\text{NiO}_x$  layer is thicker.

As can be seen from Figures 4 and 5, the balance should be considered when looking for the optimal pretreatment condition for the Ni substrates. For example, though the dielectric loss of the sample with 4 h immersing time decreases by 87% compared to the one with 5 min immersing time, the dielectric constant decreases by 85.3%. On the other hand,

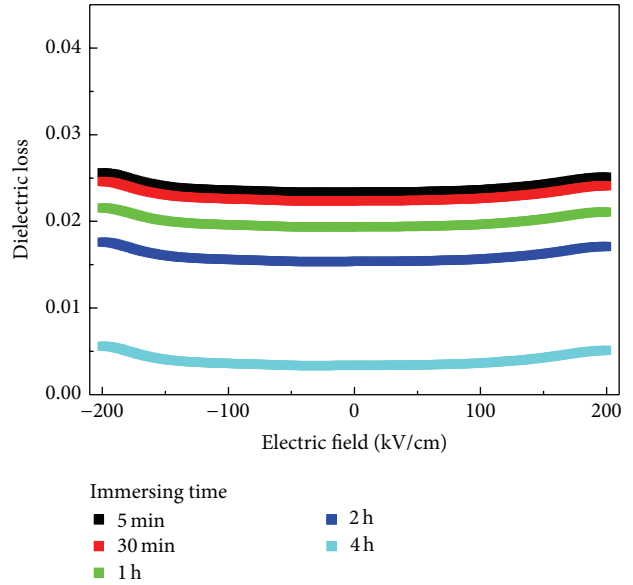


FIGURE 5: The dielectric loss characteristic curves of the BTO/Ni samples.

the dielectric constant of the sample with 2 h immersing time decreases only by 8.2%, whereas its dielectric loss reduced by 34.8% compared to the sample with 5 min immersing time. Therefore, 2 h immersing time might be an optimized condition for the applications which require low dielectric loss and high dielectric constant.

The Au electrode and the Ni substrate were regarded as positive and negative electrodes, respectively. In order to prevent the breakdown and obtain accurate leakage characteristic curve, the limit current and test delay time were set as  $100 \mu\text{A}$  and 0.1 s, respectively. All the scanning sequences began with 0 V. The leakage current density and electric field characteristic curves for the samples with different immersing time are shown in Figure 6.

From Figure 6, we can see that the  $J$ - $E$  characteristic curves are asymmetric under positive and negative bias voltage, which is mainly caused by the asymmetry of this kind of integrated structure. The leakage current conduction mechanism is then different when metal electrode is under positive and negative bias voltage. So it is necessary for us to analyze the leakage current conduction mechanism under positive and negative bias voltage, respectively. Whatever negative or positive bias voltage, leakage current decreases gradually along with the increase of immersing time. The sample with 4 h immersing time has a much lower leakage current density than the other 4 samples. This is mainly due to the increase of bulk resistance. As the oxidation time of nickel substrates increases, thickness of the nickel oxide layers increases. Since the films were thermally treated in a reduced ambient with the oxygen pressure of about  $10^{-18}$  atm, nickel oxide will decompose gradually during the heat treatment process [26, 27]. And as mentioned ahead, since the free energy of BTO is much lower than that of NiO, the oxygen from NiO would diffuse into the BTO layer to compensate oxygen vacancies. It is believed that the oxygen vacancies

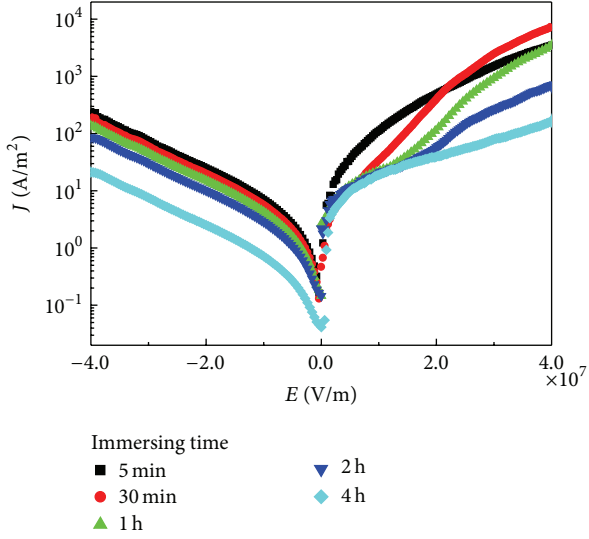


FIGURE 6:  $J$ - $E$  characteristic curves under positive and negative biases.

are the key factor contributing to the leakage current in ferroelectric oxide thin films. Thus, the sample with a thicker  $\text{NiO}_x$  layer should have a lower leakage current density.

The leakage current conduction mechanism under negative bias is analyzed by plotting  $\ln(J)$  versus  $E^{1/2}$ , as shown in Figure 7. It shows that all the curves fit well with the Schottky emission mechanism [28, 29], which can be expressed as

$$J = A^* T^2 \exp \left[ \frac{-e(\phi_0 - \sqrt{eE/4\pi\epsilon_i\epsilon_0})}{kT} \right], \quad (1)$$

where  $J$  is the current density,  $A^*$  is the Richardson constant,  $T$  is the absolute temperature,  $e$  is elementary charge,  $E$  is the applied electric field,  $\epsilon_i$  is the optical dielectric constant,  $\epsilon_0$  is the permittivity of free space,  $k$  is the Boltzmann constant, and  $e\phi_0$  is the Schottky barrier height.

The optical dielectric constant of the BTO samples is about 1.95, as calculated from the slopes of the curves in Figure 7. The value is at the same order of magnitude but smaller than the reported optical dielectric constant of about 5 for BTO bulk [30]. The reason may come from the different quality of our BTO thin film samples with the reported bulks. The absolute values of the intercept of the curves in Figure 6 reflect the Schottky barrier height. It is interesting to see that the Schottky barrier height increases with the thickness of  $\text{NiO}_x$  layer. The reason may lie in the suppression of interdiffusion between the BTO layer and the Ni substrate when the thickness of  $\text{NiO}_x$  layer increases, which would increase the Schottky barrier height.

From Figure 8, it is seen that, under the positive voltage, all the curves basely conform to a transition from the Ohmic conductive mechanism to the space-charge-limited-current (SCLC) mechanism [31].

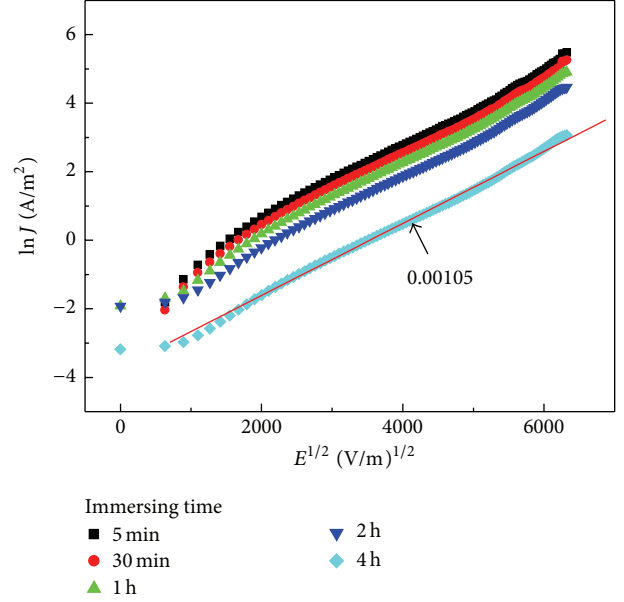


FIGURE 7:  $\ln(J)$  versus  $E^{1/2}$  plots under negative bias for the BTO/Ni samples.

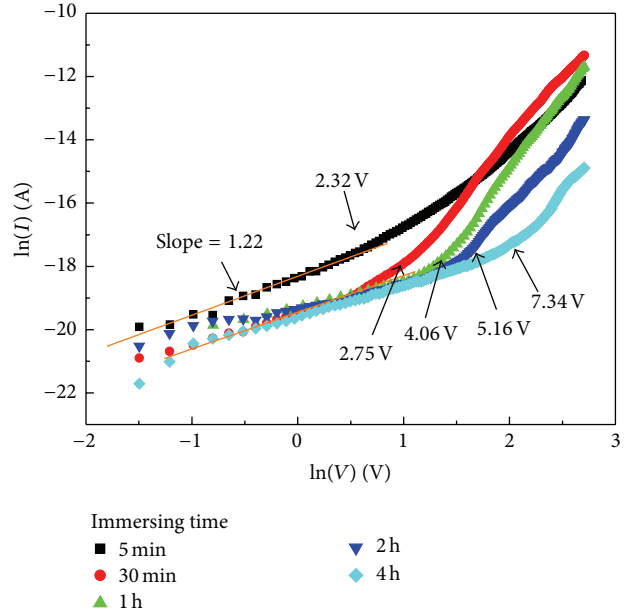


FIGURE 8:  $\ln(I)$  versus  $\ln(V)$  plots under positive bias for the BTO/Ni samples.

For the Ohmic conductive mechanism, the current density and the applied electric field follow a linear relationship. And the SCLC mechanism can be expressed as

$$J = \frac{9}{8} \epsilon_r \epsilon_0 \mu \frac{V^2}{L^3} = \frac{9}{8} \epsilon_r \epsilon_0 \mu \frac{E^2}{L}, \quad (2)$$

where  $\epsilon_r$  is the low frequency dielectric constant,  $\mu$  is the carrier mobility, and  $L$  is the thickness of the thin film.

Under positive bias, leakage currents of all samples follow Ohmic conductive mechanism when the voltage is low.

At some transition points, leakage currents increase sharply, and the voltages of these transition points, as shown in Figure 8, are 2.32 V, 2.75 V, 4.06 V, 5.16 V, and 7.34 V for the samples with the immersing time of 5 min, 30 min, 1 h, 2 h, and 4 h, respectively. In other words, the voltages at the transition point increase with the oxidation time of nickel substrates.

Two factors may account for the phenomenon that the longer the immersing time, the higher the voltage at the transition point. On one aspect, as mentioned above, the decomposition of nickel oxide layer would compensate the oxygen vacancies and thus reduce internal defects in the BTO layer. Since the oxygen vacancies are believed to be related to the origin of the space charges in many ferroelectric materials [32–35], the reduction of oxygen vacancies would increase the transition voltage from the Ohmic conductive mechanism to SCLC conductive mechanism. The second reason may lie in the voltage across the interfacial layer. Due to the compensation of the oxygen vacancies from the interfacial  $\text{NiO}_x$  layer, the distribution of oxygen vacancies in the BTO layer is not uniform. The area close to the BTO/Ni interface which has deprived oxygen from  $\text{NiO}_x$  buffer would have a higher resistance and the voltage across this area should be higher. The thicker the original  $\text{NiO}_x$  buffer is, the thicker the area in the BTO layer which can get enough compensation of oxygen vacancies is, and the higher the voltages would be applied on this area. Moreover, when the original  $\text{NiO}_x$  layer is thick enough, a residual  $\text{NiO}_x$  layer would be at the interface after the heat treatment, which would also share more voltage when its thickness increases. The higher partial voltage across the residual  $\text{NiO}_x$  layer and the interfacial BTO area would result in the increase of the voltage at the transition point.

It is interesting to note that, for the sample whose immersing time is 5 min, the slope of the curve at the high voltage part is not consistent with that of other samples. This suggests that the types of defects in this sample may be different from other samples. In the sample with 5 min immersing time, the interdiffusion between Ni and BTO is not well controlled and the oxygen vacancies in the BTO layer are not well compensated. The related defects would dominate the sources of space charge and lead to a typical SCLC conductive mechanism with the slope of  $\ln(J)$  versus  $\ln(V)$  close to 2. But when the thickness of  $\text{NiO}_x$  buffer layer increases and the interdiffusion and oxygen vacancies get a better control, other defects formed during the fabrication process would dominate the sources of space charge. Then the defect-related discrete energy levels appear in the forbidden band. The energy level influences carriers transport and conductive mechanism strongly and leads to a higher slope of  $\ln(J)$  versus  $\ln(V)$  plot.

#### 4. Conclusions

In summary, the barium titanate (BTO) thin films were successfully deposited on polycrystalline Ni substrates by the polymer assisted deposition (PAD) technique using  $\text{NiO}_x$  as the buffer layers. It is found that the dielectric properties and

the leakage current density of the BTO films are strongly affected by the thickness of  $\text{NiO}_x$  buffer layers which could be controlled by the pretreatment time. Obvious reduction in dielectric loss and leakage current densities has been observed in the samples with longer pretreatment time of Ni substrates. Combining with the analysis of leakage mechanisms in the BTO layers, the observed phenomena have been proposed to be related to the oxygen compensation and the suppression of interdiffusion at the interface.

#### Conflict of Interests

The authors declare that there is no conflict of interests regarding the publication of this paper.

#### Acknowledgments

This work is supported by the National Basic Research Program of China (973 Program) under Grant no. 2015CB351905, the National Natural Science Foundation of China (nos. 51372034, 11329402, and 51172036), and Guangdong Innovative Research Team Program (no. 201001D0104713329).

#### References

- [1] Y. Chen, W. Huang, and B. Peng, “Determination of optimal parameters for dual-layer cathode of polymer electrolyte fuel cell using computational intelligence-aided design,” *PLoS ONE*, vol. 9, no. 12, Article ID e114223, 2014.
- [2] Q. Zhang, B. Peng, D. Li, Y. Yang, and Y. Liu, “The effect of film microtexture and magnetic field on transparency of  $\text{Fe}_3\text{O}_4$ -PDMS nanocomposite films,” *IEEE Photonics Technology Letters*, vol. 26, no. 21, pp. 2181–2184, 2014.
- [3] M. Gao, Y. Pan, C. D. Zhang et al., “Tunable interfacial properties of epitaxial graphene on metal substrates,” *Applied Physics Letters*, vol. 96, no. 5, Article ID 053109, 2010.
- [4] B. Zeng, M. Gao, S. Liu, T. Pan, Z. Huang, and Y. Lin, “Thermal chemical vapor deposition of layered aligned carbon-nanotube films separated by graphite layers,” *Physica Status Solidi A: Applications and Materials Science*, vol. 210, no. 6, pp. 1128–1132, 2013.
- [5] T. X. Nan, H. Z. Zeng, W. Z. Liang et al., “Growth behavior and photoluminescence properties of ZnO nanowires on gold nanoparticle coated Si surfaces,” *Journal of Crystal Growth*, vol. 340, no. 1, pp. 83–86, 2012.
- [6] F. W. Van Keuls, R. R. Romanofsky, D. Y. Bohman et al., “ $(\text{YBa}_2\text{Cu}_3\text{O}_{7-\delta}, \text{Au})/\text{SrTiO}_3/\text{LaAlO}_3$  thin film conductor/ferroelectric coupled microstripline phase shifters for phased array applications,” *Applied Physics Letters*, vol. 71, no. 21, pp. 3075–3077, 1997.
- [7] D. L. Polla and L. F. Francis, “Processing and characterization of piezoelectric materials and integration into microelectromechanical systems,” *Annual Review of Materials Science*, vol. 28, no. 1, pp. 563–597, 1998.
- [8] P. Muralt, “Ferroelectric thin films for micro-sensors and actuators: a review,” *Journal of Micromechanics and Microengineering*, vol. 10, no. 2, pp. 136–146, 2000.
- [9] B. Lin, *Power and energy transduction in piezoelectric wafer active sensors for structural health monitoring: modeling and application* [Ph.D. thesis], University of South Carolina, Columbia, SC, USA, 2010.

- [10] S. M. Aygün, P. Daniels, W. Borland, and J.-P. Maria, "Hot sputtering of barium strontium titanate on nickel foils," *Journal of Applied Physics*, vol. 103, no. 8, Article ID 084123, 2008.
- [11] S. Kim, S. Hishita, Y. M. Kang, and S. Baik, "Structural characterization of epitaxial BaTiO<sub>3</sub> thin films grown by sputter-deposition on MgO(100)," *Journal of Applied Physics*, vol. 78, no. 9, pp. 5604–5608, 1995.
- [12] M. J. Burch, J. Li, D. T. Harris, J.-P. Maria, and E. C. Dickey, "Mechanisms for microstructure enhancement in flux-assisted growth of barium titanate on sapphire," *Journal of Materials Research*, vol. 29, no. 7, pp. 843–848, 2014.
- [13] C. L. Jia, K. Urban, S. Hoffmann, and R. Waser, "Microstructure of columnar-grained SrTiO<sub>3</sub> and BaTiO<sub>3</sub> thin films prepared by chemical solution deposition," *Journal of Materials Research*, vol. 13, no. 8, pp. 2206–2217, 1998.
- [14] Z. Yuan, J. Liu, J. Weaver et al., "Ferroelectric BaTiO<sub>3</sub> thin films on Ni metal tapes using NiO as buffer layer," *Applied Physics Letters*, vol. 90, no. 20, Article ID 202901, 3 pages, 2007.
- [15] J. T. Dawley and P. G. Clem, "Dielectric properties of random and [100] oriented SrTiO<sub>3</sub> and (Ba,Sr)TiO<sub>3</sub> thin films fabricated on [100] nickel tapes," *Applied Physics Letters*, vol. 81, no. 16, pp. 3028–3030, 2002.
- [16] T. Dechakupt, G. Y. Yang, C. A. Randall, S. Trolier-McKinstry, and I. M. Reaney, "Chemical solution-deposited BaTiO<sub>3</sub> thin films on Ni foils: microstructure and interfaces," *Journal of the American Ceramic Society*, vol. 91, no. 6, pp. 1845–1850, 2008.
- [17] J. Shin, A. Goyal, S. Jesse, and D. H. Kim, "Single-crystal-like, c-axis oriented BaTiO<sub>3</sub> thin films with high-performance on flexible metal templates for ferroelectric applications," *Applied Physics Letters*, vol. 94, no. 25, Article ID 252903, 2009.
- [18] Q. X. Jia, T. M. McCleskey, A. K. Burrell et al., "Polymer-assisted deposition of metal-oxide films," *Nature Materials*, vol. 3, no. 8, pp. 529–532, 2004.
- [19] Y. Lin, J.-S. Lee, H. Wang et al., "Structural and dielectric properties of epitaxial Ba<sub>1-x</sub>Sr<sub>x</sub>TiO<sub>3</sub> films grown on LaAlO<sub>3</sub> substrates by polymer-assisted deposition," *Applied Physics Letters*, vol. 85, no. 21, pp. 5007–5009, 2004.
- [20] Y. Lin, H. Wang, M. E. Hawley et al., "Epitaxial growth of Eu<sub>2</sub>O<sub>3</sub> thin films on LaAlO<sub>3</sub> substrates by polymer-assisted deposition," *Applied Physics Letters*, vol. 85, no. 16, pp. 3426–3428, 2004.
- [21] G. F. Zou, J. Zhao, H. M. Luo, T. M. McCleskey, A. K. Burrell, and Q. X. Jia, "Polymer-assisted-deposition: a chemical solution route for a wide range of materials," *Chemical Society Reviews*, vol. 42, no. 2, pp. 439–449, 2013.
- [22] W.-Z. Liang, Y.-D. Ji, T.-X. Nan et al., "Optimized growth and dielectric properties of barium titanate thin films on polycrystalline Ni foils," *Chinese Physics B*, vol. 21, no. 6, Article ID 067701, 6 pages, 2012.
- [23] W. Liang, Y. Ji, T. Nan et al., "Growth dynamics of barium titanate thin films on polycrystalline Ni foils using polymer-assisted deposition technique," *ACS Applied Materials and Interfaces*, vol. 4, no. 4, pp. 2199–2203, 2012.
- [24] W. Liang, Z. Li, Z. Bi et al., "Role of the interface on the magnetoelectric properties of BaTiO<sub>3</sub> thin films deposited on polycrystalline Ni foils," *Journal of Materials Chemistry C*, vol. 2, no. 4, pp. 708–714, 2014.
- [25] I. Barin, *Thermochemical Data of Pure Substances*, VCH, Weinheim, Germany, 1989.
- [26] C. Park, D. P. Norton, D. T. Verebelyi et al., "Nucleation of epitaxial yttria-stabilized zirconia on biaxially textured (001) Ni for deposited conductors," *Applied Physics Letters*, vol. 76, no. 17, pp. 2427–2429, 2000.
- [27] J. Chen, P. A. Parilla, R. N. Bhattacharya, and Z. Ren, "Growth of biaxially textured CeO<sub>2</sub>/YSZ/CeO<sub>2</sub> and SrTiO<sub>3</sub> buffer layers on textured Ni substrates by pulsed laser deposition," *Japanese Journal of Applied Physics*, vol. 43, no. 9, pp. 6040–6043, 2004.
- [28] G. W. Dietz, M. Schumacher, R. Waser, S. K. Streiffer, C. Basceri, and A. I. Kingon, "Leakage currents in Ba<sub>0.7</sub>Sr<sub>0.3</sub>TiO<sub>3</sub> thin films for ultrahigh-density dynamic random access memories," *Journal of Applied Physics*, vol. 82, no. 5, pp. 2359–2364, 1997.
- [29] C. S. Hwang, B. T. Lee, C. S. Kang et al., "Depletion layer thickness and Schottky type carrier injection at the interface between Pt electrodes and (Ba,Sr)TiO<sub>3</sub> thin films," *Journal of Applied Physics*, vol. 85, no. 1, pp. 287–295, 1999.
- [30] A. K. Burrell, T. Mark McCleskey, and Q. X. Jia, "Polymer assisted deposition," *Chemical Communications*, no. 11, pp. 1271–1277, 2008.
- [31] C.-J. Peng and S. B. Krupanidhi, "Structures and electrical properties of barium strontium titanate thin films grown by multi-ion-beam reactive sputtering technique," *Journal of Materials Research*, vol. 10, no. 3, pp. 708–726, 1995.
- [32] J.-S. Lee, Y. Li, Y. Lin, S. Y. Lee, and Q. X. Jia, "Hydrogen-induced degradation in epitaxial and polycrystalline (Ba,Sr)TiO<sub>3</sub> thin films," *Applied Physics Letters*, vol. 84, no. 19, pp. 3825–3827, 2004.
- [33] F. M. Pontes, E. R. Leite, E. Longo, J. A. Varela, E. B. Araujo, and J. A. Eiras, "Effects of the postannealing atmosphere on the dielectric properties of (Ba,Sr)TiO<sub>3</sub> capacitors: evidence of an interfacial space charge layer," *Applied Physics Letters*, vol. 76, no. 17, pp. 2433–2435, 2000.
- [34] K. T. Li and V. C. Lo, "Simulation of oxygen vacancy induced phenomena in ferroelectric thin films," *Journal of Applied Physics*, vol. 97, no. 3, Article ID 034107, 2005.
- [35] X. D. Qi, J. Dho, R. Tomov, M. G. Blamire, and J. L. MacManus-Driscoll, "Greatly reduced leakage current and conduction mechanism in aliovalent-ion-doped BiFeO<sub>3</sub>," *Applied Physics Letters*, vol. 86, no. 6, Article ID 062903, 3 pages, 2005.

## Research Article

# Magnetization Reversal and Specific Loss Power of Magnetic Nanoparticles in Cellular Environment Evaluated by AC Hysteresis Measurement

Satoshi Ota, Tsutomu Yamada, and Yasushi Takemura

Department of Electrical and Computer Engineering, Yokohama National University, Yokohama 240-8501, Japan

Correspondence should be addressed to Yasushi Takemura; [takemura@ynu.ac.jp](mailto:takemura@ynu.ac.jp)

Received 30 January 2015; Accepted 5 May 2015

Academic Editor: Yong Zhu

Copyright © 2015 Satoshi Ota et al. This is an open access article distributed under the Creative Commons Attribution License, which permits unrestricted use, distribution, and reproduction in any medium, provided the original work is properly cited.

The effect of intracellular hyperthermia induced by magnetic nanoparticles (MNPs) has been evaluated using a theoretical model. In this study, magnetization reversal of MNPs in the cellular environment under an AC magnetic field was evaluated on the basis of measured AC hysteresis loops. The specific and intrinsic loss powers—SLP and ILP—were also estimated from the area of AC hysteresis loops. The measured samples were a liquid sample dispersed in water, a fixed sample mixed with an epoxy bond, and a cellular sample. In the cellular environment, the rotations of particles and magnetic moments were inhibited by particle-cell and dipole-dipole interactions, respectively. The heat dissipation of the MNPs in the cellular environment was lower than that of the liquid and fixed samples. Moreover, the SLP in a single cell was estimated. The temperature increase of a single cell was calculated on the basis of the conventional theoretical model and the SLP measured in a single cell.

## 1. Introduction

Hyperthermia induced by magnetic nanoparticles (MNPs) is a potent tool in cancer therapy [1–3]. To increase the therapeutic effect of magnetic hyperthermia, combination therapy with other clinical agents and evaluation of the method to synthesize MNPs have been studied. In particular, antibody-modified MNPs exhibited a therapeutic effect on cancer owing to their enhanced selectivity toward cancer cells [4, 5]. The various sizes of spinal-structured iron oxide particles have been synthesized by changing heating time of  $\alpha$ -Fe<sub>2</sub>O<sub>3</sub> platelet particles in tetraethylene glycol [6]. In addition to hyperthermia, magnetic particle imaging (MPI) has recently attracted attention as the application to visualize MNPs in the human body for therapy and diagnostics [3, 7].

The volumetric power dissipation  $P$ , as calculated according to the following equation, is used to quantify the heat generated by MNPs [8]:

$$P = -f\mu_0 \oint M dH = \mu_0 \pi \chi'' f H^2, \quad (1)$$

where  $f$ ,  $\mu_0$ ,  $M$ ,  $H$ , and  $\chi''$  are the frequency of magnetic field and the permeability of free space, the magnetization

of MNPs, the magnetic field strength, and out-of-phase component of susceptibility, respectively. In addition, the specific and intrinsic loss powers—SLP and ILP—are used to express the mass power dissipation and the intrinsic heat dissipation, independent of the applied magnetic field and frequency [9, 10]:

$$\text{SLP} = \frac{P}{\rho}, \quad (2)$$

$$\text{ILP} = \frac{\text{SLP}}{fH^2}, \quad (3)$$

where  $\rho$  is the mass density of the MNPs. The magnetic properties of MNPs in tumor tissue and in cellular environments must be measured to evaluate the heating capability of MNPs under therapeutic conditions. The SLP in cellular and intratumor conditions has been estimated by a calorimetric measurement [11–14]. The SLP has been shown to decrease in tumor tissue and in the cellular environments as a consequence of the inhibition of particle rotation due to particle-particle and particle-cellular tissue interactions [13, 14]. Immobilization in tumors and cells inhibited Brownian

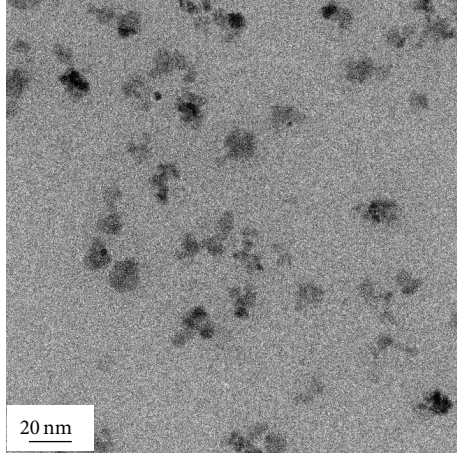


FIGURE 1: Transmission electron microscopic (TEM) image of the water-based magnetite nanoparticles.

relaxation. Moreover, a theoretical model for estimating the temperature increase of intratumor MNPs has been developed [15–17].

Magnetic relaxation loss is one of the heating mechanisms of MNPs, which is divided into Brownian and Néel relaxation. Brownian and Néel relaxation are associated with the rotation of particles and magnetic moments, respectively. Brownian and Néel relaxation times are obtained by the following equations [8]:

$$\tau_B = \frac{3\eta V_H}{k_B T}, \quad (4)$$

$$\tau_N = \frac{\sqrt{\pi}}{2} \tau_0 \frac{\exp(KV_M/k_B T)}{\sqrt{KV_M/k_B T}}, \quad (5)$$

where  $\eta$ ,  $V_H$ ,  $k_B$ ,  $T$ ,  $\tau_0$ ,  $K$ , and  $V_M$  are the viscosity of the suspended fluid, the hydrodynamic volume of MNPs, the Boltzmann constant  $1.38 \times 10^{-23}$  J/K, the temperature in Kelvin, the attempt time of  $\sim 10^{-9}$  s, the magnetocrystalline anisotropy constant, and the volume of the primary particle, respectively.

In this study, MNPs were dispersed in water, fixed with an epoxy bond, and added to cells. DC and AC hysteresis loops of each sample were measured. Magnetization reversal was evaluated on the basis of the AC hysteresis loops. Heat dissipation, as measured from the AC hysteresis loops, was not affected by a change in the state of the surrounding environment. The SLP and ILP were estimated from the area of the AC hysteresis loops. Moreover, the SLP in a single cell was calculated on the basis of the SLP of a cellular sample.

## 2. Materials and Methods

**2.1. Materials.** Water-based magnetite nanoparticles, Nanomag-D-spio, purchased from Micromod Partikeltechnologie GmbH, Rostock, Germany, were used in this study. The particle surface was functionalized by carboxylic acid group. Figure 1 shows the transmission electron microscopy (TEM)

image of the nanoparticles. The shape and size were not so uniform. The primary diameter was varied from 4 to 14 nm. The average was 9.8 nm with standard deviation of 2.0 nm. Their hydrodynamic diameter measured by dynamic light scattering (DLS) was  $40 \pm 16$  nm [18].

**2.2. Preparation of Liquid and Fixed Samples.** A liquid sample consisting of MNPs dispersed in water was prepared. For the preparation of the fixed sample, MNPs dispersed in water were mixed with an epoxy bond. The concentration of MNPs in both the liquid and fixed samples was 2.8 mg-Fe/mL.

**2.3. Preparation of Cellular Sample.** HeLa cells (human cervical carcinoma line) were cultured in Dulbecco's modified Eagle medium (DMEM) supplemented with 10% fetal bovine serum (FBS) and 1% penicillin-streptomycin (PS) at 37°C. HeLa cells were cultured in 100 mm dishes at a density of  $9 \times 10^5$  cells/well. After 50 h of incubation, a MNP solution with a concentration of 12  $\mu$ g-Fe/mL was added to cells in 10 mL of serum-free culture medium and the cells were allowed to stand for 16 h. After the cells were washed with phosphate-buffered saline (PBS), the cells were detached using 0.05% trypsin EDTA and purified by centrifugation at 1,000 rpm for 5 min. MNP-loaded cells were collected in a 2-mL tube as a cellular sample. The final concentration of MNPs was 2.8 mg-Fe/mL. The number of cells in the cellular sample was  $7 \times 10^7$  cells. The biocompatibility of magnetite nanoparticles to HeLa cells was previously studied [19]. The viability of HeLa cells was above 80% for 48 h after adding the nanoparticles at the concentration of 72  $\mu$ g-Fe/mL, which was higher than that used in this study. Figure 2 shows the images of detached HeLa cells measured as a cellular sample. Agglomerated MNPs were observed in the cytoplasm and on the membrane. The outer line of a cell indicates the membrane. The part inside the outer line of a cell was the cytoplasm because the outer line of the nucleus was clearly confirmed. Thus, MNPs observed in or around the outer line of a cell were evaluated as the intracellular or extracellular MNPs on the same plane, respectively. Although MNPs were internalized in cytoplasm, MNPs partially absorbed on the membrane were also confirmed. The diameters of MNP aggregations were measured and the volumes of MNP aggregations were calculated by the spherical approximation. The volume ratio of intracellular MNPs compared to MNPs both in the cytoplasm and on the membrane was approximately 81%. It was also confirmed that the particle localizations were changed in the different focused plane. It has been reported that iron oxide nanoparticles are degraded by lysosome [20]. However, degradation of magnetite nanoparticles in the cellular sample was evaluated by measuring DC and AC hysteresis loops in this study. Magnetization of the particles was not affected, which indicated that degradation of the nanoparticles during a limited period of the experiment was negligible.

**2.4. Measurement of DC and AC Hysteresis Loops.** DC hysteresis loops were measured by vibrating sample magnetometry (VSM) using a DC magnetic field of 4 and 8 kA/m as minor loops and 0.8 MA/m as major loops. AC hysteresis loops were measured in the frequency range of 100–500 kHz

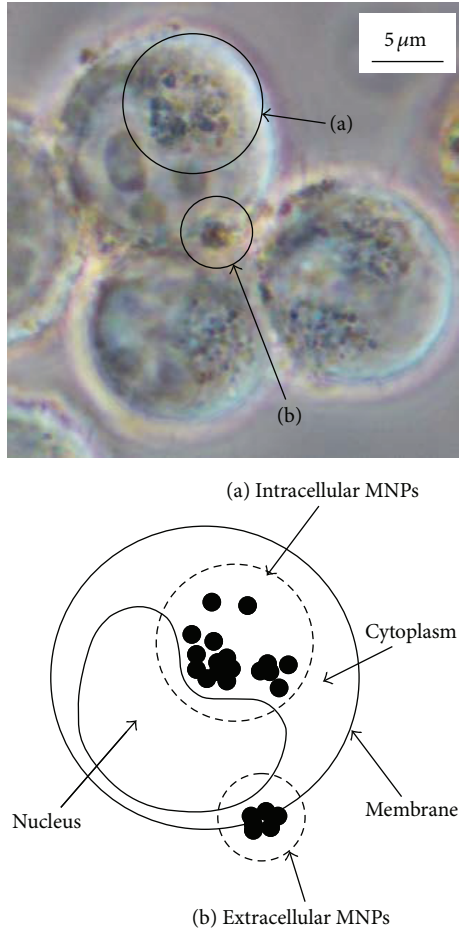


FIGURE 2: Detached HeLa cells as a cellular sample. (a) Intracellular and (b) extracellular MNPs were observed.

under an AC magnetic field of 4 and 8 kA/m as minor loops. The exciting coil was a 70-turn water-cooled solenoid with a 16.3 mm diameter [18]. All measurements were conducted at room temperature.

### 3. Results and Discussion

**3.1. DC Hysteresis Loops.** Figure 3 shows the DC major hysteresis loops of liquid, fixed, and cellular samples. Figure 3(b) shows the magnified images of Figure 3(a) at low magnetic field, which indicates the magnetization process in all of the samples. These samples exhibited superparamagnetism because the coercivity of the major loops in these samples was substantially low (Figure 3(b)). Anisotropic energy is given as the following equation:

$$E(\theta) = KV_M \sin^2(\theta), \quad (6)$$

where  $\theta$  is the angle between the easy axis and magnetic moment. The anisotropy energy is low in small  $\theta$ . The particle rotation reduces anisotropy energy because the easy axis follows the direction of a magnetic moment (see (6)). The magnetization in the liquid sample was higher than that in the fixed sample during the magnetization reversal

process (Figure 3(b)). The particles in the liquid sample are rotatable as opposed to the particles in the fixed sample. With respect to the liquid sample, the anisotropy energy barrier is decreased because particle rotation aligns the easy axis to the direction of the magnetic moment [21]. Therefore, the magnetic moment in the liquid sample was more rotatable than that in the fixed sample due to the lower anisotropy energy. For the superparamagnetic regime, magnetization reversal occurred due to the rotation of a magnetic moment whereas the reversal of a magnetic moment was associated with the magnetization reversal for the ferromagnetic regime. Although the magnetization in the liquid sample was higher than that in the fixed sample, the difference in the magnetization between the liquid and fixed samples was not significant. It is indicated that the effect of the particle rotation on the reduction of anisotropy energy is small because the random oscillation by the thermal energy is significantly influenced on the magnetization reversal for the superparamagnetic regime [22]. Thus, particle rotation slightly promoted the magnetization reversal in the liquid sample in comparison to that in the fixed sample. The magnetization in the cellular sample was lower than that in the fixed sample. The intracellular MNPs were encapsulated in endosomes and agglomerated in cytoplasm [23]. The extracellular MNPs were absorbed to the membrane in agglomerated state. In contrast to the cellular sample, MNPs were homogeneously dispersed in the fixed sample. The concentration of MNPs in the cellular sample was partially higher than that in the fixed sample because of the inhomogeneous agglomeration in the sample [24]. The interparticle distance is small at the higher concentration due to the inhomogeneous agglomeration. In the case of the smaller interparticle distance, the magnetization was decreased because the rotation of the magnetic moment was inhibited by dipole-dipole interaction [25]. Figure 4 shows the DC minor hysteresis loops of the liquid, fixed, and cellular samples. The minor loops exhibited no coercivity because of superparamagnetism. The magnetization of the fixed sample was lower than that of the liquid sample. In the liquid sample, the magnetic moments were reversed by the rotation of both the magnetic moments themselves and the particles. The reversal of the magnetic moment in the fixed sample was slower than that in the liquid sample because of the immobilized state in the fixed sample [13]. The magnetization of the cellular sample was lower than that of the fixed sample. Magnetization of the cellular sample was reduced as a consequence of dipole-dipole interaction due to inhomogeneous aggregation of MNPs in the cytoplasm and on the membrane [25].

**3.2. AC Hysteresis Loops.** Figure 5 shows AC hysteresis loops of the liquid, fixed, and cellular samples. The magnetization of the cellular sample was lower than that of the fixed sample, which was lower than that of the liquid sample. The magnetization of the AC minor hysteresis loops also indicates the magnetization reversal in the applied magnetic field range. With respect to the difference of the magnetization among all of the samples, the AC hysteresis loops showed the same trend with the DC minor hysteresis loops (Figures 3 and 4). The magnetization in the liquid sample was higher than that

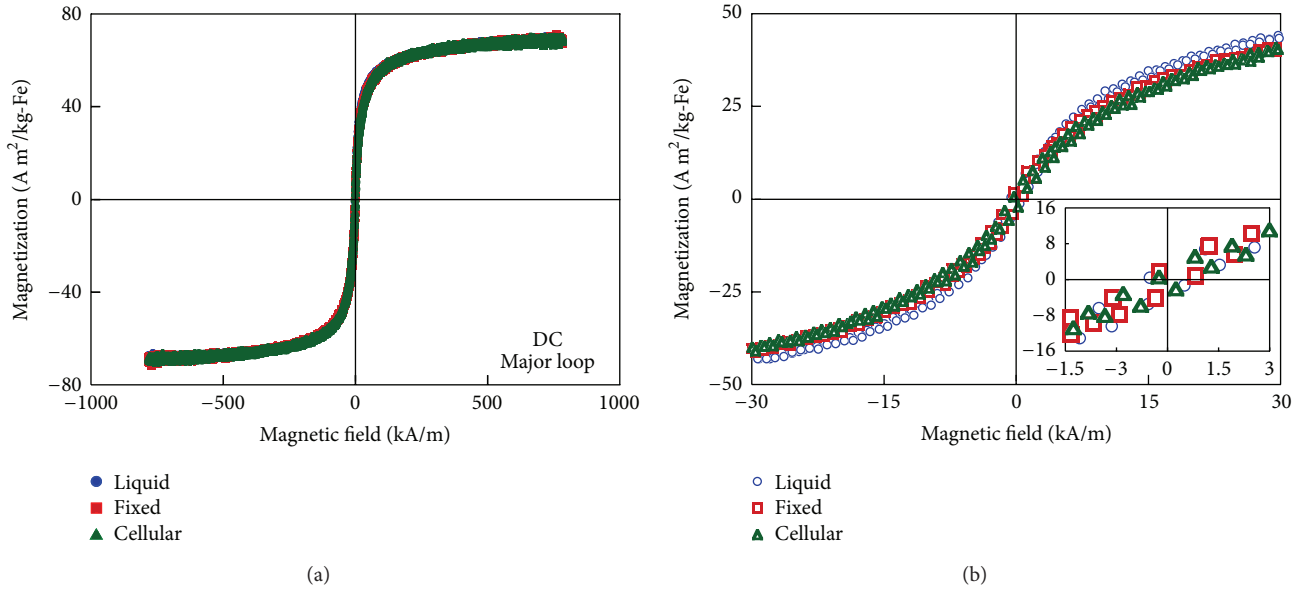


FIGURE 3: (a) DC major hysteresis loops of liquid, fixed, and cellular samples. The amplitude of the DC magnetic field was 0.8 MA/m. (b) Magnified images of (a) at low magnetic field.

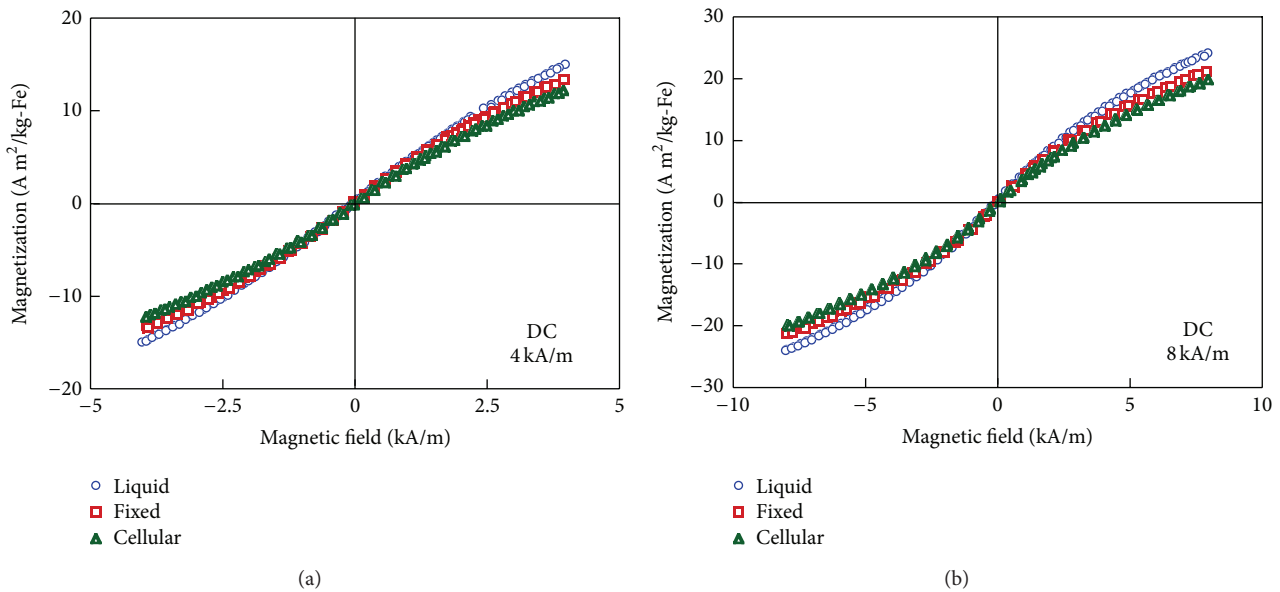


FIGURE 4: DC minor hysteresis loops of liquid, fixed, and cellular samples. The amplitude of the DC magnetic field was (a) 4 kA/m or (b) 8 kA/m.

in the fixed sample because of the anisotropy energy reduced by the particle rotation. In the cellular sample, the rotation of magnetic moments was inhibited due to dipole-dipole interaction induced by the inhomogeneous aggregation in the cellular environment. Unlike the DC minor hysteresis loops, the AC minor hysteresis loops revealed hysteresis areas in all of the samples because the rotation of the magnetic moments was delayed compared to the applied magnetic field. The results indicated that magnetic relaxation occurred due to a delay in the rotation of the magnetic moment in all of the samples. As indicated by the hysteresis loops of the fixed sample in which the particles were not

rotatable, Néel relaxation occurred in all of the samples, which exhibited areas. The coercivity of the liquid sample was higher than that of the fixed sample. Thus, Brownian relaxation occurred only in the liquid sample because the particles in this sample were rotatable [26]. Moreover, the coercivity of the cellular sample was the same as that of the fixed sample. It was indicated that delay of the rotation in magnetic moments in the cellular sample was similar to the fixed sample. These results indicate that particle rotation was inhibited by particle-cell interactions in the cellular environment. Only Néel relaxation occurred in the cellular sample [11, 13, 14].

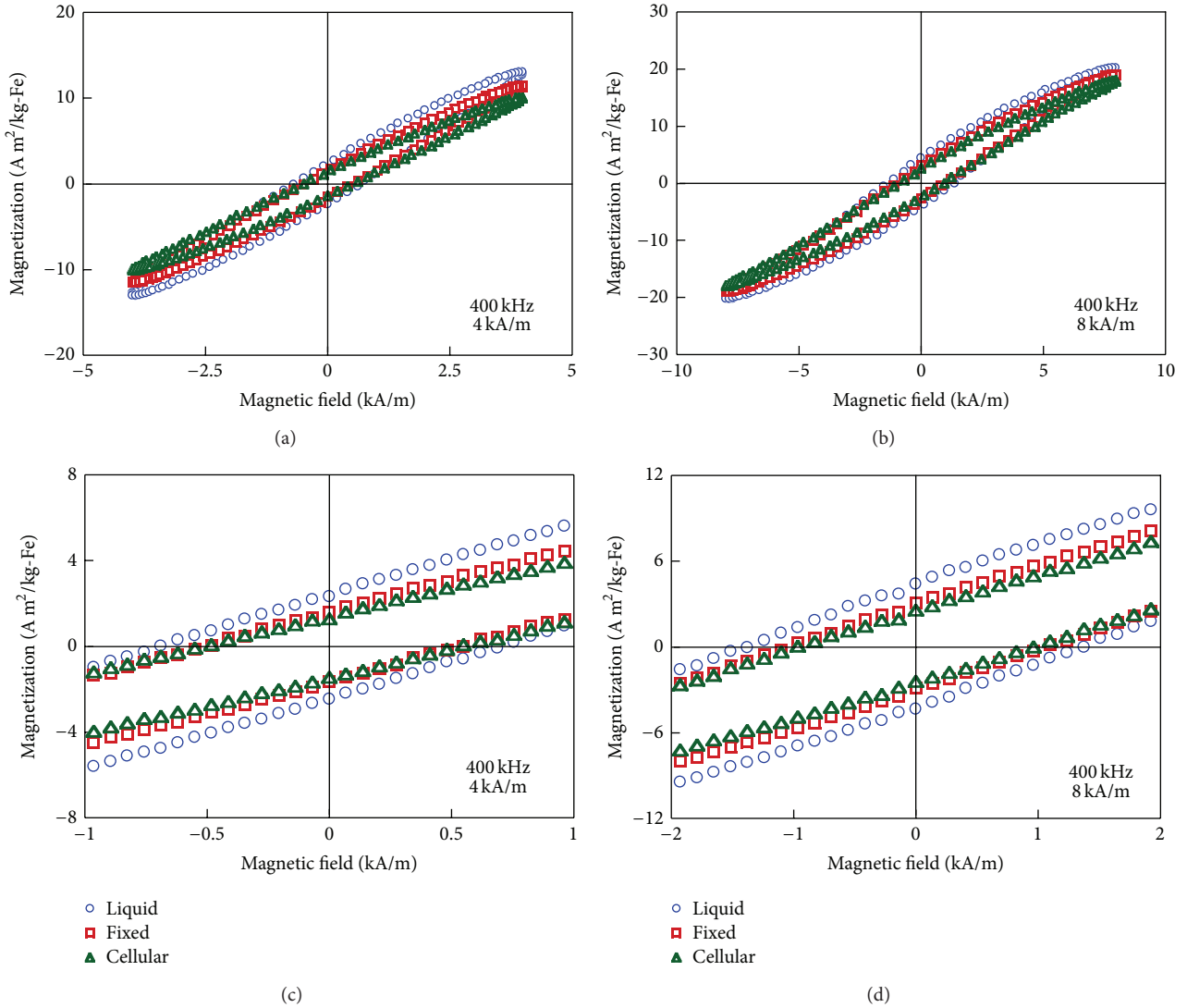


FIGURE 5: AC minor hysteresis loops of liquid, fixed, and cellular samples. The amplitude of the AC magnetic field was (a, c) 4 kA/m or (b, d) 8 kA/m. The frequency was 400 kHz. Magnified images of (a) and (b) are shown in (c) and (d), respectively.

### 3.3. Heat Dissipation Estimated from AC Hysteresis Loops.

The SLP was estimated from the area of the AC hysteresis loops. The ILP was calculated from the measured SLP and from (3). Figures 6 and 7, respectively, show the dependence of the SLP and ILP on the frequency of an applied magnetic field. By (5), the theoretical frequency of Néel relaxation peak  $f_N$  is higher than 2.2 MHz ( $K \leq 41 \text{ kJ/m}^3$ ) [8, 27, 28]. The measured frequency range in this study was lower than  $f_N$ . With increasing frequency, the ILP increased, the heat dissipation derived from the magnetic relaxation loss, and the rotation of the magnetic moments was gradually delayed. The decrease of the ILP between the liquid and fixed samples is associated with the inhibition of Brownian relaxation in the fixed sample. By (4), the theoretical frequency of Brownian relaxation peak  $f_B$  is 7.3 kHz ( $\eta = \eta_{\text{water}} = 0.89 \text{ mPa}\cdot\text{s}$ ). The theoretical  $f_B$  was lower than the measured frequency range, 100–500 kHz. However, higher coercivity in the liquid sample than in the fixed sample shows occurrence of Brownian

relaxation due to delay of particle rotation in the measured frequency range. The SLP of the intracellular MNPs has been estimated by a calorimetric measurement [11]. It has been reported that the SLP of intracellular MNPs was lower than that of MNPs dispersed in water because the Brownian relaxation was abrogated. With respect to the reduction of heat dissipation by the inhibition of Brownian relaxation, this study showed the same result with the conventional study. However, in this study, the measurements of magnetization reversal by DC and AC hysteresis loops also revealed that heat dissipation of MNPs in the cellular environment was lower than that of fixed MNPs because of the lower magnetization (Figures 4 and 5). The ILP of the cellular sample was lower than that of the fixed sample, as indicated by the lower magnetization of the cellular sample due to dipole-dipole interaction. The SLP is proportional to  $H^2$  when magnetization is linear with magnetic field (see (1) and (2)). However, magnetization was not linear with magnetic field

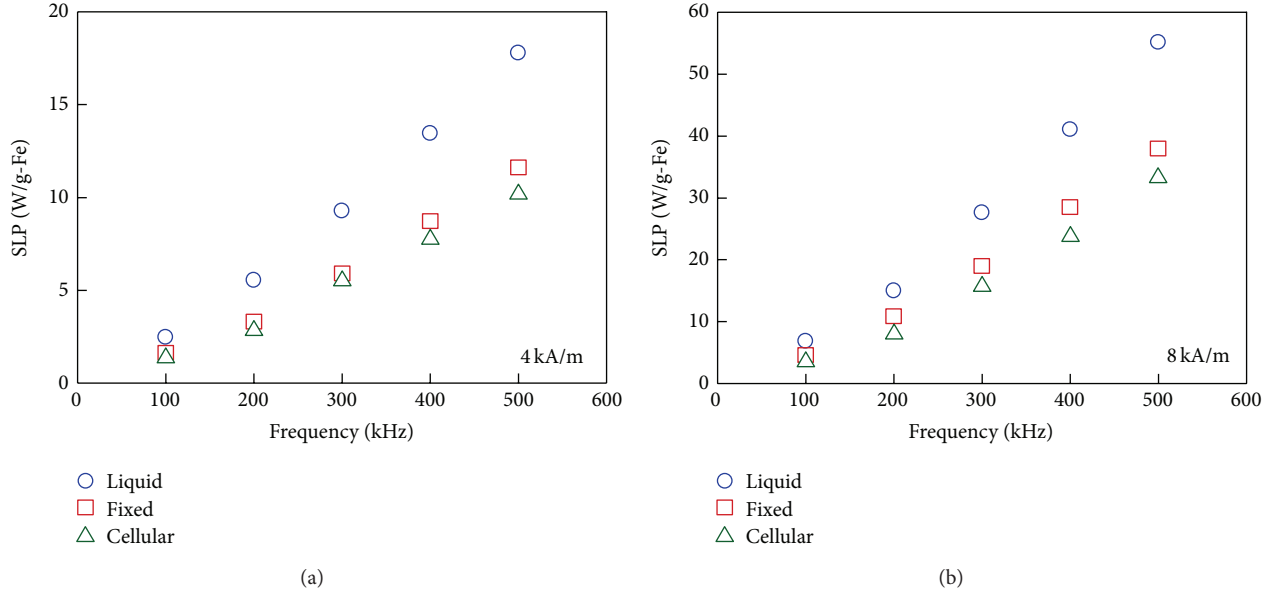


FIGURE 6: The dependence of SLP estimated from the areas of AC hysteresis loops on frequency. The amplitude of the magnetic field was (a) 4 kA/m or (b) 8 kA/m.

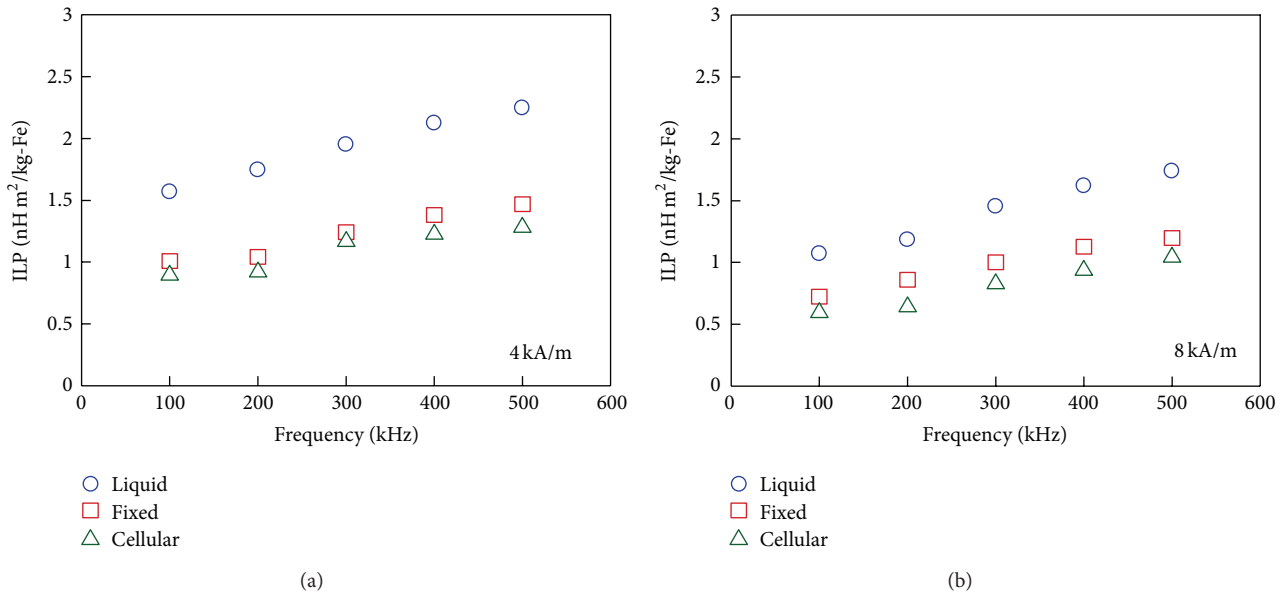


FIGURE 7: The dependence of the ILP calculated from the measured SLP (Figure 6) and (3) on frequency. The amplitude of the magnetic field was (a) 4 kA/m or (b) 8 kA/m.

in applied magnetic field range. The ILP at 8 kA/m was lower than that at 4 kA/m. In the case of SLP being unproportional to  $H^2$ , the ILP is lower at the higher magnetic field because the ILP is shown as the SLP normalized by  $H^2 f$  (see (3)).

The SLP in a single cell was estimated (Figure 8) using the following equation:

$$SLP_{\text{single cell}} = SLP_{\text{cellular}} \frac{m_{\text{Fe}}}{N_{\text{cell}}}, \quad (7)$$

where  $SLP_{\text{cellular}}$ ,  $m_{\text{Fe}}$ , and  $N_{\text{cell}}$  are the SLP, the mass of Fe, and the number of cells in the cellular sample, respectively.

The temperature increase at the center of a heated spherical object is estimated from the following equation [15–17]:

$$\Delta T_s = \frac{DP}{8k_s}, \quad (8)$$

where  $D$ ,  $P$ , and  $k_s$  are the diameter of the sphere, the heating rate per unit volume within the sphere, and the thermal conductivity of the sphere, respectively. Applying the spherical model in (8) to a single cell, (8) was obtained as

$$\Delta T_{\text{single cell}} = \frac{D_{\text{cell}}}{8k_{\text{cell}}} \frac{SLP_{\text{single cell}}}{V_{\text{cell}}}, \quad (9)$$

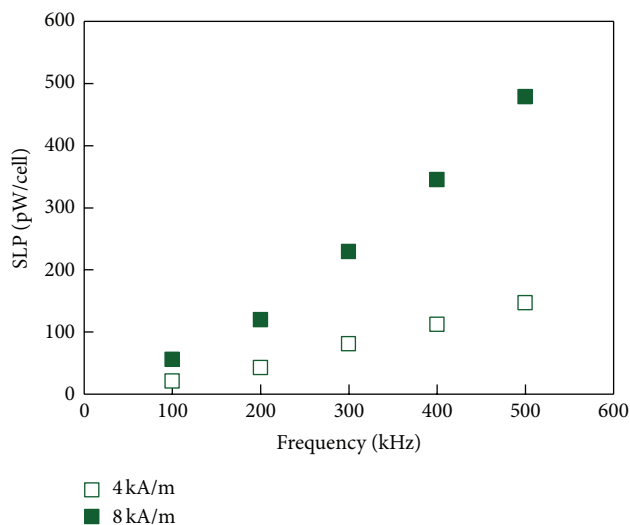


FIGURE 8: The dependence of the SLP in a single cell on frequency, as calculated from (7).

where  $D_{\text{cell}}$ ,  $V_{\text{cell}}$ , and  $k_{\text{cell}}$  are the diameter and volume of a single cell and the thermal conductivity of a cell ( $0.64 \text{ W/m}^\circ\text{C}$ ), respectively. In Figure 8, the SLP in a single cell was  $480 \text{ pW/cell}$  at  $8 \text{ kA/m}$  and  $500 \text{ kHz}$ . In the case of  $D_{\text{cell}} = 15 \mu\text{m}$ , the temperature increase of a single cell was  $12 \times 10^{-6}^\circ\text{C}$ . Therefore, at  $8 \text{ kA/m}$  and  $500 \text{ kHz}$ , the SLP of MNPs necessary to kill a single cell by hyperthermia treatment ( $\Delta T = 5^\circ\text{C}$ ) was  $14 \text{ MW/g-Fe}$  because the SLP of the cellular sample was  $33.6 \text{ W/g-Fe}$ . This result is in good agreement with the conventional estimation of SLP necessary to kill a single cell [29]. It was confirmed that hyperthermia focused on a single cell was restricted due to the limitation in the amount of MNPs internalized into a single cell [30, 31].

#### 4. Conclusion

The heating mechanism and heat dissipation of MNPs in the cellular environment were assessed via measurements of DC and AC hysteresis loops. In the intracellular state, the rotations of particles and magnetic moments were inhibited due to particle-cell and dipole-dipole interactions, respectively. Therefore, the heat dissipation of MNPs in the cellular environment was lower than that of MNPs in the liquid and fixed states, because Brownian relaxation was inhibited and magnetization decreased in a cell. It was also revealed that heat dissipation of MNPs in the cellular environment was reduced by dipole-dipole interaction due to the partial agglomeration of MNPs. Our results indicated that because the concentration of MNPs in the cells was low, the hyperthermia treatment was not conducted solely by intracellular hyperthermia. High intratumoral accumulation of MNPs in both intra- and extracellular states is necessary to induce hyperthermia.

#### Conflict of Interests

The authors declare that there is no conflict of interests regarding the publication of this paper.

#### References

- [1] C. C. Berry and A. S. G. Curtis, "Functionalisation of magnetic nanoparticles for applications in biomedicine," *Journal of Physics D: Applied Physics*, vol. 36, no. 13, pp. R198–R206, 2003.
- [2] Q. A. Pankhurst, N. K. T. Thanh, S. K. Jones, and J. Dobson, "Progress in applications of magnetic nanoparticles in biomedicine," *Journal of Physics D: Applied Physics*, vol. 42, Article ID 224001, 2009.
- [3] K. M. Krishnan, "Biomedical nanomagnetism: a spin through possibilities in imaging, diagnostics, and therapy," *IEEE Transactions on Magnetics*, vol. 46, no. 7, pp. 2523–2558, 2010.
- [4] A. Ito, K. Tanaka, K. Kondo et al., "Tumor regression by combined immunotherapy and hyperthermia using magnetic nanoparticles in an experimental subcutaneous murine melanoma," *Cancer Science*, vol. 94, no. 3, pp. 308–313, 2003.
- [5] S. Ota, N. Yamazaki, A. Tomitaka, T. Yamada, and Y. Takemura, "Hyperthermia using antibody-conjugated magnetic nanoparticles and its enhanced effect with cryptotanshinone," *Nanomaterials*, vol. 4, no. 2, pp. 319–330, 2014.
- [6] M. Kishimoto, K. Asai, A. Horiuchi, H. Yanagihara, Y. Nagasaki, and E. Kita, "Characterization of spinel-structured iron oxide particles synthesized by heating  $\alpha\text{-Fe}_2\text{O}_3$  platelets in tetraethylene glycol," *Materials Transactions*, vol. 54, no. 2, pp. 222–224, 2013.
- [7] B. Gleich and J. Weizenecker, "Tomographic imaging using the nonlinear response of magnetic particles," *Nature*, vol. 435, no. 7046, pp. 1214–1217, 2005.
- [8] R. E. Rosensweig, "Heating magnetic fluid with alternating magnetic field," *Journal of Magnetism and Magnetic Materials*, vol. 252, no. 1–3, pp. 370–374, 2002.
- [9] S. Dutz and R. Hergt, "Magnetic nanoparticle heating and heat transfer on a microscale: basic principles, realities and physical limitations of hyperthermia for tumour therapy," *International Journal of Hyperthermia*, vol. 29, no. 8, pp. 790–800, 2013.
- [10] M. Kallumadil, M. Tada, T. Nakagawa, M. Abe, P. Southern, and Q. A. Pankhurst, "Suitability of commercial colloids for magnetic hyperthermia," *Journal of Magnetism and Magnetic Materials*, vol. 321, no. 10, pp. 1509–1513, 2009.
- [11] J.-P. Fortin, F. Gazeau, and C. Wilhelm, "Intracellular heating of living cells through Néel relaxation of magnetic nanoparticles," *European Biophysics Journal*, vol. 37, no. 2, pp. 223–228, 2008.
- [12] C. L. Dennis, A. J. Jackson, J. A. Borchers et al., "Nearly complete regression of tumors via collective behavior of magnetic nanoparticles in hyperthermia," *Nanotechnology*, vol. 20, no. 39, Article ID 395103, 2009.
- [13] S. Dutz, M. Kettering, I. Hilger, R. Müller, and M. Zeisberger, "Magnetic multicore nanoparticles for hyperthermia-influence of particle immobilization in tumour tissue on magnetic properties," *Nanotechnology*, vol. 22, no. 26, Article ID 265102, 2011.
- [14] R. D. Corato, A. Espinosa, L. Lartigue et al., "Magnetic hyperthermia efficiency in the cellular environment for different nanoparticle designs," *Biomaterials*, vol. 35, no. 24, pp. 6400–6411, 2014.
- [15] W. Andrä, C. G. D'Ambly, R. Hergt, I. Hilger, and W. A. Kaiser, "Temperature distribution as function of time around a small spherical heat source of local magnetic hyperthermia," *Journal of Magnetism and Magnetic Materials*, vol. 194, no. 1, pp. 197–203, 1999.
- [16] Y. Rabin, "Is intracellular hyperthermia superior to extracellular hyperthermia in the thermal sense?" *International Journal of Hyperthermia*, vol. 18, no. 3, pp. 194–202, 2002.

- [17] M. Hedayati, O. Thomas, B. Abubaker-Sharif et al., "The effect of cell cluster size on intracellular nanoparticle-mediated hyperthermia: is it possible to treat microscopic tumors?" *Nanomedicine*, vol. 8, no. 1, pp. 29–41, 2013.
- [18] K. Nakamura, K. Ueda, A. Tomitaka, T. Yamada, and Y. Takemura, "Self-heating temperature and AC hysteresis of magnetic iron oxide nanoparticles and their dependence on secondary particle size," *IEEE Transactions on Magnetics*, vol. 49, no. 1, pp. 240–243, 2013.
- [19] A. Tomitaka, A. Hirukawa, T. Yamada, S. Morishita, and Y. Takemura, "Biocompatibility of various ferrite nanoparticles evaluated by in vitro cytotoxicity assays using HeLa cells," *Journal of Magnetism and Magnetic Materials*, vol. 321, no. 10, pp. 1482–1484, 2009.
- [20] K. Briley-Saebo, A. Bjørnerud, D. Grant, H. Ahlstrom, T. Berg, and G. M. Kindberg, "Hepatic cellular distribution and degradation of iron oxide nanoparticles following single intravenous injection in rats: implications for magnetic resonance imaging," *Cell and Tissue Research*, vol. 316, no. 3, pp. 315–323, 2004.
- [21] J. Carrey, B. Mehdaoui, and M. Respaud, "Simple models for dynamic hysteresis loop calculations of magnetic single-domain nanoparticles: application to magnetic hyperthermia optimization," *Journal of Applied Physics*, vol. 109, Article ID 083921, pp. 1–17, 2011.
- [22] D. Serantes, D. Baldomir, C. Martinez-Boubeta et al., "Influence of dipolar interactions on hyperthermia properties of ferromagnetic particles," *Journal of Applied Physics*, vol. 108, no. 7, Article ID 073918, 2010.
- [23] C. Wilhelm, C. Billotey, J. Roger, J. N. Pons, J.-C. Bacri, and F. Gazeau, "Intracellular uptake of anionic superparamagnetic nanoparticles as a function of their surface coating," *Biomaterials*, vol. 24, no. 6, pp. 1001–1011, 2003.
- [24] H. Mamiya and B. Jeyadevan, "Hyperthermic effects of dissipative structures of magnetic nanoparticles in large alternating magnetic fields," *Scientific Reports*, vol. 1, article 157, 2011.
- [25] S. Dutz and R. Hergt, "The role of interactions in systems of single domain ferrimagnetic iron oxide nanoparticles," *Journal of Nano- and Electronic Physics*, vol. 4, no. 2, Article ID 02010, 2012.
- [26] A. Tomitaka, K. Ueda, T. Yamada, and Y. Takemura, "Heat dissipation and magnetic properties of surface-coated  $\text{Fe}_3\text{O}_4$  nanoparticles for biomedical applications," *Journal of Magnetism and Magnetic Materials*, vol. 324, no. 21, pp. 3437–3442, 2012.
- [27] P. C. Fannin, C. N. Marin, and C. Couper, "Investigation of magnetic fluids exhibiting field-induced increasing loss peaks," *Journal of Magnetism and Magnetic Materials*, vol. 322, no. 9–12, pp. 1677–1681, 2010.
- [28] M. Suto, Y. Hirota, H. Mamiya et al., "Heat dissipation mechanism of magnetite nanoparticles in magnetic fluid hyperthermia," *Journal of Magnetism and Magnetic Materials*, vol. 321, no. 10, pp. 1493–1496, 2009.
- [29] R. Hergt and S. Dutz, "Magnetic particle hyperthermia—biophysical limitations of a visionary tumour therapy," *Journal of Magnetism and Magnetic Materials*, vol. 311, no. 1, pp. 187–192, 2007.
- [30] C. Wilhelm, F. Gazeau, J. Roger, J. N. Pons, and J. C. Bacri, "Interaction of anionic superparamagnetic nanoparticles with cells: kinetic analyses of membrane adsorption and subsequent internalization," *Langmuir*, vol. 18, no. 21, pp. 8148–8155, 2002.
- [31] C. Shundo, H. Zhang, T. Nakanishi, and T. Osaka, "Cytotoxicity evaluation of magnetite ( $\text{Fe}_3\text{O}_4$ ) nanoparticles in mouse embryonic stem cells," *Colloids and Surfaces B: Biointerfaces*, vol. 97, pp. 221–225, 2012.